Ultracold ^{87}Rb^{133}Cs Molecules: Production and Rotational Coherence

Li (Albert) Tao

A thesis submitted in partial fulfilment
of the requirements for the degree of
Masters by Research

Department of Physics
Durham University
2023

Declaration

I confirm that no part of the material offered has previously been submitted by myself for a degree in this or any other university. Where material has been generated through joint work, the work of others has been indicated.

Li Tao
Durham, Jan 13, 2023

Abstract

The thesis reports transferring the ultracold RbCs molecules to the absolute ground state and a trapping light that eliminates the differential AC Stark shift.

We build a laser system to perform Stimulated Raman Adiabatic Passage (STIRAP) for the molecules trapped in tweezers, which transfer the molecules from the weakly-bounded state to the absolute ground state. We use the offset cavity stabilisation technique to stabilise the laser frequencies to a passive cavity to narrow the laser linewidths while keeping the laser frequency tunable. We then align the beams to the molecules.

We demonstrate a "magic" laser frequency to eliminate the differential AC Stark shift of the rotational states in the ground vibrational state of RbCs molecule and to increase the rotational coherence time of multiple states. We study the AC Stark effect caused by the trapping light. We calculate the polarisabilities of the rotational states near a narrow electronic from $X^1\Sigma^+$ state to $b^3\Pi_0$ state and found at certain laser frequency the polarisabilities become the same. We measure the transition frequencies to different vibrational states in the excited electronic state experimentally. We perform microwave spectroscopy to measure the light shift and show that the shift vanishes at the magic frequency. We confirmed the coherence in 1 ms timescale by measuring the Ramsey fringe contrast.

Contents

Chapter 1

Introduction

1.1 Producing Ground State Molecules in an Optical Trap

1.1.1 Why Ultracold Polar molecules?

Ultracold polar molecules are ideal candidates to realise a series of proposals in quantum science. They exhibit reasonably large electric dipole moments which offers a system to explore anisotropic long-range dipole-dipole interactions tunable by external fields. Polar molecules exhibit dipole-dipole interactions in the electronic ground state, in states that have negligible spontaneous emission, and therefore have potentially longer lifetimes than e.g. Rydberg atoms. Furthermore, the additional vibrational and rotational degrees of freedom give the molecules rich internal structure that can be useful in many applications. For example, this provides a bigger Hilbert space to imprint information and realise a more complex platform than the neutral atom counterparts. Therefore, the system of the molecules have many potential applications, including quantum simulation[1, 2], quantum information [3, 4], precision measurement of the fundamental constants [5] and quantum-state-controlled chemistry [6–9]. Particularly, the rich structure of molecules facilitate the simulation of many-body physics [10–12], which is more difficult for neutral atoms.

For diatomic molecules, only the heteronuclear species have large permanent electric dipole moments that are required by many applications, because the asymmetric distribution of the electrons around the nuclei forms a dipole moment. We implement laser cooling to cool the constituent atoms, so we focus on alkali atoms which are suitable for this process. In our experiment we choose to use ^{87}Rb^{133}Cs molecule which has some advantages. For example, it's chemically stable so have a long lifetime; it has a large

electric dipole moment of 1.23 D in the molecular frame.

Most of the applications requires cooling and trapping the molecules in an optical trap as well as controlling the internal quantum states. In the previous years, much work has been done in our group to develop these tools [13–15]. In this work, we focus on two aspects of the research in this field: transferring the molecules to the ground state by Stimulated Raman Adiabatic Passage (STIRAP) and extend their rotational coherence using "magic" trapping.

1.1.2 Creating Ultracold Molecules - an Overview

In this section we discuss the steps to produce ultracold ^{87}Rb^{133}Cs (hereafter referred to as RbCs) molecules in an optical trap using the indirect method. We first produce ultracold ^{87}Rb and ^{133}Cs atoms using laser cooling, then we use magnetoassociation by sweeping over a Feshbach resonance to associate the atoms to a bounded molecular state followed by transferring the molecules to the absolute ground state by STIRAP. Below we will introduce each step of this process.

Laser Cooling of the Constituent Atoms

Laser cooling is a robust method to cool atoms down to $\sim \mu$K. This method is based on a transition between two energy states of an atom, normally the transition between $^2P_{3/2}$ state and $^2S_{1/2}$ state for alkali metal atoms, i.e., the D_2 line. Resonant light is incident to a gas of atoms to drive the transitions. The atom absorbs a photon and the momentum is changed by $\hbar\vec{k}$ along the direction of $\vec{k}$, where $\vec{k}$ is the wave vector of the light. The lifetime of the upper state is short, so the atom will emit a photon of the same frequency in a random direction and experience a momentum change in the opposite direction of the emitted photon. Then the atom is excited and the same process happens over and over again. The average of the momentum change due to the emission of the photon over a time is zero, meaning the atom experiences a net force in the direction of the light that slows it down. To reduce the velocity of an atom notably, $> 10^5$ photons need to be scattered. The reason why this method can't be readily applied to the molecules is that this process requires a closed transition, the population only decays back to the initial state after being excited, which is difficult for molecules due to the rich vibrational and rotational structure.

Magentoassociation

When we have the pre-cooled atoms of the two species, we can associate them to make molecules. Magnetoassociation uses a controlled magnetic field to associate the atoms. The atoms begin in the free atomic state at the magnetic field above Feshbach resonance. When the magnetic filed is ramped down over a Feshbach resonance at a slow enough speed, the atoms adiabatically follow an avoided crossing and end up with a bounded molecular state.

Stimulated Raman Adiabatic Passage

Stimulated Raman Adiabatic Passage, or STIRAP, is a general method to transfer population between states that are not directly coupled to each other via an intermediate state. The intermediate state can be strongly coupled to both the initial and the final state, but in the process it's never populated. This system can be described by a three-level model which will be discussed in detail in Chapter 2. In our experiment we use this technique to transfer the weakly-bounded molecules associated by Feshbach association to their ground electronic and rovibrational state. We have achieved the STIRAP efficiency of 93% [16], but in other paper, the transfer efficiency of unity was achieved [17]. Compared to other methods like a resonant π pulse in a two-state transition, STIRAP is relatively robust to the changes in the experimental parameters, for instance the variation of the light intensity and the single-photon detuning [18]. After first proposed in 1989, STIRAP was initially used to study collisional dynamics in molecular beam experiments. Nowadays, STIRAP has been used in many fields and systems. A complete review of STIRAP and its applications can be found in Ref. [19].

1.2 The AC Stark Effect and the Related Decoherence

Many proposed applications of the ultracold polar molecules take advantage of the dipole-dipole interaction between the molecules. These interactions can be controlled by external fields, for instance, static electric field or microwaves. Many of those applications requires the molecules being confined in optical lattices and high occupancy of the lattices. Occupancy fraction greater than 30% has been demonstrated by the previous works on RbCs Feshbach molecules [20] and KRb molecules [21] by associating the pre-filled constituent atoms in lattice sites. To successfully simulate the other systems using the confined

molecules, three criteria needs to be satisfied. One, the lifetime of the molecules in the lattice must be much greater than the evolving time of the Hamiltonian investigated. Two, the coherence time of the quantum states involved in the physical simulation process must be much greater than the characteristic interaction time associated with the interaction energy. The potential energy of the dipole-dipole interaction V_{dd} of two electric dipoles of $\sim$1 D in the lattice spacing of 500 nm is $\sim h \times 1$ kHz. Hence the coherence time needs to be greater than h/V_{dd}, i.e., $\sim$1 ms. Three, the Feshbach state and the absolute ground state of the molecule should have the same or similar polarisability to prevent excitation to higher lattice bands during the STIRAP process.

Previously we have studied the decoherence in the hyperfine states in the rotational ground state [22]. The careful choice of the magnetic field and the direction of the polarisation with respect to the magnetic field (known as the "magic angle") has been used to greatly reduce this decoherence.

In this work, we aim to eliminate decoherence between different rotational states. To do this, we will study the AC Stark effect of the light near a narrow transition between a singlet and a triplet electronic state to eliminate the decoherence between rotational states. We use the pre-established analytical equations to calculate the polarisabilities of the rotational states near this transition and show that they can be tuned by the light frequency such that the light shift of the transitions can be eliminated. This leads to a "magic frequency" that can extent the coherence time significantly. We then experimentally demonstrate the application of this magic frequency.

Chapter 2

Transferring Molecules to the Ground State in a New Experiment

The molecules produced by the magnetoassociation step described in Chapter 1 are in weakly-bound states with binding energies typically 1MHz. In this thesis we call the weakly-bound state "Feshbach state". The lifetime of this state is ∼100 ms. Furthermore, since the electric dipole moment d is proportional to r^{-7} where r is the inter-atomic separation, the molecules in the Feshbach state only have a negligible electric dipole moment. Therefore, for most of the applications, we want to transfer the molecules to their electronic and rovibrational ground state. STIRAP offers an efficient, robust and coherent method to transfer the molecules from their Feshbach state to the absolute ground state. In this chapter, the mathematical principle of STIRAP and the experimental setup of the laser system for it is described. The frequencies of the STIRAP lasers are stabilised to an optical cavity using a modified Pound-Drever-Hall technique, which is also described in this chapter.

2.1 The Theory of STIRAP in a 3-level System

In this section, we will look at the STIRAP process in an ideal 3-level system. The Feshbach state (referred to as $|F\rangle$) and the ground state (referred to as $|G\rangle$) are both coupled to a common electronic excited state (referred to as the excited state $|E\rangle$) by two laser frequencies. The light coupling the Feshbach state and the excited state is called the pump light, and the light coupling the ground state and the excited state is called the Stokes light. The diagram of such a system is shown in Fig. 2.1 (a). The pump (Stokes) light has a Rabi frequency Ω_P (Ω_S) and a detuning Δ_P (Δ_S) which is also shown in

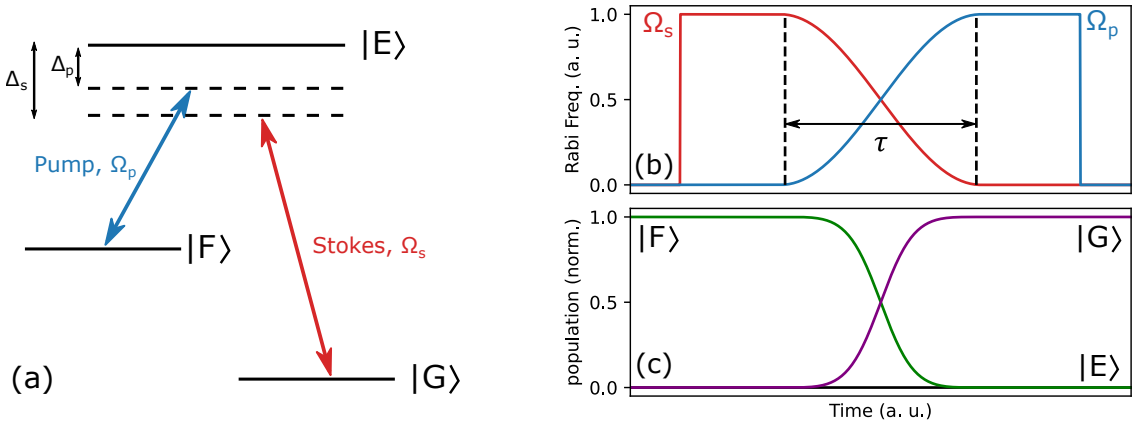

Figure 2.1: The illustration of an ideal STIRAP process. (a) Scheme for coupling the three relevant molecule states which are labelled as $|G\rangle$, $|F\rangle$ and $|E\rangle$. The blue and red lines indicate the pump and Stokes laser frequencies with Rabi frequencies of Ω_P and Ω_S and detunings from the excited state of Δ_P and Δ_S. (b) Example STIRAP pulse sequence. The Rabi frequency of the Stokes light starts high and is ramped down sigmoidally, whilst the pump Rabi frequency is ramped up. The typical timescale for STIRAP in our experiment is anticipated to be $\sim$ 20 μs. (c) The time evolution of the population in each state. The green, purple and black lines indicate the normalised population of state $|F\rangle$, $|G\rangle$ and $|E\rangle$, respectively. The population is gradually transferred from $|F\rangle$ to $|G\rangle$ without populating $|E\rangle$. The transfer time is τ.

Fig. 2.1 (a). The single-photon detunings of the two lights from resonance are

$$\hbar\Delta_P = \hbar(\omega_{P0} - \omega_P) \tag{2.1a}$$

$$\hbar\Delta_S = \hbar(\omega_{S0} - \omega_S), \tag{2.1b}$$

where ω_{P0} and ω_{S0} are the resonant frequencies of the pump and the Stokes transitions, ω_P and ω_S are the corresponding light frequencies.

The Hamiltonian of such a 3-level system in the rotating-wave approximation and neglecting loss is given by:

$$\hat{H} = \begin{pmatrix} 0 & \Omega_P(t) & 0 \\ \Omega_P(t) & 2\Delta_P & \Omega_S(t) \\ 0 & \Omega_S(t) & 2(\Delta_P - \Delta_S) \end{pmatrix}. \tag{2.2}$$

If we set $\Delta_P = \Delta_S = 0$, i.e., the lasers on two-photon resonance, we can solve the

analytical eigenstates of the above Hamiltonian to be:

$$|a^+\rangle = \sin\theta\sin\phi\,|F\rangle + \cos\phi\,|E\rangle + \cos\theta\sin\phi\,|G\rangle \tag{2.3}$$

$$|a^0\rangle = \cos\theta\,|F\rangle - \sin\theta\,|G\rangle \tag{2.4}$$

$$|a^-\rangle = \sin\theta\cos\phi\,|F\rangle - \sin\theta\,|E\rangle + \cos\theta\cos\phi\,|G\rangle\,, \tag{2.5}$$

where θ and ϕ are the mixing angles. θ is given by

$$\tan\theta = \frac{\Omega_P}{\Omega_S}. \tag{2.6}$$

ϕ is not relevant to the discussion of STIRAP but here we also give its expression:

$$\tan 2\phi = \frac{\sqrt{\Omega_P^2 + \Omega_S^2}}{\Delta_P}. \tag{2.7}$$

The state $|a^0\rangle$ is the dark state where there is no $|E\rangle$ component. This state is crucial for transferring the population directly from $|F\rangle$ to $|G\rangle$. When $\Omega_P = 0$ and $\Omega_S > 0$, the dark state $|a^0\rangle$ becomes equivalent to $|F\rangle$. When $\Omega_P > 0$ and $\Omega_S = 0$, the dark state becomes equivalent to $|G\rangle$. When Ω_P and Ω_S are both non-zero, the dark state is the superposition of $|F\rangle$ and $|G\rangle$. The sequence of light pulses is often described as "counter-intuitive" [23]. The initial state the molecular population is in is $|F\rangle$. To initialise all the population to the dark state, the Stokes light is first switched on with pump light off. In this case the compositions of $|F\rangle$ in $|a^+\rangle$ and $|a^-\rangle$ are both zero whilst the composition in $|a^0\rangle$ is 1. So this operation initialises the molecules to the dark state. Then the intensity of the Stokes light is ramped down and pump ramped up to change the mixing angle θ and hence the composition of $|a^0\rangle$. Eventually the Stokes light is ramped off and pump light is on. The excited state $|E\rangle$ is short-lived; the population in this state decays to a series of lower states. Therefore populating $|E\rangle$ leads to the loss of the molecules. If the ramps of the pump and the Stokes lights are slow enough, the whole process is adiabatic and all the population stays in the dark state. Thus the states $|a^+\rangle$ and $|a^-\rangle$ are never populated, which means the state $|E\rangle$ is never populated, so the loss of population is avoided and an efficiency of the process of 100% is achieved. In practice the perfect adiabaticity cannot be achieved as the ramps cannot be infinitely slow, the reason of which will be discussed in the next section. As the result, a small portion of the population is transfer to $|E\rangle$ and lost.

Figure 2.1 (b) shows the Rabi frequencies with which we drive the pump and Stokes transitions during STIRAP process. As described above, the Stokes light (red line) is switched on and ramped off, the pump light (blue line) is ramped on. The time of the ramps is denoted by τ. Figure (c) shows the changes of the normalised population of state

$|F\rangle$, $|G\rangle$, and $|E\rangle$ throughout the STIRAP pulse sequence in the ideal case where there is no loss. This sequence is completely reversible. For RbCs molecules that we use in out experiment, previous spectroscopy work has determined that the wavelengths of the pump and the Stokes light are 1557 nm and 977 nm, respectively [24]. These two beams will be discussed in details later in this chapter.

2.2 Experimental Requirements

The experiment requirements of STIRAP are imposed by the need for high efficiency. In the last section we assumed a perfect adiabatic process and thus a 100% efficient process. In this section we discuss the practical efficiency of the transfer (P) due to non-adiabaticity of the dark state evolution. The efficiency is given by [25]

$$P = \exp\left(-\frac{\pi^2\gamma}{\Omega_0^2\tau} - \frac{D\tau}{2}\right). \tag{2.8}$$

In this equation, P is the transfer efficiency, γ is the natural linewidth of $|E\rangle$, Ω_0 is the reduced Rabi frequency, $\Omega_0 = \sqrt{\Omega_S^2 + \Omega_P^2}$, where Ω_S and Ω_P are the highest Rabi frequencies in the whole process of each light, τ is the transfer time and D is the linewidth associated with the frequency difference between the two lasers. To get the maximum efficiency we need to minimise the term in the bracket in Eq. (2.8), which gives the condition for an efficient transfer [26]:

$$\frac{\Omega_0^2}{\pi^2\gamma} \gg \frac{1}{\tau} \gg D. \tag{2.9}$$

Looking from the left to the right, γ is determined by the chosen excited state $|E\rangle$ and the reduced Rabi frequency Ω_0 is limited by the available laser power and cannot be increased indefinitely. This sets the lower limit on τ. Then the laser linewidth associated with the frequency difference between the two lasers D needs to fulfill the right inequality.

It is important to search a wide range of states for a suitable $|E\rangle$ state that satisfies sever criteria. It needs to have a narrow natural linewidth γ, needs to be a mixed state to couple singlet with triplet molecular electronic potentials and needs to be isolated from other transitions. This requires both the lasers to be widely tunable over an overlapping frequency range to cover as many states as possible to find the optimum $|E\rangle$ state. Once γ is set, the minimum duration of the transfer τ is set in turn, then the laser linewidth D associated with the frequency difference must be narrow enough, which is the second requirement. In the experiment the two lasers are stabilised to the same optical cavity so the noise in frequencies is correlated, thus D is minimised. In previous work in our

group [24] it has been found that there are transitions allowing pulse durations on the order of $\sim$10 μs. This indicates the laser linewidth for an efficient transfer needs to be on the order of kHz.

2.3 Optical Cavities

2.3.1 Introduction

In optics, a device composed of two highly reflective mirrors aligned to the same axis is called an optical cavity or a Fabry-Pérot Interferometer. This device plays an essential role in the laser frequency stabilisation technique we use to provide the required linewidths of the STIRAP lasers. This technique will be introduced in Section 2.4. In this section we consider an ideal lossless cavity with linear geometry. The cavity theory will be described, followed by the characterisation of the cavity used in the experiment. For more details of the cavity theory, one can refer to optical or laser textbooks, for example, [27–29].

The light injected into the cavity is reflected back and forward between the two mirrors. The light can only be transmitted when the cavity length L is an integer times the half wavelength λ, i.e.,

$$L = n \cdot \frac{\lambda}{2}, n \in \mathbb{N}, \tag{2.10}$$

as at this frequency a standing wave is built within the cavity. The region in the frequency space where no light can be transmitted is called the free spectral range of the cavity which is referred as $\Delta\nu_{fsr}$ in this thesis. From the above equation one can readily derive that

$$\Delta\nu_{fsr} = \frac{c}{2L}, \tag{2.11}$$

where c is the speed of light. It is the narrow transmission (and reflection) spectrum that we use as a frequency reference to stabilise the laser frequencies provided the cavity length is stable. The details of the transmission and the reflection coefficients will be given below.

2.3.2 Cavity Theory

General Solution of The Cavity Field

The Hermite-Gaussian beams, or usually referred to as Gaussian beams, are the eigenstates of the electric field oscillating in an optical resonator such as a cavity. The expres-

sion of this electric field can be derived in the paraxial wave approximation. Hermite-Gaussian beams are expressed by [30]

$$\begin{aligned}\tilde{E}(x,y,z,t) = &\frac{w_0}{w(z)} H_l\left[\sqrt{2}\frac{x}{w(z)}\right] H_m\left[\sqrt{2}\frac{y}{w(z)}\right] \exp\left[-\frac{x^2+y^2}{w^2(z)}\right] \\ &\times \exp\left[-i\frac{k(x^2+y^2)}{2R(z)} + i(1+l+m)\arctan\frac{z}{z_R}\right] \\ &\times \exp\left[i(\omega t - kz)\right]\end{aligned}, \tag{2.12}$$

where $E(x,y,z,t)$ is the electric field, H_l and H_m are Hermite polynomials of order l and m, k is the wave vector, ω is the angular frequency of the light, and the rest of the quantities in this equation will be discussed later. The eigenstates with Hermite polynomials of order l and m are usually called TEM_{lm} where TEM stands for Transverse Electric and Magnetic which are both transverse in the paraxial wave approximation. The simplest solution can be obtained if one sets $l = m = 0$, then the electric field will reduced to Gaussian solution as the zeroth order Hermite polynomials equals 1. The Gaussian solution is

$$\tilde{E}(x,y,z) = \frac{w_0}{w(z)} \exp\left[-\frac{x^2+y^2}{w^2(z)}\right] \exp\left[-i\frac{k(x^2+y^2)}{2R(z)} + i\arctan\frac{z}{z_R}\right] \exp\left(-ikz\right), \tag{2.13}$$

ignoring time t. $w(z)$ is the spot size of the beam at z (z-axis is the propagation direction) and w_0 is the spot size at $z = 0$, i.e., the beam waist, and they are given by

$$w(z) = w_0\left[1 + \left(\frac{z}{z_R}\right)^2\right]^{\frac{1}{2}}. \tag{2.14}$$

$R(z)$ is the radius of curvature of the equiphase surface at z and reads

$$R(z) = \frac{z^2 + z_R^2}{z}. \tag{2.15}$$

In the above equations z_R is the Rayleigh range which describes the divergence of the beam:

$$z_R = \frac{\pi w_0^2}{\lambda}. \tag{2.16}$$

It is the distance along the propagation direction from the waist to the position where the beam cross area has doubled.

As shown in Eq. (2.12), there are multiple solutions of the cavity field labelled by l and m. The frequency spacing between them is [31]

$$\nu_{n,l,m} = \frac{c}{2L}\left[n + (l+m+1)\frac{\arccos\sqrt{g_1 g_2}}{\pi}\right], n, l, m \in \mathbb{N}, \tag{2.17}$$

where n is the label for longitudinal modes as in Eq. (2.10), l and m are the labels of the transverse modes as in Eq.(2.12), $g_i = 1 - L/\mathcal{R}_i$ are the resonator g parameters with $\mathcal{R}_i$ being the radius of curvature of the i-*th* mirror of the cavity.

Transmission and Reflection

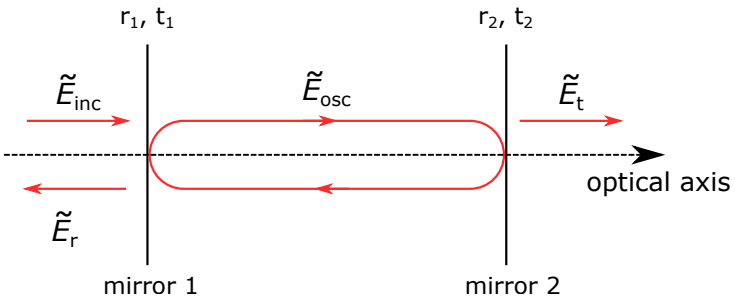

Figure 2.2: A two-mirror optical cavity. The light bouncing in the cavity interferes with itself and only builds up at certain wavelengths. The incident, reflected, transmitted and oscillation fields are labelled in the figure. For normal incidence, all the beams are along the optical axis.

The transmission and reflection spectra of the cavity are one of the most important traits of the cavity, which will be discussed in this sub-section. Figure 2.2 shows the diagram of the electric fields relevant to the cavity. The light is incident to mirror 1 of the cavity. A portion of the incident light is immediately reflected and the other enters the cavity and oscillates inside the cavity forming the oscillating field. Some of this field leaks through mirror 2 and becomes the transmitted field; some leaks through mirror 1 and interferes with the directly reflected field and in total becomes the reflected field.

When a plane wave light is incident to a mirror, the reflected and transmitted light are

$$\tilde{E}_{\mathrm{r}} = r\tilde{E}_{\mathrm{inc}}, \tag{2.18a}$$

$$\tilde{E}_{\mathrm{t}} = t\tilde{E}_{\mathrm{inc}}, \tag{2.18b}$$

with r and t being the amplitude reflection and transmission coefficient, respectively. Then the intensity reflection and transmission coefficient are r^2 and t^2. We only consider lossless mirrors, in which case we have $r^2 + t^2 = 1$ from the conservation of energy. The parameters of the mirrors of the cavity are shown in the figure.

For a cavity, there are generally three cases in terms of the mirror parameters [32]:

- *undercoupled* for $t_1^2 < t_2^2$;
- *impedance matched* for $t_1^2 = t_2^2$;
- *overcoupled* for $t_1^2 > t_2^2$.

The reflection and the transmission of a cavity are very different for each case. In this work we mainly consider an impedance-matched cavity, but the transmission and the

reflection coefficient for the general case without assuming the relations between the mirror parameters will also be given. For the impedance-matched case, we write $r_1 = r_2 = r$ and $t_1 = t_2 = t$.

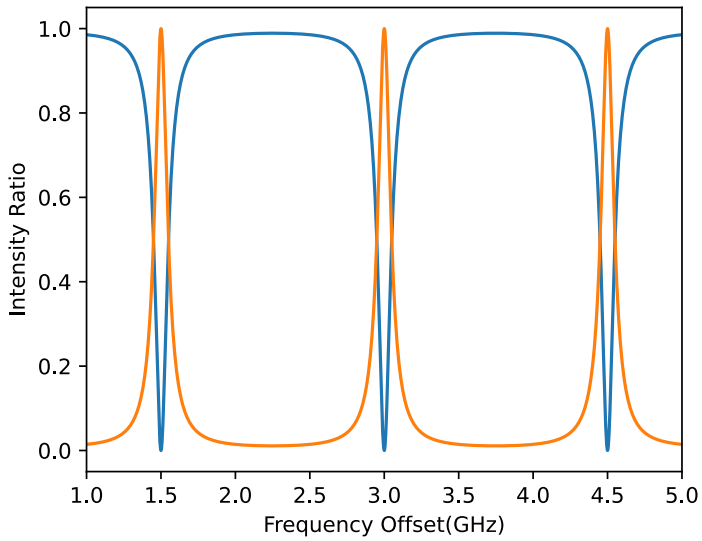

Figure 2.3: The ratio of the transmitted (orange) and the reflected (blue) light intensity to the incident light intensity of an optical cavity. The values are calculated for a finesse of 30 and a free spectral range of 1.5 GHz based on Eq. (2.20b) and Eq. (2.22b).

First we look at the cavity transmission. The field transmission is [32]

$$\frac{\tilde{E}_\mathrm{t}}{\tilde{E}_\mathrm{inc}} = \frac{-t_1 t_2 \exp(-ikL)}{1 - r_1 r_2 \exp(-i2kL)}, \tag{2.19a}$$

$$\frac{\tilde{E}_\mathrm{t}}{\tilde{E}_\mathrm{inc}} = \frac{-t^2 \exp(-ikL)}{1 - r^2 \exp(-i2kL)}, \tag{2.19b}$$

where in Eq. (2.19b) $t_1 = t_2 = t$ and $r_1 = r_2 = r$ and the other variables were defined before. The transmitted field is dependent on the light frequency which is related to the wave vector k. Then the light intensity transmission can be described by

$$\frac{I_\mathrm{t}}{I_\mathrm{inc}} = \frac{t_1^2 t_2^2}{1 + r_1^2 r_2^2 - 2 r_1 r_2 \cos 2kL}, \tag{2.20a}$$

$$\frac{I_\mathrm{t}}{I_\mathrm{inc}} = \frac{1}{1 + \frac{2r^2}{(1-r^2)^2} \cos 2kL}, \tag{2.20b}$$

where I_t and I_inc are the intensities of the transmitted and incident light. Equation (2.20a) gives the cavity transmission in general cases; Eq. (2.20b) describes the impedance-matched cavity transmission and is the well-known Airy function. The variable of the cosine $2kL$ is the light phase shift after one round trip in the cavity. Using $k = \omega/c$ and Eq. (2.11), the one round trip phase shift can also been expressed as $\omega/\Delta\nu_\mathrm{fsr}$ where ω is the light angular frequency and $\Delta\nu_\mathrm{fsr}$ is the cavity free spectral range. From Eq. (2.20b)

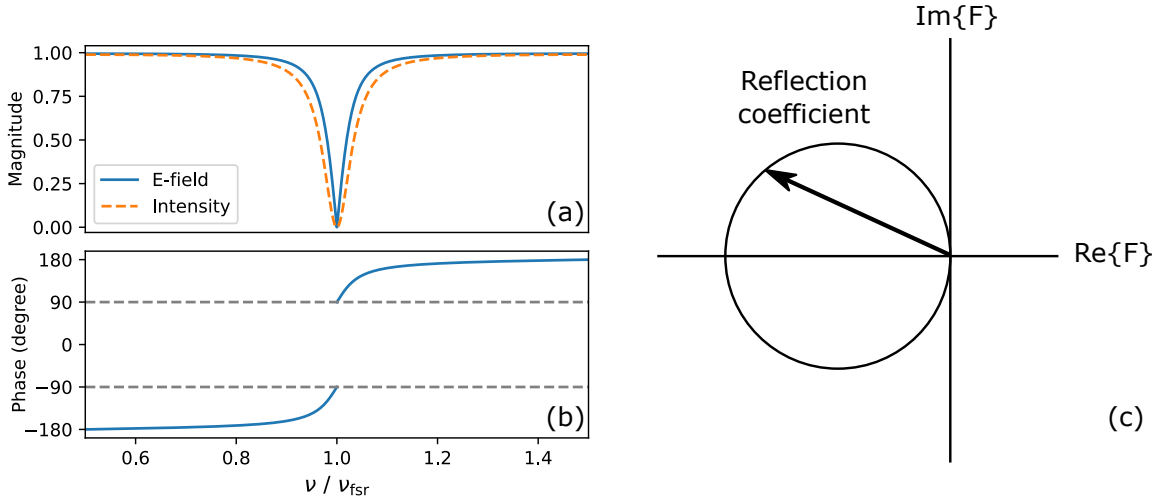

Figure 2.4: The complex reflection coefficient $F(\omega)$ of the cavity. Figure (a) shows $|F(\omega)|$ (blue solid line) corresponding to the E-field reflectance and $|F(\omega)|^2$ (orange dashed line) corresponding to the reflectance of the intensity. The phase of $F(\omega)$ is shown in (b). At $\nu/\nu_{\text{fsr}} = 1$, where ν_{fsr} is the free spectral range in frequency of the cavity, the phase jumps from $-90°$ to $90°$ due to the reflection's vanishing. The E-field reflectance is not smooth at this frequency but the intensity reflectance is smooth. For a critically coupled cavity, the end point of $F(\omega)$ on the complex plane is always on the circle that is tangent to the imaginary axis at the origin as shown in (c) and rotates anticlockwise as the frequency increases. When the laser frequency is on resonance $F(\omega) = 0$.

one can model the transmission of an impedance-matched cavity. Figure 2.3 shows the modelled cavity transmission signal for a cavity with a free spectral range of 1.5 GHz in the orange line. The full-width-half-maximum (FWHM) of the peaks in the transmission spectrum (or the cavity modes) is used to specify the linewidth of the peaks. This quantity is called cavity linewidth. In this work we use $\Delta\nu_{\text{cav}}$ to denote the FWHM of the cavity modes in frequency. It can be derived by equating the transmission to one half and solve the frequency.

Another important quantity of the cavity is the finesse ($\mathcal{F}$). It is given by

$$\mathcal{F} = \frac{\Delta\nu_{\text{fsr}}}{\Delta\nu_{\text{cav}}} = \frac{\pi}{2\arcsin\left(\frac{1-r_1 r_2}{2\sqrt{r_1 r}-2}\right)}. \tag{2.21}$$

The modelling shown in Fig. 2.3 considers a finesse of 30. Practically one have a cavity of a much higher finesse and the peaks in the transmission signal can be much narrower.

We are also interested in the reflected field and its intensity from the cavity. Here we give the cavity reflection coefficient as a function of the incident light angular fre-

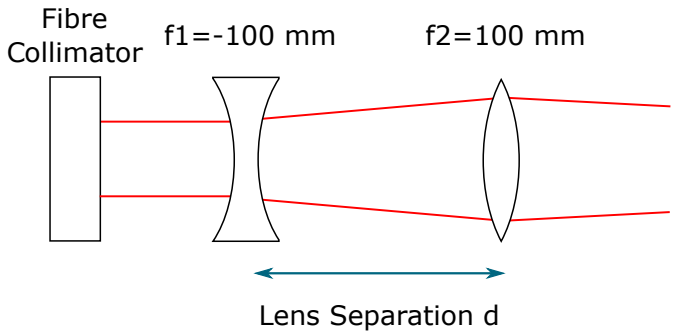

Figure 2.5: The cage setup for cavity mode-matching. A set of lenses modifies the beam after the fibre collimator to produce the desired waist at the plane mirror. The lens for the 977 nm and the 1557 nm beam have the same focal lengths. The fibre collimator and the lenses are mounted in a cage system. The beam waist and focus position can be fine adjusted by changing the lens separation d.

quency [33]:

$$F(\omega) = \frac{\tilde{E}_{\mathrm{r}}}{\tilde{E}_{\mathrm{inc}}} = -r_1 + \frac{t_1^2 r_2 \exp\left(i\frac{\omega}{\Delta\nu_{\mathrm{fsr}}}\right)}{1 - r_1 r_2 \exp\left(i\frac{\omega}{\Delta\nu_{\mathrm{fsr}}}\right)}, \tag{2.22a}$$

$$F(\omega) = \frac{\tilde{E}_{\mathrm{r}}}{\tilde{E}_{\mathrm{inc}}} = \frac{r\left[\exp\left(i\frac{\omega}{\Delta\nu_{\mathrm{fsr}}}\right) - 1\right]}{1 - r^2 \exp\left(i\frac{\omega}{\Delta\nu_{\mathrm{fsr}}}\right)}, \tag{2.22b}$$

where $F(\omega)$ is the complex reflection coefficient and $\omega = 2\pi \times \nu$ is the angular frequency of the incident field. Equation (2.22a) gives the reflection coefficient in general cases; Eq. (2.22b) gives the reflection coefficient of impedance-matched cavity. The total reflected light is the superposition of the light directly reflected by the first mirror that never enters the cavity and the the leaked light from the standing wave inside the cavity. The blue line in Fig. 2.3 shows the intensity of the reflected light calculated by taking the modulus square of $F(\omega)$. The parameters are the same as those used to calculate the transmitted light. Figure 2.4 shows the modulus and the phase of $F(\omega)$. At the resonant frequency the reflected light vanishes and causes the discontinuity in the phase as shown in Fig. 2.4 (a) and (b). It can be proven that for an impedance-matched cavity, the head of $F(\omega)$ on the complex plane lays on the circle centred at $-\frac{1}{2}$ with a radius of $\frac{1}{2}$. The arrow of $F(\omega)$ rotates anticlockwise as the frequency increases. When the light is on resonance, $F(\omega)$ is at the origin. The complex reflection coefficient is important as we will use it to understand the frequency stabilisation technique used in this work.

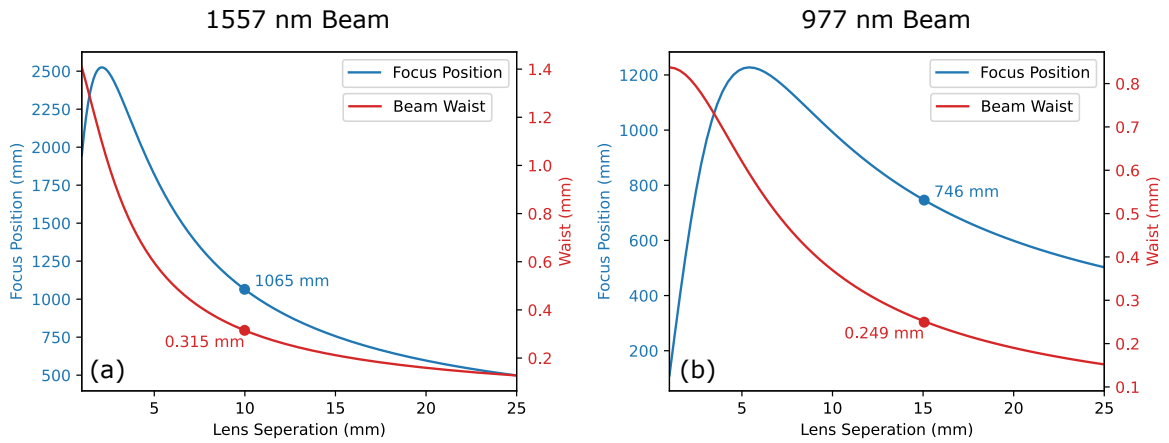

Figure 2.6: The modelling of the waist size (red) and the focus position (blue) as functions of the lens separation d in the cage system for (a): 1557 nm and (b): 977 nm beam. The desired beam waist and the focus position at corresponding lens separation for each beam are shown by the filled circles.

Mode-matching

The optical field of the cavity has multiple eigen solutions, but we want to couple as much light into the TEM_{00} mode (or the Gaussian mode) as possible which is called *mode-matching*. This is done when the shape of the light matches the cavity geometry. The radius of curvature of the beam at the positions of each mirror must match the radius of curvature of each mirror. We use a cavity with one flat mirror and one curved mirror in the experiment. Below we analyse the required beam shape to suit the cavity.

The radius of curvature of the beam at the waist is ∞, so it is necessary to set the focus at the flat mirror. Then the beam waist size is decided by the radius of curvature of the curved mirror. Since usually the radius of curvature of the curved mirror is a known value, we can calculate the required beam waist from it. Use Eq. (2.15) and Eq. (2.16) and set $R(0) = \infty$, $R(L) = \mathcal{R}$, one can easily derive

$$w_1 = \frac{[4(L\mathcal{R} - L^2)]^{\frac{1}{4}}}{\sqrt{k}}, \tag{2.23}$$

where w_1 is the waist at the flat mirror, L is the length of the cavity, $\mathcal{R}$ is the radius of curvature of the curved mirror and k is the wave vector.

We use lenses in a cage system to modify the beam. The beam waist is determined by Eq. (2.23), and the distance from the waist to the position of the last lens in the cage is also restricted by the layout of the optical table. On the one hand, we must accommodate the vacuum system for the cavity and the optics for locking and overlapping in between them; on the other hand, the size of the optical table is limited so the distance cannot be

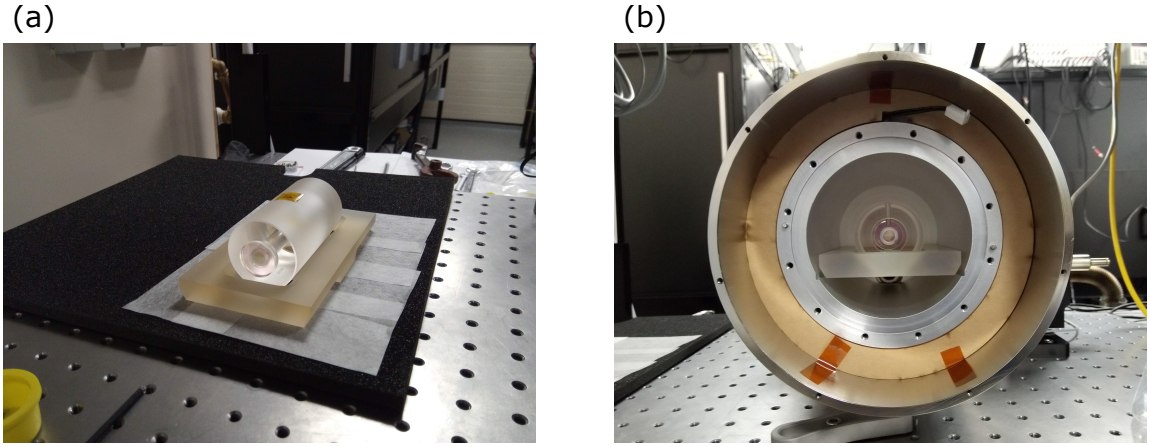

Figure 2.7: (a): The ULE cavity on Viton Balls on the Zerodur Mounting Block. (b): The ULE cavity in the vacuum housing. The material surrounding the cavity is thermal insulation. The upper black object is the heater.

too large. The cage system can ensure the right waist at an appropriate distance, whose diagram is shown in Fig. 2.5. The fibre collimator and two lenses of focal length -100 mm and 100 mm are mounted in the same cage. This makes alignment easy and facilitates adjusting the separation of the lenses d. The 1557 nm light and the 977 nm light use the same combination of lenses.

The waist size and position of the beam after the cage will change as separation d changes. We can model them by the ABCD-matrix formalism. The modelling results of the beams with the two STIRAP wavelengths are given in Fig. 2.6. The focus position measured from the last lens in the cage is shown on the left axes in blue; the beam waist is shown on the right axes in red. The modelling is based on the $1/e^2$ beam radii of the collimators which are measured beforehand. The desired waist at the plane mirror of each beam is calculated by Eq. (2.23) and shown in the figures by the red closed circles. The waist is 0.315 mm for 1557 nm light and 0.249 mm for 977 nm light. The corresponding distances from the last lens to the waist are 1065 mm and 746 mm, respectively, as shown by the blue circles. These distances are acceptable. The desired waist can be achieved by $\sim$10 mm separation for 1557 nm light and $\sim$15 mm for 977 nm light.

2.3.3 Optical Cavity Characterisation

In this section, we will present and characterise the optical cavity used in our experiment. We use a commercial cavity manufactured by Stable Laser System. The spacer of the cavity is made of an Ultra-Low-Expansion (ULE) material. This material is special because there is a zero crossing of the thermal expansion coefficient. At the zero crossing

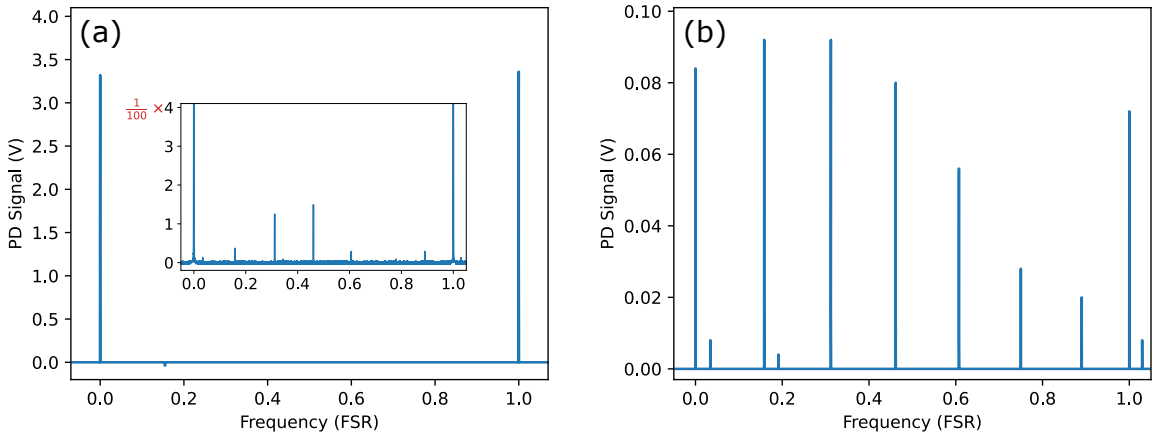

Figure 2.8: The transmission signal of the 1557 nm light showing mode-matching to the cavity. Figure (a) shows the good mode-matching signal. The two visible peaks are adjacent Gaussian modes. The insert figure has the same x- and y- axis labels as the main figure with a y-axis scale of 1/100 of that of the main figure and shows the amplitudes of the higher order transverse modes which are not visible in the main figure. At good mode-matching, the Gaussian modes are of two orders of magnitude higher than the transverse modes. Figure (b) shows the bad mode-matching. The spacing between the higher order modes agrees with Eq. (2.17).

temperature the thermal expansion coefficient is zero, which minimises the drift of the spacer length caused by the temperature drift. This temperature is hard to be predicted precisely [34]. Stable Laser System, the supplier of the cavity, measured the zero crossing temperature of the spacer to be 27(1) °C. We stabilse the temperature of the cavity to this value. One of the mirrors of the cavity is plane; the other one is curved and has a radius of curvature of 50 cm. This facilitates mode-matching as introduced in Section 2.3.2. The mirror coating is customised to provide high finesse at 420 nm, 977 nm, 1013 nm and 1556 nm. Among them, 977 nm and 1556 nm are the wavelengths of the STIRAP lasers, 420 nm and 1013 nm are the wavelengths of the lasers also locked to the same cavity but not relevant to STIRAP and they will not be discussed in this thesis.

Figure 2.7 (a) shows a picture of the cavity. The cavity spacer is 10 cm long; the mirror diameter is 1 inch. The cavity sits in the vacuum housing provided by Stable Laser System as shown in Fig. 2.7 (b). Inside the vacuum housing, the cavity is placed on a Zerodur mounting block which is supported on Viton balls. The pressure in the vacuum housing is kept at 1.7×10^{-7} mbar by the ion pump produced by Gamma vacuum. There is thermal insulation in the vacuum can. The temperature inside the can is set to the zero crossing temperature by the temperature controller and measured by thermistors (General Electric MC65F103B).

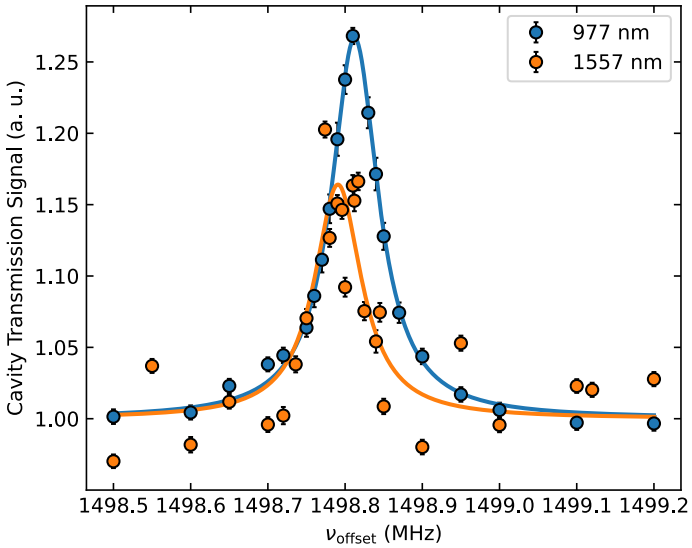

Figure 2.9: The measurement of the free spectral range of the cavity at two wavelengths. The carrier is stabilised to a cavity mode and sidebands are generated by modulating the light phase. The offset of sidebands from the carrier can be tuned by tuning the modulation frequency. The free spectral range is measured by tuning the offset frequency and recording the cavity transmission signal (filled circles). The data are fitted to the Lorentzian function (solid lines) to extract the centre position and the linewidth.

The characteristics of the cavity are summarised in Table 2.1. The cavity was characterised at two STIRAP wavelengths, 977 nm and 1557 nm. The free spectral range, cavity linewidth, finesse and the beam waist ω_1 are given in the table.

Figure 2.8 shows the cavity transmission signal of the 1557 nm light when the laser frequency is scanned over roughly 1 free spectral range. The case of good mode-matching is shown in Fig. 2.8 (a). The two high peaks are the adjacent Gaussian modes and the small peaks in the insert are the higher order transverse modes. Note that the y-scale of the insert is 1/100 of the y-scale of the main figure, so most of the light power is coupled into TEM_{00} mode. For a case of bad mode-matching, all the transverse modes are present and the power of each mode is lower than the power of good mode-matching. The signal for the 977 nm laser is similar. The designed reflectivity of the cavity mirrors at these wavelengths is lower than 0.5%, correspondingly, the minimum finesse is 5000. The expected maximum cavity linewidth ν_{cav} is 300 kHz. This is less than the linewidth of the free running lasers. Therefore, in Fig. 2.8 (a), the transmission peaks are too narrow to measure the width, and it doesn't give information of the free spectral range.

To precisely measure the cavity free spectral range, we add two sidebands beside the carrier and stabilise[1] the carrier to a cavity mode (TEM_{00}, the same below). This

[1]The laser stabilisation will be introduced in Section 2.4.

operation narrows the laser linewidth to be less than the cavity linewidth. Then we can tune the spacing between the carrier and the sidebands and measure the transmission signal. When the sidebands are away from cavity modes only the carrier is transmitted. When the sidebands overlap with the next cavity mode they are transmitted and the transmitted power of light rises and thus we can measure the free spectral range. The results of the 977 nm light and the 1557 nm light are shown in Fig. 2.9 by the filled blue and orange circles. The shape of the transmitting signal is described by Eq. (2.20b) and can be approximated by a Lorentzian function. Fitting the data to a Lorentzian function (solid lines) can extract the centres of the peaks which is the free spectral range and the peak linewidths. From Fig. 2.9 one can see that the data of the 977 nm light is close to the fitted line while the data of the 1557 nm light is more noisy. Here we discuss the reason. In our setup we use fibre EOMs for both beams, but they are of different model. The output end of the fibre with the EOM for 1557 nm light is unangled, which means the retroreflection between the fibre output and the first mirror of the cavity forms another optical resonator. This makes the light intensity after the EOM oscillate. Since this oscillation is outside the EOM, it can be tuned out by the demodulation phase and won't affect frequency stabilisation (details see Section 2.4), but it affects the light intensity passes through the cavity. Therefore, the data of the 1557 nm light is noisy as the transmitted light from the cavity is measured. The finesse can also be calculated. The exact numbers of $\Delta\nu_{\text{fsr}}$ and $\Delta\nu_{\text{cav}}$ and the finesse of each light are given in Table 2.1. The reason why the free spectral ranges $\Delta\nu_{\text{fsr}}$ for the two wavelengths are slightly different is that the coating of the cavity mirrors has different refractive indices at different wavelengths, which slightly changes the total cavity length for different wavelengths. The theoretical free spectral range given by $c/2L$ is 1499.0 MHz. Considering the value of the cavity length is provided by the manufacturer and the error of it is unclear, the measured value agrees well with the theory. The values of finesse measured in this way are given in the column of "Finesse 1". The linewidth of the frequency stabilised laser is about 3 orders of magnitude less than that of the cavity linewidth so it won't affect the results of $\Delta\nu_{\text{cav}}$. We will see the laser linewidth in Section 2.5.2.

To better measure the cavity finesse, we also measure the cavity dynamic response signal of the reflected light [35]. The signal can be detected when the input laser frequency is swept across the cavity resonant frequency with a reasonably high scan rate. The mirrors of the cavity are not perfectly reflective, therefore, a portion of the input field will enter the cavity and bounce between the cavity mirrors forming a cavity field. The modulation of the input light frequency induces an oscillating component in the cavity field. This

λ (nm)	$\Delta\nu_{\text{fsr}}$ (MHz)	$\Delta\nu_{\text{cav}}$ (kHz)	Finesse 1	Finesse 2	w_1 (mm)
977	1498.8123(9)	74(3)	$200(8) \times 10^2$	$204(2) \times 10^2$	0.249
1557	1498.7907(9)	74(3)	$202(8) \times 10^2$	/	0.315

Table 2.1: The summary of the cavity characteristics for each wavelength. The cavity spacer length is 10 cm, one mirror is plane, the other is curved with a radius of curvature of 50 cm. In the table, Finesse 1 is measured from the cavity transmission signal; Finesse 2 is measured from the cavity dynamic response signal. w_1 is the waist at the plane mirror.

cavity field can be described by the differential equation [35]

$$\frac{\mathrm{d}E_{\text{cav}}}{\mathrm{d}t} = \left(\frac{\rho - 1}{\tau} + \frac{i2\rho\dot{\omega}L}{\tau c}t\right) E_{\text{cav}} + \frac{i\sqrt{T_1}}{\tau}E_0, \tag{2.24}$$

where E_{cav} is the amplitude of the cavity field, t is time, ρ is the cavity round-trip loss factor, τ is the uninterrupted round-trip time, i is the imaginary unit, $\dot{\omega}$ is the frequency sweep rate, L is the length of the cavity, c is the speed of light in vacuum, T_1 is the power transmission coefficient of the first cavity mirror, E_0 is the field amplitude of the input field. Again, due to the non-unity reflectance of the cavity mirrors, some of the cavity field will leak from the first cavity mirror and be combined with the directly reflected field from it. We can use a photodiode to detect this signal while sweeping the input light frequency.

The differential equation Eq. 2.24 indicates that the oscillating component of the cavity field decays over time. The decay time of this signal indicates the mirror reflection coefficient and hence the finesse. The decay time is characterised by the storage time τ_s which is defined as the time required for the cavity field to decay to $1/e$ of its initial strength. It is related to the finesse$\mathcal{F}$ by

$$\tau_s = \frac{2\mathcal{F}L}{\pi c}. \tag{2.25}$$

The dynamic response signal of the 977 nm light reflected from the cavity is shown in Fig. 2.10 (a) and (b) with a linear and a logarithm y-axis scale. The signal and fitted curve shown in Fig. (a) and (b) are identical. The overall trend of the oscillating signal can be seen in Fig. (a) while Fig. (b) offer a better view for the peaks with small amplitudes at linger time. The original data is smoothed by taking a rolling average of 40 points around each data point. The heights of the peaks of the oscillation are fitted to an exponential decay function to extract the storage timeτ_s. Due to the photodiode responsivity, the signal amplitude in the fitting function is multiplied by an arbitrary number, before arbitrary offsets are added to the time and the amplitude. Then the only

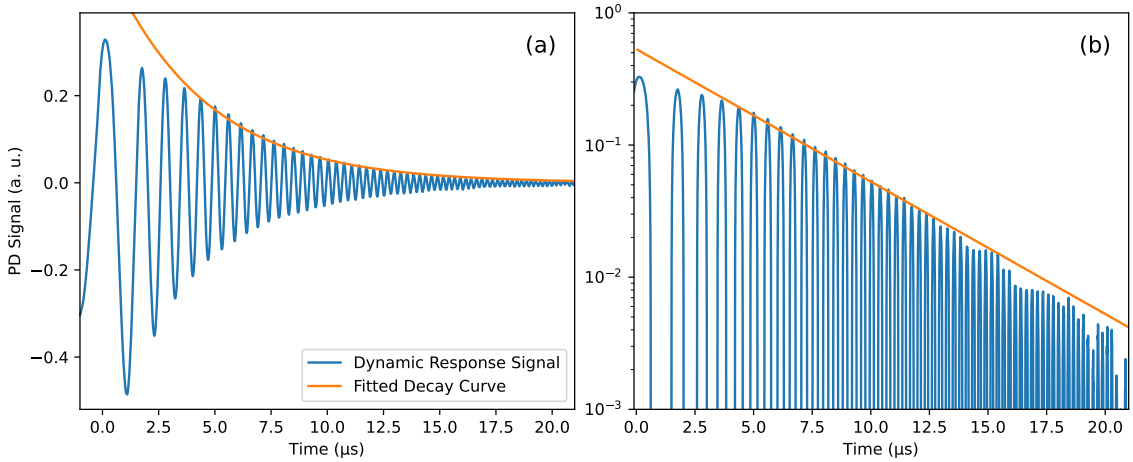

Figure 2.10: The cavity dynamic response signal measured with the 977 nm light reflected from the cavity. The data is smoothed by taking the rolling average of the 40 points around each point. The orange line is a fitting of the envelope of the dynamic response signal (blue) to an exponential decay function. The fitting parameters include the storage time τ_s, the oscillation amplitude scale, an offset to the amplitude and an offset to the time. The storage time is extracted from the fitting. The first 3 peaks are lower than the fitting line because the light hasn't fully built up in the cavity. They are excluded from the fitting. Figure (a) and (b) show the identical signal and the fitted curve with linear and logarithm y-axis scales. Due to the limit of a logarithm y-axis scale, only the upper half of the signal is shown in (b).

free parameter in the fitting function is the storage time τ_s. The first three peaks are neglected in the fitting because by the time they appear the light hasn't fully built up in the cavity. The storage time from this signal is 4.33(5) μs which corresponds to a finesse of $204(2) \times 10^2$. This is given in Table 2.1 as "Finesse 2". It agrees with the "Finesse 1" within the error and has a smaller error bar. In the time frame of this project the signal for the 1557 nm light hasn't been measured.

2.4 Laser Frequency Stabilisation With an Optical Cavity

This section introduces the theory of the Pound-Drever-Hall (PDH) technique [36] we use to stabilise the frequency of the lasers for STIRAP.

2.4.1 Introduction

The stabilisation of laser frequency is critical for many applications ranging from precise spectroscopy to atomic clocks. A key characteristic describing the short-term stability of laser frequency is the laser linewidth which is the width of its optical spectrum and features its frequency stability. Another type of the laser frequency stability is the long-term stability which describes the drift of the centre frequency over a longer time. The free-running linewidth is inadequate for the application in STIRAP without active stabilization of the laser frequency and the long-term frequency stability is also needed. Therefore, the lasers for STIRAP need to be frequency stabilised, or "locked". There has been many frequency stabilisation techniques developed before using atomic transitions as a frequency reference. These include frequency modulation spectroscopy [37] and modulation transfer spectroscopy [38] which limit the linewidth to sub-MHz level. But for the lasers for STIRAP, those techniques are ineffective as there are no suitable atomic transitions in the desired frequency region, so the signal used to correct the laser frequency (the "error signal") can't be generated. Furthermore, based on the requirements on the STIRAP lasers described in Section 2.2, good relative stability between the two lasers are needed and their linewidths need to be in the range of kHz. Therefore, a narrow, arbitrary frequency reference point is needed to generate the error signal. We use an optical cavity to produce the frequency reference which has been introduced in Section 2.3. In this section, we describe a modified Pound-Drever-Hall technique to generate the error signal allowing the laser frequencies to the stabilised to the desired cavity mode while keeping the frequencies tunable, i.e. offset sideband locking [39].

2.4.2 Standard Pound-Drever-Hall (PDH) Locking

Before introducing the offset sideband locking technique, we first review the principles of the standard Pound-Drever-Hall (PDH) frequency stabilisation based on [36]. An optical cavity with a high finesse has a series of narrow resonant modes as described in Section 2.3.2. The general idea of the PDH stabilisation technique is to measure the

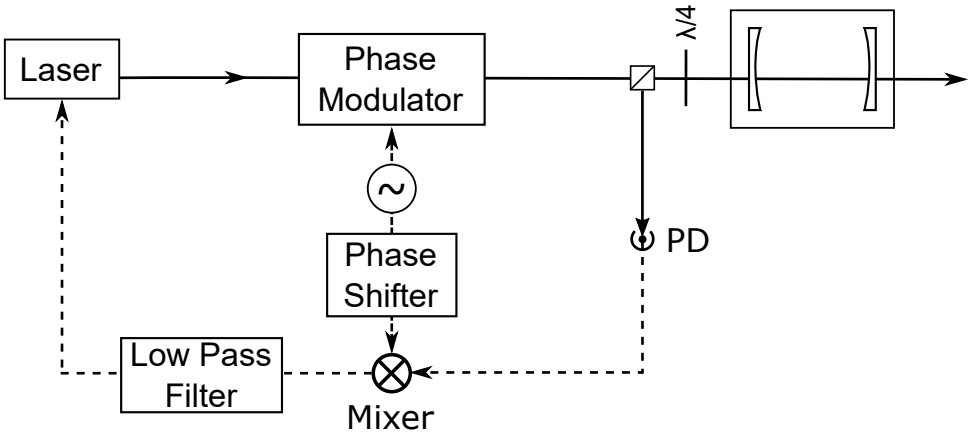

Figure 2.11: Diagram of the setup for the standard Pound-Drever-Hall locking. The solid lines represent light; the dashed lines represent RF signals. The light coming from the laser is modulated by a phase modulator and then sent to an optical cavity. The reflected light from the cavity is detected by a photodiode. The signal from the photodiode and the signal driving the phase modulator after a phase shifter are mixed then pass through a low pass filter to derive the error signal. This signal is fed back to the laser to correct its frequency.

frequency of the laser with an optical cavity, and the result of the measurement is fed back to the laser to adjust the laser frequency. A typical setup diagram for this technique is shown in Fig. 2.11. The function of each component and the mechanism of this technique will be described in detail below based on [36].

One can measure the transmitted signal of the optical cavity. When the laser frequency is on resonance with the cavity, the transmission is nearly 100%. However, there are some problems with this method. One is that the fluctuation of the laser intensity is coupled with the fluctuation of the frequency, both of which cause the transmitted light intensity to change. The other is that the transmission signal is symmetric in terms of frequency around resonance, so the electronics can't distinguish whether the laser frequency is above or below resonance.

A better method is to measure the reflected signal of the cavity instead. This decouples the fluctuations in frequency and intensity because the reflected light will always be zero no matter how much the intensity fluctuations when the laser is on resonance. The conceptual model is that although the reflection signal is also symmetric in terms of frequency, one can measure the derivative of the reflection signal which is antisymmetric. Note that practically we don't measure the derivative of the reflection signal. This is only to facilitate understanding of the technique.

Previously in Section 2.3.2, we have carefully derived the complex cavity reflection

coefficient $F(\omega)$ of the electric field. There is a discontinuity in the phase of the reflection coefficient $F(\omega)$ around the laser frequency being equal to the cavity free spectral range times an integer (Fig. 2.4 (b)) which can be used to tell if the laser frequency is below or above the cavity resonance frequency. The phase of the light can't be measured directly, but one can modulate the light phase and generate two sidebands with opposite phases and fixed frequency difference. Then the beating signal of the sidebands indicates the phase of the reflected light.

The laser phase can be modulated by a phase modulator, for example, an electro-optic modulator (EOM). The electric field of the incident light to the cavity at certain point in the space with its phase modulated is

$$\tilde{E}_{\text{inc}} = E_0 e^{i(\omega t + \beta \sin \Omega t)}, \tag{2.26}$$

where ω is the frequency of the light, Ω is the modulation frequency and β is the modulation depth. The power of the light is $P_0 = \frac{1}{2} c\epsilon_0 |E_0|^2 \times A$ where A is the area of the beam. Using Jacobi-Anger expansion

$$e^{iz\cos\theta} = \sum_{n=-\infty}^{\infty} i^n J_n(z) e^{in\theta}, \tag{2.27}$$

and

$$J_{-n}(z) = (-1)^n J_n(z), \tag{2.28}$$

where $J_n(z)$ is Bessel function of the first kind of order n, at small modulation depth β, this electric field can be expanded by Bessel functions to

$$\tilde{E}_{\text{inc}} \approx E_0 \left[J_0(\beta) e^{i\omega t} + J_1(\beta) e^{i(\omega+\Omega)t} - J_1(\beta) e^{i(\omega-\Omega)t} \right]. \tag{2.29}$$

The Bessel functions of higher orders are neglected for small β. One can see that there are three bands in the modulated beam: a carrier with angular frequency ω and two sidebands with angular frequencies $\omega \pm \Omega$ and opposite phases. The power of the carrier and the first order sidebands is P_c and P_s, respectively, where

$$P_c = \frac{1}{2} c\epsilon_0 |E_0 J_0(\beta)|^2 \times A = J_0(\beta)^2 P_0, \tag{2.30}$$

$$P_s = \frac{1}{2} c\epsilon_0 |E_0 J_1(\beta)|^2 \times A = J_1(\beta)^2 P_0. \tag{2.31}$$

For small β we have

$$P_c + 2P_s \approx P_0. \tag{2.32}$$

This expansion allows us to treat each band independently. To calculate the reflected electric field, we can multiply each beam by the reflection coefficient F at the corresponding frequency. We derive the reflected field:

$$\tilde{E}_{\text{r}} = E_0 \left[F(\omega) J_0(\beta) e^{i\omega t} + F(\omega+\Omega) J_1(\beta) e^{i(\omega+\Omega)t} - F(\omega-\Omega) J_1(\beta) e^{i(\omega-\Omega)t} \right]. \tag{2.33}$$

What we can measure with a photodiode is the power of the reflected light which is proportional to the square modulus of the electric field. The power of the reflected beam with angular frequency Ω is given to first order by

$$\begin{aligned} P_{\mathrm{r},\Omega} =& P_c|F(\omega)|^2 + P_s|F(\omega+\Omega)|^2 + P_s|F(\omega-\Omega)|^2 \\ &+ 2P_0J_0(\beta)J_1(\beta)\mathrm{Re}[F(\omega)F^*(\omega+\Omega) - F^*(\omega)F(\omega-\Omega)]\cos\Omega t \\ &+ 2P_0J_0(\beta)J_1(\beta)\mathrm{Im}[F(\omega)F^*(\omega+\Omega) - F^*(\omega)F(\omega-\Omega)]\sin\Omega t \\ &+ (2\Omega \text{ terms}). \end{aligned} \tag{2.34}$$

In this expression, the $\cos\Omega t$ and the $\sin\Omega t$ terms are from the beat note between the carrier and the sidebands and the 2Ω terms are from the sidebands beating against each other. It is the the $\cos\Omega t$ and the $\sin\Omega t$ terms that we care about because they tell us the phase of the carrier. We can use a mixer to extract the amplitude of the oscillations at angular frequency Ω. The diagram of an ideal mixer is shown on the left. The mixer accepts two input signals and produces one output signal which is the product of the input signals.

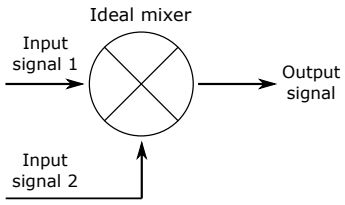

Figure 2.12: An ideal mixer.

Considering the trigonometric identities below:

$$\sin a \sin b = \frac{\cos(a-b) - \cos(a+b)}{2} \tag{2.35a}$$

$$\cos a \cos b = \frac{\cos(a-b) + \cos(a+b)}{2} \tag{2.35b}$$

$$\sin a \cos b = \frac{\sin(a-b) + \sin(a+b)}{2}, \tag{2.35c}$$

one can see that the output frequencies are the sum and difference of the input frequencies. To get the amplitude of the the Ω terms, the signal from the photodiode and the signal at the modulation frequency Ω are fed to a mixer, the output of which consists of the error signal as the DC component and the 2Ω components. A low pass filter is used to filter the higher frequency components. There are two terms with angular frequency Ω that are proportional to the real part and the imaginary part of the term in the square bracket in Eq. (2.34), respectively.

At high modulation frequency ($\Omega \gg \Delta\nu_{\mathrm{cav}}$), when the carrier is near resonance, all the sidebands are reflected. Hence we have $F(\omega \pm \Omega) \approx -1$ and $|F(\omega)|^2 \approx 0$ (see Fig. 2.4). Then

$$F(\omega)F^*(\omega+\Omega) - F^*(\omega)F(\omega-\Omega) \approx -2i \cdot \mathrm{Im}[F(\omega)]. \tag{2.36}$$

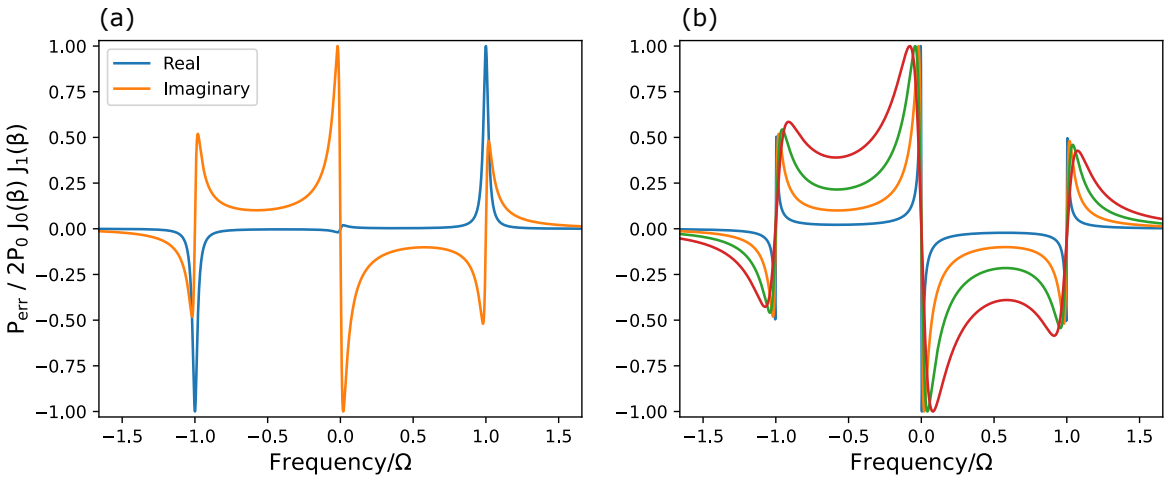

Figure 2.13: Modelling of the PDH error signal. (a): The calculated error signals for 0° (labelled by imaginary) and 90° phase shift (labelled by real) of the input signals to the mixer with the cavity finesse being 20000. The imaginary and the real part correspond to the $\sin\Omega t$ and the $\cos\Omega t$ term, respectively. 0° phase shift produces a good error signal. (b): The error signals at 0° phase difference with a series of values of finesse. Increasing the finesse sharpens the error signal.

In the above equation the real part vanishes. The reflected power becomes

$$P_{\mathrm{r},\Omega} = 2P_s - 4P_0 J_0(\beta) J_1(\beta) \mathrm{Im}[F(\omega)] \sin\Omega t + (2\Omega \text{ terms}). \tag{2.37}$$

To select the sine term in Eq. (2.34), the phase shift between the inputs of the mixer needs to be carefully tuned such that the DC component is non-zero. To obtain the sine term, we need 0 phase shift as $\sin\Omega t \cdot \sin\Omega t$ produces the $\cos(\Omega t - \Omega t) = 1$ term. The phase shift can be controlled by a delay line, a phase shifter or tuning the signal phase on the function generator.

Having shown that $F(\omega)F^*(\omega+\Omega) - F^*(\omega)F(\omega-\Omega)$ is nearly purely imaginary, we take the imaginary part of this quantity as the error signal P_{err} which reads

$$P_{\mathrm{err}} = 2P_0 J_0(\beta) J_1(\beta) \mathrm{Im}[F(\omega)F^*(\omega+\Omega) - F^*(\omega)F(\omega-\Omega)]. \tag{2.38}$$

Figure 2.13 (a) shows both the real and the imaginary part of $F(\omega)F^*(\omega+\Omega) - F^*(\omega)F(\omega-\Omega)$. The modulation frequency is two orders of magnitude greater than the cavity linewidth. Note that the x-axis is the frequency of the carrier, $\omega/2\pi$, with respect to a resonant frequency. When the carrier is near resonance, the real part vanishes while the imaginary part produces a steep error signal that can be used to stabilise the laser frequency. The error signals with different ratios of the modulation frequency and the cavity linewidth are presented on Fig. 2.13 (b). With the same modulation frequency and cavity free spectral range, increasing the finesse steepens the centre slope of the error signal.

Now we calculate the gradient of the centre slope with some approximations. We rewrite the carrier angular frequency as:

$$\omega = \omega_N + \delta\omega, \tag{2.39}$$

where ω_N is the nearest resonant (angular) frequency associated with an integer number N of the cavity modes (i.e. $\omega_N = N \cdot \Delta\omega_{\text{fsr}}$), $\delta\omega$ is the (angular) frequency deviation from resonance. Then we have[2]

$$\frac{\omega}{\Delta\nu_{\text{fsr}}} = 2\pi N + \frac{\delta\omega}{\Delta\nu_{\text{fsr}}}. \tag{2.40}$$

When near resonance, we have $\delta\omega/\Delta\nu_{\text{fsr}} \ll 1$ and $\delta\omega/\Delta\nu_{\text{cav}} \ll 1$. For a cavity with high finesse, we can make the approximation [40]:

$$\mathcal{F} = \frac{\Delta\nu_{\text{fsr}}}{\Delta\nu_{\text{cav}}} = \frac{\Delta\omega_{\text{fsr}}}{\Delta\omega_{\text{cav}}} \approx \frac{\pi}{1-r^2}. \tag{2.41}$$

From Eq. (2.22b), Eq. (2.40) and Eq. (2.41) one can derive the reflection coefficient is

$$F(\omega) = \frac{i}{\pi}\frac{\delta\omega}{\Delta\nu_{\text{cav}}}. \tag{2.42}$$

Substituting $F(\omega)$ into Eq. (2.38) with the above equation and considering $F(\omega \pm \Omega) \approx -1$, the error signal can be written as

$$\begin{aligned} P_{\text{err}} &\approx -\frac{4}{\pi}P_0 J_0(\beta)J_1(\beta)\frac{\delta\omega}{\Delta\nu_{\text{cav}}} \\ &= -8P_0 J_0(\beta)J_1(\beta)\frac{\delta\nu}{\Delta\nu_{\text{cav}}}, \end{aligned} \tag{2.43}$$

where $\delta\nu = \delta\omega/2\pi$ is the frequency deviation. Note that this approximation is only valid when the conditions of $\delta\omega/\Delta\nu_{\text{cav}} \ll 1$ and high finesse are met. When near resonance, the error signal is proportional to the frequency deviation. The coefficient of proportionality is the frequency discriminant D. For the standard PDH technique,

$$D_{\text{PDH}} = -\frac{8}{\Delta\nu_{\text{cav}}}P_0 J_0(\beta)J_1(\beta). \tag{2.44}$$

Note that this equation is only valid for standard PDH technique. In our experiment we use a modified technique whose frequency discriminant can't be described by this equation. From Fig. 2.13 one can see that the error signal is linear around 0 frequency deviation then suddenly becomes non-linear for higher deviations.

[2] in this equation we have a term of $\frac{\delta\omega}{\Delta\nu_{\text{fsr}}}$ because this term is useful in the equation of the reflection coefficient

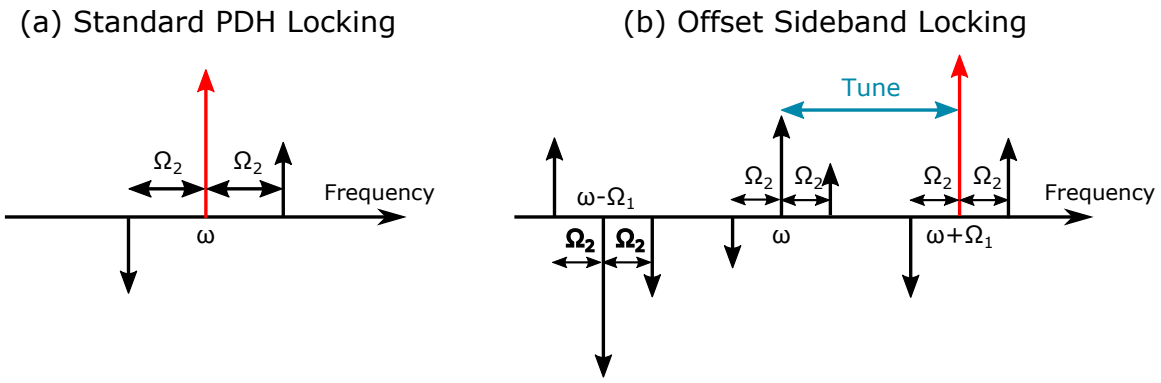

Figure 2.14: Diagram of the laser frequency components with modulation. (a) shows the carrier and the sidebands with the standard PDH modulation. The directions of the arrows indicates the phase. The two PDH sidebands have opposite phases and lower amplitude than the carrier at low modulation depth. The carrier is locked to a cavity mode (red arrow). (b) shows the bands generated by dual modulations. As an example, the offset sideband with higher frequency is locked to a cavity mode (red arrow), the spacing between which and the carrier is tunable.

2.4.3 Offset Sideband Locking

In the last section we have reviewed the standard PDH technique, but this technique has some limits. The major one is the laser frequency can only be stabilised to one of the cavity modes. We have shown that the STIRAP lasers are required to be tunable to search for suitable states for transfer. Therefore, in this section we introduce offset sideband locking (OSB) technique [39] adding tunability to the carrier frequency. This is achieved by locking a sideband to the cavity mode and the laser frequency is tuned by changing the spacing between the sideband and the laser frequency. The diagram of the experiment setup is shown in Section 2.5.1. A small amount of light is picked off and sent to the cavity for locking, the rest of the light is not modulated and has the same frequency as the carrier.

Offset sideband locking is a modification of the standard PDH technique, where additional sidebands are generated in the laser beam and used to stabilise the laser frequency. In this technique, we apply two modulation signals with different frequencies to the beam to modulate its phase. The light field incident to the cavity with two modulations is

$$\tilde{E}_{\text{inc}} = E_0 e^{i(\omega t + \beta_1 \sin\Omega_1 t + \beta_2 \sin\Omega_2 t)}, \tag{2.45}$$

where the modulation depth and the modulation frequency of the first (second) modulation are β_1 (β_2) and Ω_1 (Ω_2). We assume $\Omega_2 > 2\Omega_1$ and $\beta_1 > \beta_2$. Below we will see that the second assumption is the requirement to maximise the frequency discriminant.

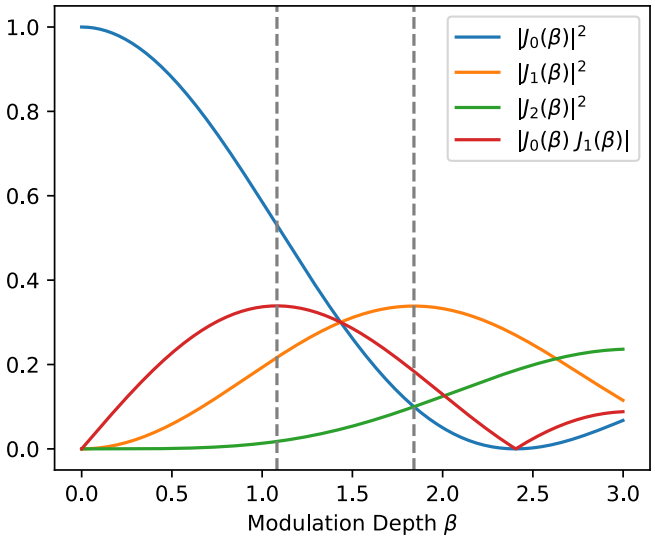

Figure 2.15: The values of the square of the Bessel functions and their product which determine the frequency discriminant of the offset sideband locking. The modulation depths are chosen to maximise the discriminant according to Eq. (2.46). β_1 and β_2 are to be set to 1.841 (the right grey dashed line) and 1.082 (the left gery dashed line), respectively, to maximise $J_1(\beta_1)^2$ and $J_0(\beta_2)J_1(\beta_2)$.

Similar to the last section, this light field can be expanded by Bessel functions of the first kind to first order. The diagrams of the frequency components of the standard PDH locking and offset sideband locking are presented in Fig. 2.14. For standard PDH locking, the carrier (the red arrow) is stabilised to a cavity mode. Two sidebands are generated for stabilisation to which we refer as the "PDH sidebands".

The frequency diagram of one example of sideband offset locking is shown in Fig. 2.14 (b). In this example, the sideband generated by the first modulation with higher frequency (the red arrow) is stabilised to a cavity mode. We refer to the sidebands generated by the first modulation as the "offset sidebands". The spacing between the offset sidebands and the carrier in the frequency domain can be tuned by tuning the modulation frequency Ω_1. To stabilise the offset sideband, two PDH sidebands with opposite phases are generated around them by the second modulation featured by its frequency Ω_2. Note that one can also lock using the offset sideband at lower frequency. This technique allows us to stabilise the laser frequency, tracking the carrier frequency at any frequency between two cavity modes by tuning Ω_1. For a cavity with a free spectral range of 1.5 GHz, the maximum required Ω_1 is 750 MHz. This signal can be easily generated by a function generator with linewidth below 100 Hz.

The frequency discriminant of this technique D_{OSB} is given by [39]

$$D_{\mathrm{OSB}} = \frac{8}{\Delta\nu_{\mathrm{cav}}} P_0 J_1^2(\beta_1) J_0(\beta_2) J_1(\beta_2), \tag{2.46}$$

where $P_0 = \frac{1}{2} c\epsilon_0 |E_0|^2 \times A$ is the power of the light. The high frequency discriminant is crucial for achieving a narrow laser linewidth by stabilisation. Practically, the cavity linewidth is determined by the cavity mirrors and the light power is restricted by the laser power, so we need to choose the modulation depths β_1 and β_2 carefully to maximise the frequency discriminant. Figure 2.15 plots the values of the Bessel functions of the first kind and their product. Accordingly, β_1 and β_2 are to be set to 1.841 and 1.082, respectively. In Section 2.3.3 we have shown that the cavity linewidth of the light at 977 nm is 74(3) kHz. Then we can calculate the frequency discriminant based on this value.

2.5 Experimental Locking Demonstration

In this section, the experiment system used to stabilise the frequency of the STIRAP lasers is presented. We use the offset sideband locking technique to stabilise the laser frequencies. This technique allows the laser frequency to be tunable while minimising the frequency deviation. The parameters of the feedback circuitry are optimised to reduce the laser frequency noise and maximise the lock bandwidth. To characterise the performance of the system, we measure the noise spectra of the error signal both with and without demodulation. The laser linewidth and the lock bandwidth are estimated from that data.

2.5.1 Experimental Setup

Figure 2.16 shows the diagram of the optical system used to lock the lasers to the ULE cavity discussed in Section 2.3.3. This system will be referred to as the STIRAP laser system in the following contents.

In the Fig. 2.16, the laser used to couple the Feshbach state to the excited state in the molecule (pump laser) is denoted by red. The laser to couple the excited state to the ground state (Stokes laser) is denoted by orange. We use two Toptica DL pro External Cavity Diode Lasers as the light sources of the two lasers needed to perform STIRAP. Each laser head has a built-in optical isolator to prevent optical feedback from entering the laser diode. Both lasers can be tuned across a wide frequency range. The pump laser can be tuned from 1490 nm to 1580 nm. The maximum output power behind the isolator is 51 mW. The Stokes laser has the maximum output power of 90 mW behind the isolator

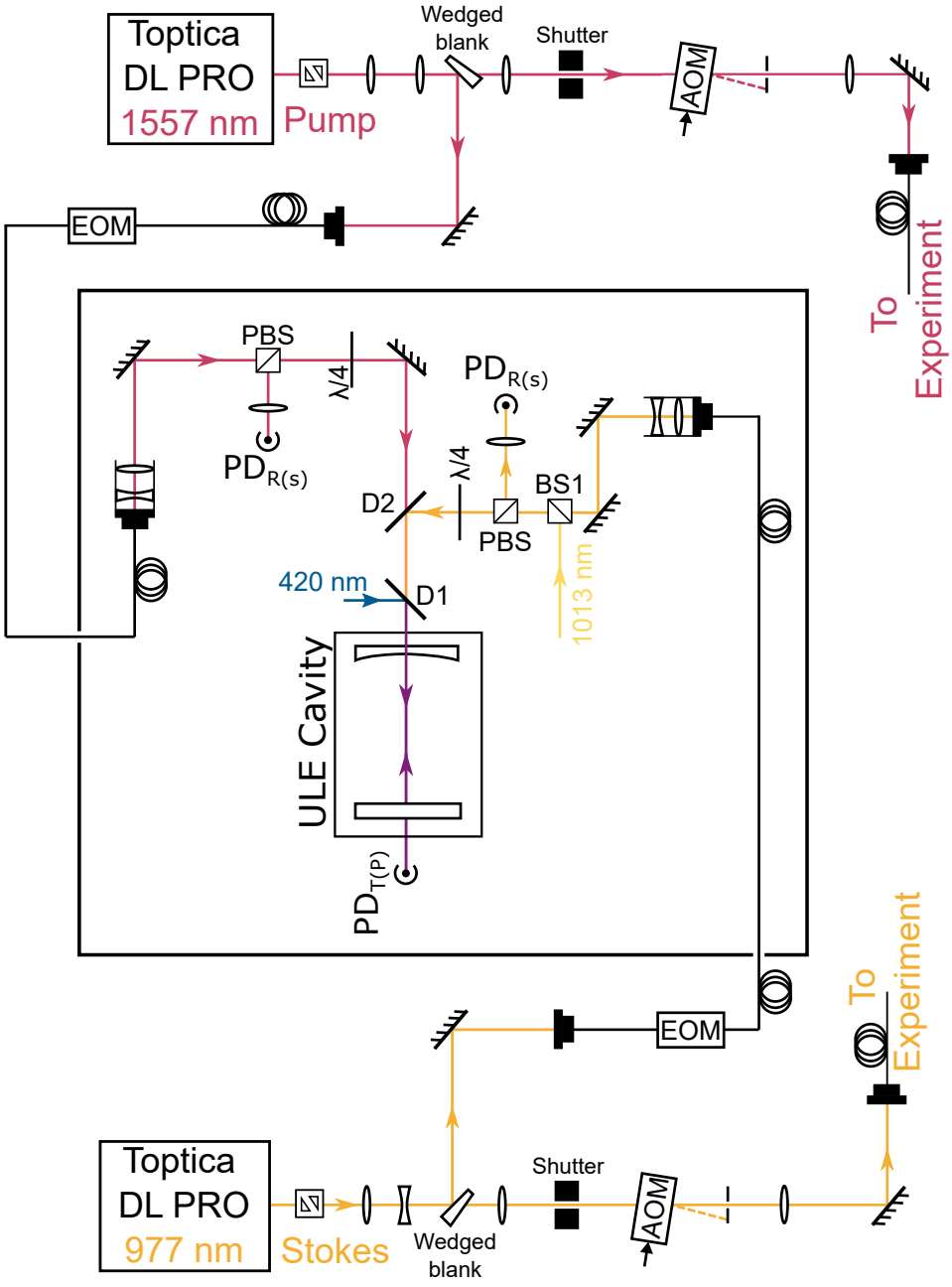

Figure 2.16: The STIRAP laser system. The pump laser at ∼1557 nm (red) and the Stokes laser at ∼977 nm (orange) are locked to the ULE cavity using offset sideband locking. There are another two lasers at ∼420 nm (blue) and ∼1013 nm (yellow) respectively locked to the same cavity. D1 is a dichroic mirror for combining the light from the 420 nm laser with the other beams. BS1 is a non-polarising 50:50 beam splitter for combining the light from the 1013 nm laser with the light from the 977 nm laser. The functions of each component are explained in the main text.

and can be tuned from 930 nm to 990 nm. The pump and Stokes lasers need to couple the weakly-bound Feshbach state and the rovibronic ground state to a common excited state. Previous works have identified the wavelengths corresponding to the transition energies from the Feshbach state to the excited state and from the rovibronic ground state to the excited state are 1556.7804(3) nm and 977.0621(1) nm, respectively [24, 41]. For the characterisation of the locking performance, the pump laser is centred at 1557 nm and the Stokes laser is centred at 977 nm. The absolute wavelengths are measured with Bristol Instruments 621A laser wavelength meter whose operating range is 520-1700 nm and accuracy 20 MHz. Its accuracy was confirmed by measuring the wavelength of laser driving the $5P_{3/2} \leftrightarrow 4D_{5/2}$ transition in Rb at 1529nm [42]. In order to isolate the lasers from changes in the lab environment, the laser heads are placed inside home-made PALIGHT boxes with 30 mm thick foam filling the gap between the box and the laser head to reduce acoustic vibrations coupling to the laser cavity.

The cavity performs the function of the optical reference to which the lasers are referred to stabilise the frequency and is used to narrow the linewidth of the lasers. Hence it is the core of the locking system. The theory and the characterisation of the cavity are presented in Section 2.3.2 and Section 2.3.3, respectively.

The setup for the pump and Stokes lasers are similar. Only a small amount of light is needed for locking. Therefore, after being output from the laser head, $\sim$4% of the laser power is picked off using an uncoated wedged blank and coupled to the fibre EOM before it's sent to the cavity for frequency stabilisation. Another $\sim$4% of the laser power is also picked off and currently blocked but could be sent to a wavemeter to monitor the absolute laser frequency. The rest of the laser power ($\sim$92%) is transmitted and sent to the main experiment. The purpose of the wedged blanks is to deviate the second reflection beam from the first reflection beam and the incident beam. Furthermore, to keep the good polarisation purity of the light from the laser head in both the reflected and the transmitted beam, it is required that the incident angle to the blank must be small enough such that the reflectivity of the s-polarised light and the p-polarised light are similar and the polarisation purity won't be largely affected. In the experiment, the blanks are placed to minimise the incident angle while ensuring the reflected beam is not blocked by the other optics on the table.

The function of the EOM is to modulate the phase of the light in order to generate the sidebands used for locking and offset, which is essential for sideband offset locking. Both EOMs are fibre coupled. The part numbers of the EOM are EOSPACE PM-0K5-10-PFA-PFA-980 for 977 nm and Thorlabs LN65S-FC for 1557 nm. These EOMs are non-resonant and have a bandwidth of 10 GHz, which is wider than the free spectral range of the cavity

and hence can be used to produce a locking sideband at any point in between the cavity modes allowing the laser frequency to be stabilised as well as continuously tunable. They can operate at multiple driving frequencies simultaneously, allowing the PDH and the offset modulation to be applied using the same EOM. They also have low V_π, allowing them to be driven at a relatively low voltage.

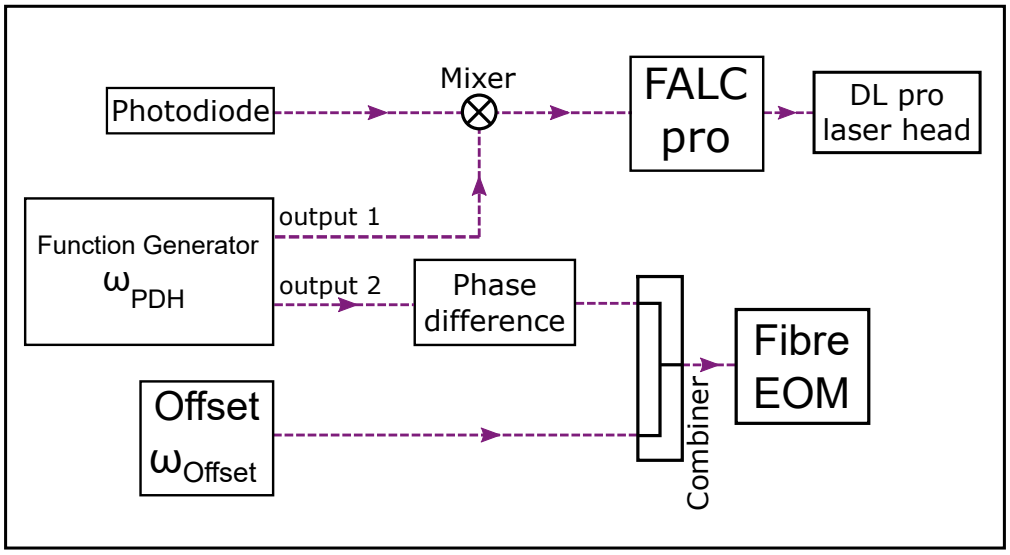

Figure 2.17: The electronic setup to achieve offset sideband locking. The PDH modulation signal from output 2 of the function generator and the offset modulation signal are combined at the combiner and sent to the EOM. The signal from output 1 is sent to the mixer to mix with the signal from the photodiode and to demodulate it to get the error signal. The phase difference of two outputs of the function generator can be set on the function generator control panel. The error signal is sent to a Fast Analog Linewidth Control (FALC) pro for PID control. The mixer is integrated inside the FALC module in practice which sends a signal to the laser head to tune the laser frequency.

The light output from the fibre is modified by the mode-matching cage such that its waist position is at the planer mirror of the cavity and its waist size is 0.25 mm to match the beam with the cavity geometry. The waist size is governed by Eq. (2.23). The 977 nm light is combined with another 1013 nm light (yellow) at BS1 which is a non-polarising 50:50 beam splitter. At the dichroic mirror D2, the 1557 nm laser is combined with the 977 nm and the 1013 nm laser. Then at the dichroic mirror D1, another laser of 420 nm wavelength (denoted by blue) is combined. The photodiodes detecting the photon signals are labelled by the signal type and the photon polarisation. The reflected signal and the transmitted signal are labelled by "R" and "T", respectively and the polarisation (s- and p-light) of the light is further noted in the bracket. Note that it's hard to combine or separate 977 nm laser light and 1013 nm laser light with a standard dichroic mirror

because their wavelengths are too close. Hence they are combined with a 50:50 beam splitter and detected by the same photodiode.

From our experience of setting up STIRAP in another lab, the STIRAP lasers are sensitive to environmental vibrations. It's important to isolate the optical cavity and the fibre EOMs from the vibrations. The cavity is placed on an optical table with a vibration isolation platform in the same lab as the main experiment table. Both EOMs and most of the associated fibres are mounted in a home-made stainless steel mount to prevent the EOM and the fibre from being disturbed by the vibrations. The stainless steel mounts are placed on the same optical table as the cavity.

Light destined for the main experiment passes through an acoustic optical modulator, or AOM[3], and is subsequently transmitted to the main experiment by optical fibres. The first order diffraction beam of the AOM is used in the main experiment. The AOMs are centred at 74 MHz (977 nm) and 80 MHz (1557 nm), respectively. The frequencies of the lasers are up-shifted by the corresponding frequency. The two AOMs can produce the laser pulses needed for STIRAP. The driving signals for intensity control are generated by Direct Digital Synthesis (DDS). The signals are sent to amplifiers (Mini-Circuits ZHL-1-2W+) and control the shape of the intensity curve by changing the diffraction efficiency. The beam can be blocked by the shutter before the AOM to prevent light leakage.

The electronic setup of the 977 nm and the 1557 nm laser are identical. Figure 2.17 shows the set-up diagram for offset sideband locking to the cavity. The PDH modulation signal ω_{PDH} and the signal to mix with the photodiode signal are both from the RIGOL DG822 2 channel 25 MHz function generator but using different outputs. The two channels of the function generator are controlled independently. The frequencies of the two outputs are set to be the same and the phases can be tuned on the control panel of the function generator. To control the phase difference between the two outputs, the phase of one output stays fixed and the phase of the other one is tuned. Every time the function generator is switched on, the phase difference is adjusted to maximise the error signal amplitude. In terms of PDH modulation frequency ω_{PDH}, the lasers are modulated at $2\pi \times 24.1$ MHz (977 nm) and $2\pi \times 18.95$ MHz (1557 nm).

The offset modulation signal ω_{offset} is from another RF signal generator (Windfreak SynthHD V2) which can output frequencies up to 15 GHz. This frequency is higher than the free spectral range of the cavity and can produce a locking sideband at any point in between the cavity modes. The PDH modulation signal and the offset modulation signal are combined at the combiner(Mini-Circuits ZAPD-2-252-S+) and sent to the fibre EOM.

[3]ISOMET 1205C-843 for 977 nm and ISOMET M1205-P80L-0.6 (1550nm) for 1557 nm

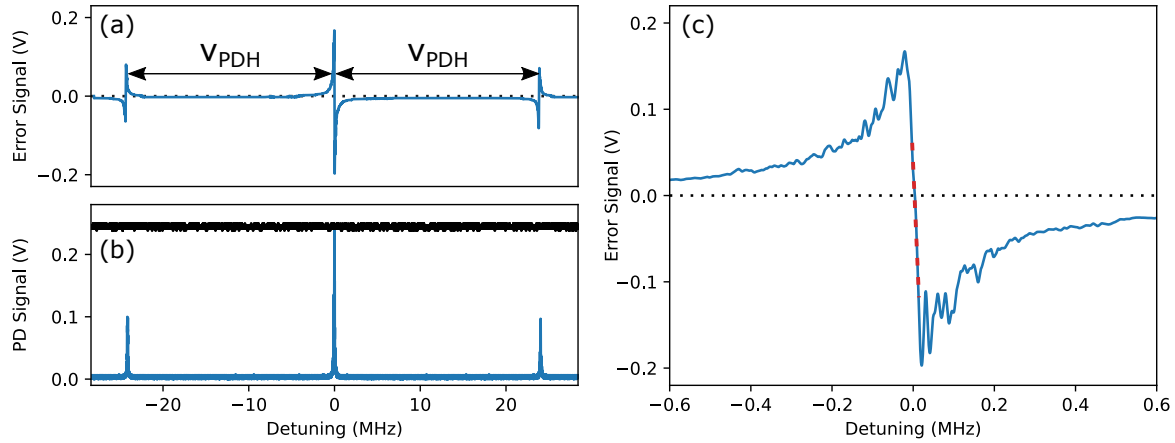

Figure 2.18: (a): The PDH error signal at one of the offset sidebands. (b): The cavity transmission signal of the PDH carrier and the sidebands generated by PDH phase modulation in terms of the detuning from the carrier frequency (blue) and the same signal recorded for 20 ms when the laser is locked (black). The two blue lines in (a) and (b) share the same x-axis. The x-axis of the black line is time and is omitted in the figure and its y-axis is the same as the blue line in (b). The dotted line crosses zero volts. The modulation frequency is $\omega_{\mathrm{PDH}} = 2\pi \times 24.1$ MHz. It can be seen that the detuning of the sidebands from the carrier is the same as the modulation frequency. A zoom onto the centre slope of the error signal is shown in (c). The red dashed line is the fitting to a straight line.

The choice of the modulation depth of the two modulations are described in Section 2.4.3. In the experiment the modulation depths are set by the voltage of the modulation signals. The modulation depth is 1.08(2) for PDH modulation and 2.11(4) for offset modulation for the 977 nm laser. For 1557 nm laser, by the time this thesis is written, it hasn't been properly modulated and locked. The reflected light signal from the cavity is received by the 800-1700 nm photodiode (Thorlabs PDA05CF2), the bandwidth range of which is $0 - 150$ MHz. The photodiode has a quoted responsivity with gain of $\sim$4.7 V/mW at 977 nm and $\sim$10.5 V/mW at 1557 nm. The reflected light of the 1557 nm laser and the 977 nm laser are detected with separate photodiodes of the same model. Note that as shown in Fig. 2.16, the 977 nm laser and the 1013 nm laser are detected on the same photodiode. These two lasers need to be locked at the same time. To avoid causing harmonic mixinf of the signals, ω_{PDH} of the 977 nm laser and the 1013 nm laser must be set as far apart as possible. The 1013 nm laser is modulated at 13.9 MHz. Thus when the signal from the photodiode is demodulated at the mixer, the error signal of the different lasers is extracted with the corresponding frequency ω_{PDH} applied to the mixer.

The output of the mixer is processed by the Fast Analog Linewidth Control (FALC)

pro which is a fast laser locking module from Toptica. It has a quoted 50 MHz bandwidth and < 10 ns signal delay. This module has a built-in mixer and a PID regulator. The error signal is processed by the module which produces a signal sent to the laser head to correct the laser frequency. Behind the mixer, there is a signal at $2 \times \omega_{\mathrm{PDH}}$ in addition to the error signal which is at DC. To filter the signal at higher frequency, a low-pass filter is needed. But instead of adding a physical low-pass filter, the piezo in the laser head plays the role of a low-pass filter due to its limited response time.

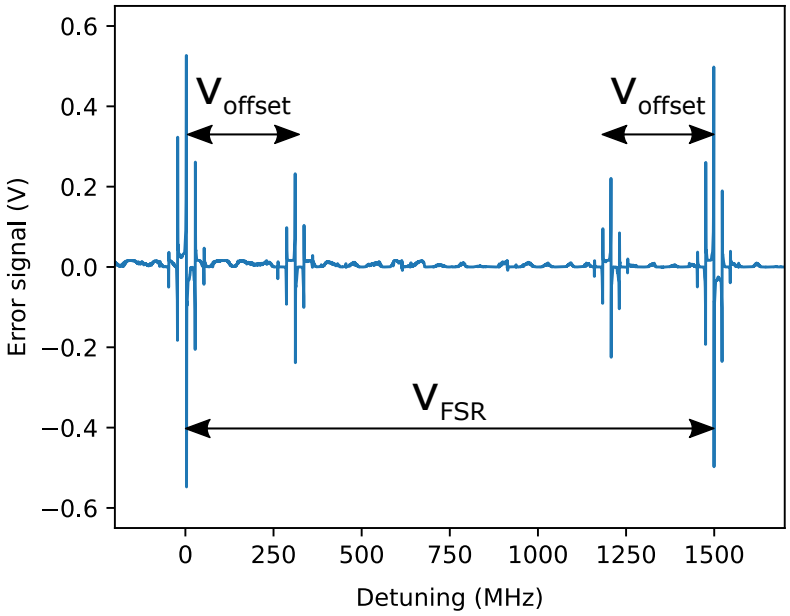

Figure 2.19: An example of the error signal that is generated by dual phase modulation of the light using an EOM. The laser is scanning over a large frequency range to include two adjacent cavity modes in one scan. The leftmost and rightmost signals are the carriers and are at the frequencies of the cavity modes. The frequency difference between them is the free spectral range of the cavity. The two smaller signals in the middle are the sidebands and are generated by the offset modulation. Their detuning from the carrier is set be the offset modulation frequency. Here the amplitude of the sidebands are tuned lower than that of the carriers to show their relations more clearly.

Figure 2.18 shows the error signal measured on the oscilloscope from the monitor port on FALC and the transmission signal of the cavity including the PDH carrier and sidebands. The frequencies are the detuning from the carrier frequency. The modulation frequency is $\omega_{\mathrm{PDH}} = 2\pi \times 24.1$ MHz. The error signal is measured with a low pass filter (Mini-Circuits BLP-5+, 5 MHz) and is further processed by a software low pass filter in Python, threshold 60 kHz. One can clearly see that the error signal crosses zero at the

frequencies of the carrier and the sidebands. The transmission signal when the laser is locked is also shown. All the light is transmitted with small intensity fluctuations around the peak. A zoom-in to the centre slope of the error signal is given in the right panel. The steep slope close to zero detuning is approximately linear and can be fitted to a linear function to find the gradient of the slope to which the laser frequency is stabilised (red dashed line). From Eq. (2.46) one can calculate the frequency discriminate which is approximately the gradient of the centre slope. Using the measured cavity finesse and FWHM in Section 2.3.3 and the modulation depth, we derive that the frequency discriminant $D_{\mathrm{DSB}} = 10.4(6)$ V/MHz. To measure the gradient, 19 error signals are recorded within 5 hours and the centre gradient of each is calculated using the method described above. The mean value and standard deviation are then calculated. This measurement yields a gradient of 11(1) V/MHz ignoring the minus sign as the direction of the slope is set by the internal FALC design to give the correct feedback to the laser. The standard error is quoted. The error signals over a wider frequency range is given in Fig. 2.19 where two sets of cavity peaks are shown. One of the offset sidebands is locked to the cavity and the carrier frequency can be tuned by changing the offset frequency.

2.5.2 Locking Performance

We expect the laser linewidths below 1 kHz can be achieved using the PDH locking technique with our cavity. To characterise the performance of the lock, one needs to measure the laser linewidth with precision below 1 kHz. To do this, one of the techniques is the self-heterodyne method [43]. In this method, the laser light is split into two paths, one of which is delayed with a fibre and the light frequency-shifted with respect to the other before both beams are recombined, and the resulting beat response is measured. The laser linewidth can be inferred from the width of this beat spectrum [44]. The coherence length of the laser of 1 kHz linewidth is $\sim$50 km, which means the fibre must be longer than 50 km. This is impractical. One can send the laser through the same fibre multiple times to delay it [45], but the total loss will be too high as there is loss each time the laser passes through the fibre. Adding a fibre amplifier can compensate this but the amplifier itself will introduce new noise so the true linewidth still can't be measured.

Here, we use another method to the optimise the locking parameters and estimate the laser linewidth. A part of the error signal before the mixer is extracted with a directional coupler (Mini-Circuits ZFDC-15-6+, CPL=15 dB at 26 MHz) and measured in a spectrum analyser. Then one can adjust the PID parameters to push away the servo bumps and reduce the noise around the centre. Figure 2.20 (a) shows the noise spectra when the

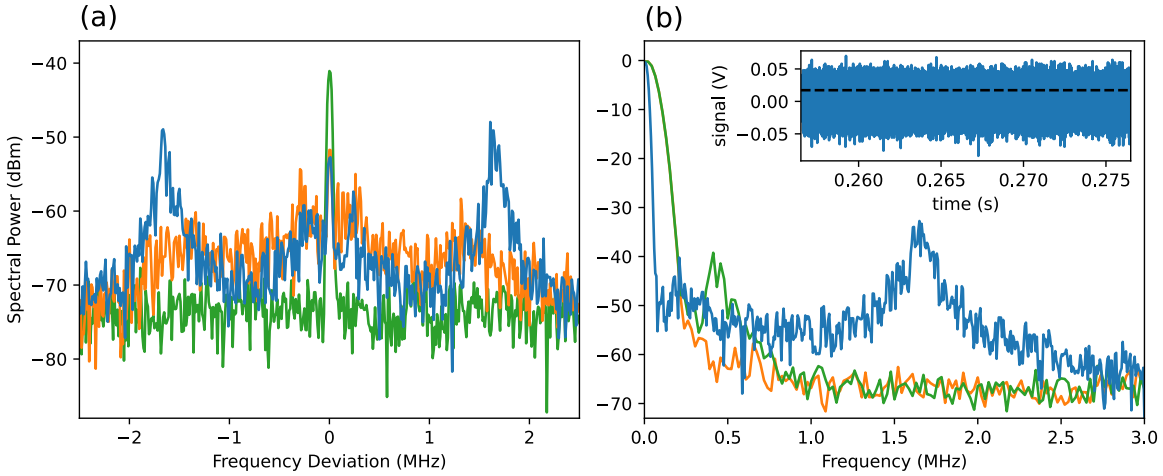

Figure 2.20: The noise of the lock. (a) The noise spectra measured before the mixer. The x-axis is the frequency deviation from the PDH modulation frequency. The noise spectra of the unlocked laser (green), optimum lock (orange) and lock with high gain (blue) are shown. (b) The noise spectrum of the optimum lock measured from the error signal after the mixer of the locked laser (blue); the background noise from the photodiode and the spectrum analyser (orange) and the noise from the error signal without locking (green). The insert shows the same signal measured on a oscilloscope over 2ms, with the black dashed line showing the RMS voltage.

laser is unlocked (green), locked with the optimum parameters (orange) and locked with the gain being too high (blue). The x-axis is the frequency deviation from the PDH modulation frequency 24.1 MHz. With the optimum parameters the noise up to the servo bump is suppressed comparing to the unlocked laser. The optimum locking parameters suppresses the noise up to the servo bump comparing to the unlocked laser and pushes away the servo bump without causing lock oscillation. The lock starts to oscillate when the gain is too high and the noise around the modulation frequency is increased. The peak is at $\sim$1.7 MHz indicating the lock bandwidth is $\sim$1.7 MHz.

Figure 2.20 (b) shows the error signal measured behind the mixer when the laser is locked. The peak is at $\sim$1.7 MHz which agrees with the bandwidth measure before the mixer. The pulse duration of STIRAP is $\sim$ 10 μs corresponding to $\sim$1 MHz. Hence we care about the noise around 1 MHz the most. The insert shows the same signal measured on a oscilloscope with a 5 MHz low pass filter in 2 ms which is much longer than the pulse duration. The RMS voltage is 0.017 V. The voltage fluctuation corresponds to the laser frequency fluctuation. From the gradient of the error signal central slope that is calculated in Section 2.5, one can estimate the laser linewidth is about 1.5(3) kHz.

As an outlook, there are two additional methods we can employ to estimate the laser

linewidth. One: in our previous experiment of RbCs quantum gas in a different lab, a very similar laser system for STIRAP has already built [24] and ground state RbCs molecules have been successfully produced [16]. We can estimate the linewidth with the same method as above and compare the results. Two: in addition the previous mentioned lab, we are also building a similar laser system for STIRAP for quantum site microscopy of RbCs in a different lab. Hence there will be three laser system with very similar set-up. we can beat the lasers in the different labs against each other and measure the width of the beating signal which gives an idea of the maximum linewidth of all the lasers.

2.6 Main Experiment

In order to perform STIRAP, the lights from pump and Stokes lasers need to be transferred to another optical table (referred to as the main table) on which the vacuum apparatus for the atoms is placed and the main experiment is conducted. In this section, we will discuss the setup on the main table to combine the lights and to focus them to the atomic cloud. The alignment method will be introduced, too.

2.6.1 Experimental Setup

The whole laser system of the experiment is complex as different laser are needed for cooling and trapping different species of atoms. Additional lasers are required to excite atoms to their Rydberg state as this is a hybrid platform of molecules and Rydberg atoms. Those lasers are irrelevant to STIRAP and are not the focus of this thesis. Since some of the laser beams are combined with the STIRAP light before being sent to the atoms, they will be mentioned briefly. Figure 2.21 shows the diagram of the setup to transfer the beams to the the atoms. The pump and Stokes light are both sent from the "STIRAP" table (diagram is in Fig. 2.16) using polarisation maintaining (PM) optical fibres. There are 5 beams combined in total in Fig.2.21. Each beam is shown in one colour. All the beams are combined by the dichroic mirrors (D1-D3), except the Stokes light (977 nm) and the light at 1013 nm which have different polarisation and are combined at the polarised beam splitter (PBS). The optical traps trapping the atoms and the molecules are in the vacuum chamber. There is a flipper mirror in front of the vacuum chamber. This can be used to reflect the light onto a camera which is situated roughly at the same distance from the flipper mirror as the distance from the flipper mirror to the atoms. This allows us to characterise the beam at the position of the atoms.

It is important to have as high a Rabi frequency as possible to reduce the pulse time

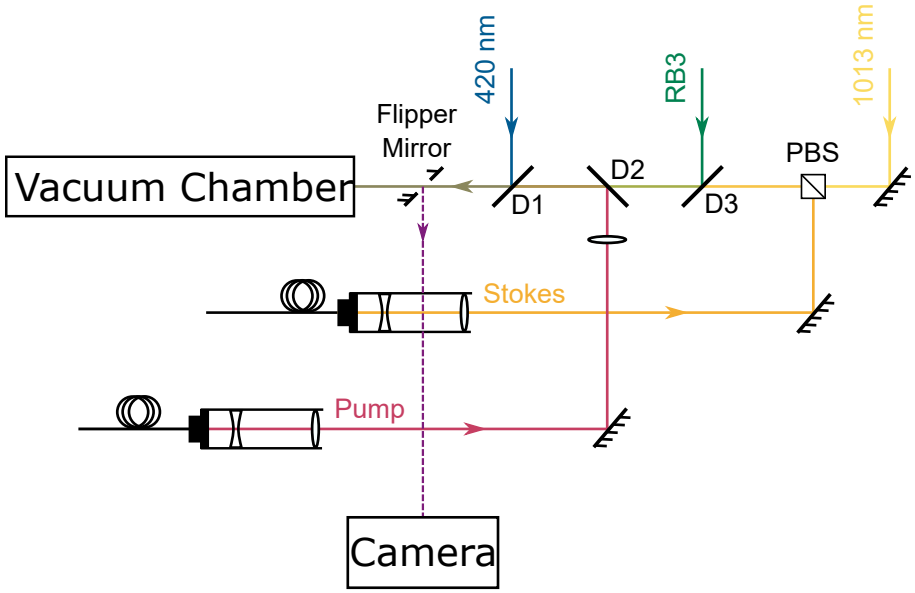

Figure 2.21: The diagram of the STIRAP laser system on the experimental table. The pump (red) and Stokes (orange) beams are combined with 3 other beams and sent to the atomic cloud. The cage systems are employed to focus the pump and Stokes beams to the atoms, the details of which are given in the main text. The Stokes light at 977 nm is combined with the light at 1013 nm by a polarised beam splitter (PBS). The other beams are combined by the dichroic mirrors (D1-D3). Before the vacuum chamber that contains the atoms, there is a flipper mirror to reflect the beams to a camera placed roughly at the same distance from the flipper mirror as that from the mirror to the atoms for characterising the beams. The details of the vacuum are omitted.

during the STIRAP process. The short duration is desired because it makes the transfer more robust to dephasing given the same dephasing rate. The atoms and the molecules are trapped in optical tweezers whose sizes are $\sim$1 μm. Then we aim to make an array of tweezers to exploit the rich physics provided by the molecules. The STIRAP beams need to be tightly focused to increase the Rabi frequency but the waist should not be smaller than the size of the tweezer array. Due to space limitations on the main table, the STIRAP light outputs (the fibre collimators) must be placed $\sim$900 mm away from the atoms, which means the pump and the Stokes lights must be tightly focused at a long distance. To achieve this, the pump and Stokes beams are shaped using a set of lenses before combining with the other beams. With this optical system, we are able to focus the beams as well as adjust the axial and radial position of the beam waist.

Due to the time scale of this project, only the pump light has been focused. The light from the pump laser is first diverged by a concave lens then converged by a convex lens to nearly collimated. It is then focused by another convex lens just in front of the

dichroic mirror D2. The purpose of this is to reduce aberration and beam apodisation on the further optics. To simplify the alignment, the collimator and the first two lenses are assembled in a cage system. The concave lens is mounted on a Z-axis translation mount which offers repeatable Z-axis travel within the cage system (Thorlabs SM1ZA). Moving this mount along the cage changes the separation between the lenses and the collimator in the cage system and thus achieves the fine adjustment of the beam waist position without largely affecting its size. The radial position of the beam can be tuned by the two mirrors with the differential adjuster (Thorlabs DM22) which can create a fine adjustment of 25 μm/revolution, making the increment as small as 0.5 μm possible. This means the radial waist position can by moved by 500 μm/revolution, allowing us to align the pump beam to within $\pm$10 μm. The horizontal size of the waist is 67(3) μm; the vertical size is 40.2(9) μm. This beam size can accommodate $\sim$10 optical tweezers providing the spacing between the tweezers is around 4 μm which is the spacing we commonly have. The light intensity is $3.8(3) \times 10^5$ mW/cm^2 with 16 mW before entering the chamber.

The Stokes light is also first expanded by a concave lens after outputted from the fibre collimator then focused by a convex lens. To simplify the alignment, the collimator and the two lens are assembled in a cage system, too. The waist size can be tuned by changing the separation between the two lenses. The radial position can be tuned by the PBS and the mirror. The PBS is mounted on a kinematic mount with two adjusters (Thorlabs KM100PM). We expect to achieve a beam waist of $\sim$65 μm. The correspond light intensity is 3.8×10^5 mW/cm^2 with 25 mW before entering the chamber.

2.6.2 Alignment to the Molecules

It is important to align the beams to the atoms within a small fraction of the beam size to get the highest Rabi frequency for the corresponding transitions. Here the technique of aligning the STIRAP beams to the atoms is described. For coarse alignment, the STIRAP beams are overlapped with a previously aligned 420 nm beam as shown in Fig. 2.21. This light is for exciting Rb atoms to a Rydberg state and has been previously aligned by minimising the number of the atoms in the MOT when the light at 420 nm is switched on, because this light can disturb the MOT and stop the atoms from being trapped. To overlap the other beams with it, the flipper mirror is flipped so the lights are reflected to the direction of the camera (Thorlabs CS165MU/M) that responds to the light with $\sim$300 nm to 1100 nm wavelength. For the Stokes light at 977 nm, it can be overlapped with the 420 light on camera. For the pump light at 1557 nm, we use a knife edge instead. First only the 420 nm light is switched on and the knife edge is set to the centre of the

beam where the power drops to one half of the total power. Then keeping the knife edge position fixed, the 420 nm light is switched off and the pump light is switched on and centred at the knife edge where its power also drops to one half. This process is done in both vertical and horizontal dimension. Only the pump beam is aligned when this thesis is written.

After the coarse alignment, the fine alignment can be done by measuring the one-photon and two-photon spectroscopy signal of the molecule on a strong transition. The pump light can be aligned by minimising the pulse time and laser power used to remove the molecules. The Stokes light can be aligned by minimising the pulse time and laser power needed to obtain the ground state molecules.

2.7 Conclusion

2.7.1 Summary

In this chapter, we discussed the details of STIRAP - the technique to transfer the molecules to their ground state. We reviewed the theory of STIRAP. We introduced the offset sideband lock technique along with the cavity theory. We described the laser system to stabilise the laser frequencies and to perform STIRAP. The laser linewidth is estimated to be $\sim$1.5(3) kHz when locked using this technique. The lock bandwidth is estimated to be $\sim$1.7 MHz. We developed the method to align the beams to a small focus at the molecular sample to maximise the Rabi frequencies. We developed a system to control the light intensities to deliver the pulses needed for STIRAP. We are ready to perform molecular spectroscopy and transfer of molecules to the ground state using STIRAP.

Chapter 3

AC Stark Effect, Molecular Polarisability and Magic Conditions

In this chapter, we introduce the effect of the trapping laser on the energy of the rotational states of the molecules through the AC Stark effect, and demonstrate a "magic trap" which eliminates the decoherence caused by this effect.

3.1 AC Stark Effect

3.1.1 Molecular Polarisability and the AC Stark Effect

In this section, we derive the Hamiltonian to describe the AC Stark effect in a diatomic molecule. The coordinate system used in this work to describe the molecular polarisability and the laser polarisation is shown in Fig. 3.1. We choose the z-axis as the quantisation axis in which direction the magnetic field is applied. We assume a linearly polarised light propagating along the x-axis. The direction of the electric field (E_{DT}) of the light, i.e. the polarisation direction is in the yoz plane. The polarisation has an angle to z of β. The inter-atomic axis of the molecule lays at an angle θ to z and θ' to the light polarisation. In the molecular frame, it's important to note the polarisability components parallel to the axis $\alpha_{\parallel}$, and the component perpendicular to the axis $\alpha_{\perp}$, which are typically different.

The molecular polarisability $\boldsymbol{\alpha}$ is a tensor in general, describing the polarisation of the molecule in three directions. In the molecular frame, it can be written as

$$\boldsymbol{\alpha} = \begin{pmatrix} \alpha_{11} & \alpha_{12} & \alpha_{13} \\ \alpha_{21} & \alpha_{22} & \alpha_{23} \\ \alpha_{31} & \alpha_{32} & \alpha_{33} \end{pmatrix}, \tag{3.1}$$

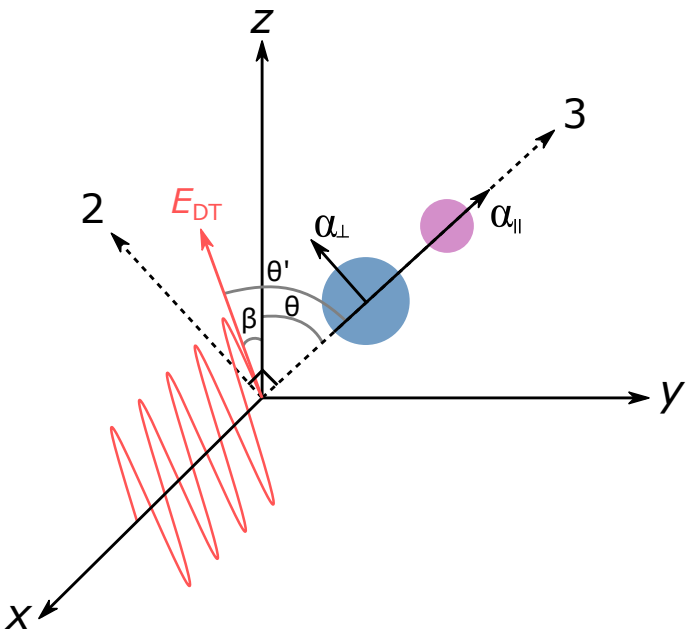

Figure 3.1: The coordinate system to describe the polarisability of the molecule and the laser polarisation. x, y, z axes form the laboratory coordinate system. z is the quantisation axis. Assume a linearly polarised light propagating along x, the electric field of the light is E_{DT} in the yoz plane and has an angle of β to z. Assume the molecule is also in the yoz plane. 1, 2 and 3 are the axes of the molecule's coordinate system. 1 overlaps with x. The angle between the inter-atomic axis of the molecule and z is θ, between inter-atomic axis and the laser polarisation is θ'. $\alpha_\parallel$ and $\alpha_\perp$ are the polarisability components along and perpendicular to the inter-atomic axis of the molecule, respectively. Another $\alpha_\perp$ is parallel to x and is not shown in this figure.

where the subscripts 1, 2, 3 are the axes of the molecular coordinate system as shown in Fig. 3.1. For a diatomic molecule in a coordinate system shown in Fig. 3.1, we have $\alpha_{11} = \alpha_{22} = \alpha_\perp$ and $\alpha_{33} = \alpha_\parallel$, all the other elements are zero. Then we can simplify the polarisability tensor in Cartesian coordinates to

$$\boldsymbol{\alpha} = \begin{pmatrix} \alpha_\perp & & \\ & \alpha_\perp & \\ & & \alpha_\parallel \end{pmatrix}. \tag{3.2}$$

The molecular polarisability interacts with the oscillating electric field of the off-resonant light in an optical trap. We assume that the light is polarised along the z-axis such that $\beta = 0$, $\theta = \theta'$. The electric field seen by the molecule in its own frame is

therefore

$$\boldsymbol{E} = E \begin{pmatrix} 0 \\ \sin\theta \\ \cos\theta \end{pmatrix}, \tag{3.3}$$

where E is the magnitude of the electric field of the trap light. This is related to the intensity of the light I by

$$I = \frac{1}{2}\epsilon_0 c E^2, \tag{3.4}$$

where ϵ_0 is the permittivity of free space and c is the speed of light.

Now we are able to construct the Hamiltonian of the AC Stark effect H_{AC} using [46]

$$H_{\mathrm{AC}} = -\boldsymbol{E} \cdot \boldsymbol{\alpha} \cdot \boldsymbol{E}. \tag{3.5}$$

Substituting Eq. (3.2) and Eq. (3.3) into Eq. (3.5) and replacing E^2 by the intensity yields

$$H_{\mathrm{AC}} = -(\alpha_{\parallel}\cos^2\theta + \alpha_{\perp}\sin^2\theta) \times \frac{2I}{\epsilon_0 c}. \tag{3.6}$$

At this point we choose to define new terms to describe the polarisability of the molecule

$$\alpha^{(0)} = \frac{1}{3}(\alpha_{\parallel} + 2\alpha_{\perp}), \tag{3.7a}$$

$$\alpha^{(2)} = \frac{2}{3}(\alpha_{\parallel} - \alpha_{\perp}). \tag{3.7b}$$

Here, $\alpha^{(0)}$ is the isotropic polarisability and describes the component of the polarisability that does not depend on the orientation of the molecule with respect to the trap light. Conversely, $\alpha^{(2)}$ is the anisotropic component of the polarisability and therefore does depend on the orientation of the molecule. Using these newly defined terms, Eq.(3.5) can be written as

$$H_{\mathrm{AC}} = -[\alpha^{(0)} + \alpha^{(2)} P_2(\cos\theta)] \times \frac{2I}{\epsilon_0 c}, \tag{3.8}$$

where $P_2(\cos\theta)$ is the second associated Legendre polynomial, given by $P_2(\cos\theta) = (3\cos^2\theta - 1)/2$. Comparing Eq. (3.6) and Eq. (3.8) to the energy of a distributed charge in the light field $\varepsilon \propto -\alpha I$, one can see that the total polarisability $\alpha(\theta)$ is

$$\alpha(\theta) = \alpha_{\parallel}\cos^2\theta + \alpha_{\perp}\sin^2\theta = \alpha^{(0)} + \alpha^{(2)} P_2(\cos\theta). \tag{3.9}$$

Now we calculate the matrix elements of the AC Stark Hamiltonian in the basis of $|N, M_N\rangle$, the rotational angular momentum and its projection along z. The wavefunctions in this basis are simply the spherical harmonic functions. Meanwhile, $P_2(\cos\theta)$ is proportional to a spherical harmonic $Y_{2,0}$. Though we assumed the polarisation direction is along z before, this is not always the case generally, hence to obtain a more general

expression, we need to rotate the polarisation by an angle β by multiplying $Y_{2,0}$ by the reduced Wigner rotation matrix $d^2_{M,0}(\beta)$ as the polarisation is only rotated about x. Then we can derive the matrix elements by integrating. The matrix elements are [47]:

$$\begin{aligned}
&\langle N', M'_N|\, I\alpha\, |N, M_N\rangle \\
&= I\alpha^{(0)}\delta_{NN'}\delta_{M_N M'_N} \\
&+ I\alpha^{(2)} \sum_M d^2_{M,0}(\beta)(-1)^{M'_N}\sqrt{(2N+1)(2N'+1)} \\
&\times \begin{pmatrix} N' & 2 & N \\ 0 & 0 & 0 \end{pmatrix} \begin{pmatrix} N' & 2 & N \\ -M'_N & M & M_N \end{pmatrix},
\end{aligned} \tag{3.10}$$

where the first term is the isotropic energy, the second term is anisotropic, and the symbols in the brackets in the second term are Wigner $3j$-symbols. The matrix element is non-zero only when the following three conditions are all satisfied: $|N' - N| \in \{0, 2\}$, $0 \leq |M'_N - M_N| \leq 2$ and $M = M'_N - M_N$. The isotropic component $\alpha^{(0)}$ shifts all the diagonal elements by the same amount and hence doesn't affect the transition energy, though it contributes to optical trapping. The anisotropic component $\alpha^{(2)}$ has non-zero off-diagonal elements which can mix the different hyperfine states in the excited rotational states. For $N = 0$, the anisotropic term is zero, so only $\alpha^{(0)}$ contributes to the polarisabilities of all the hyperfine states, and $\alpha^{(0)}$ is the same for all the rotational states. For $N = N' = 1$, if we neglect the off-diagonal elements in N, the matrix element with $M_N, M'_N = 0, +1, -1$ is [47]

$$\begin{aligned}
&\langle 1, M'_N|\, I\alpha\, |1, M_N\rangle \\
&= I\alpha^{(0)} + \frac{I\alpha^{(2)}}{5} \begin{pmatrix} 2P_2(\cos\beta) & -\frac{3}{\sqrt{2}}\sin\beta\cos\beta & +\frac{3}{\sqrt{2}}\sin\beta\cos\beta \\ -\frac{3}{\sqrt{2}}\sin\beta\cos\beta & -P_2(\cos\beta) & -\frac{3}{2}\sin^2\beta \\ +\frac{3}{\sqrt{2}}\sin\beta\cos\beta & -\frac{3}{2}\sin^2\beta & -P_2(\cos\beta) \end{pmatrix},
\end{aligned} \tag{3.11}$$

where all the angular dependence is encoded in β. All the diagonal terms of the matrix have the $P_2(\cos\beta)$ dependence. Therefore all the diagonal elements can be set to zero by tuning the polarisation $\beta_0 \approx 54.7°$. At this angle all the diagonal elements are removed, but the off-diagonal terms still play a role and can lead to higher-order shifts in the energies.

3.1.2 Electronic Transitions

Long coherence times between rotational states are essential for most applications of polar molecules, e.g. [48]. The energy of the dipole-dipole interaction between RbCs molecules in a lattice will be of order ~ 1 kHz. Hence the coherence time must be at least 1 ms

for experiments to be sensitive to these interaction. The rotational coherence time can be limited by the trap-induced light shift of the transitions [49]. In the last section we saw that, $\alpha^{(2)}$ mixes the different hyperfine states in the rotationally excited states, and the energy shifts and couplings between states of the molecules in an optical trap are affected by both the light intensity and the polarisation. However, what we have not yet considered is that the magnitude of $\alpha^{(2)}$ depends on the frequency (or wavelength) of the trap light. In this section we investigate reducing the light shift of the rotational transitions of RbCs molecules by tuning $\alpha^{(2)}$ to zero by a trapping laser at the "magic laser frequency".

We first briefly introduce the the molecular term symbols for the diatomic molecules. In those molecules, the electronic spin and orbital angular momenta are conserved. Only unfilled subshells contribute to those momenta. In general the molecular term symbol take the following form:

$$n^{2S+1}\Lambda_{\Omega}^{(+/-)}, \tag{3.12}$$

where n is analogous to the principle quantum number for atoms and uses capital letters X, A, B, C,... for singlet states and lower case letters a, b, c,... for triplet states in (typically) ascending order of energy with X conventionally being the lowest state; S is the total spin angular momentum quantum number, Λ is the quantum number of the total orbital angular momentum of the electrons about the internuclear axis, $\Lambda = 0, 1, 2, 3$ corresponds to $\Sigma, \Pi, \Delta, \Phi$; the subscript Ω is then the axial projection of the electronic angular momentum and nuclear spins; the superscript $+/-$ applies only to Σ states labeling the symmetry of the electronic wavefunction with respect to reflection in a plane containing the nuclei. So the lowest RbCs molecular electronic state is written as $X^1\Sigma^+$.

The molecule-frame polarisabilities $\alpha_\parallel, \alpha_\perp$ depend on the laser frequency. In particular, tuning close to ${}^1\Sigma \rightarrow {}^1\Sigma$ electronic transitions will affect $\alpha_\parallel$, while tuning close to ${}^1\Sigma \rightarrow {}^1\Pi$ transitions affects $\alpha_\perp$. To develop a rotationally magic trap, we consider a transition from the ground electronic state $X^1\Sigma^+$ to the excited triplet state $b^3\Pi_0$. The $X^1\Sigma^+$ state is the ground electronic state. The transition from a single state to a triplet state is usually forbidden by selection rules. But the $b^3\Pi_0$ state is coupled to the single state $A^1\Sigma^+$ by spin-orbit coupling, therefore, the states in the ground electronic state $X^1\Sigma^+$ can be coupled to the lowest states of the $b^3\Pi_0$ state which have a small admixture of the $A^1\Sigma^+$ state. This mixing is crucial to enabling STIRAP from the triplet Feshbach state to the singlet ground state [16]. Transitions to states at the bottom of the $b^3\Sigma_0$ potential are particularly narrow, facilitating optical trapping with the laser near this frequency with relatively low photon scattering rates. As we are driving the transition to the admixed component, tuning close to this transition only affects $\alpha_\parallel$.

To eliminate the decoherence caused by the AC Stark shift of the trapping laser, we will look at the molecular polarisabilities and the AC Stark shift at laser frequencies near these transitions in Section 3.2 and end up with identifying a "magic frequency" for rotational states. The resonance transition frequency from the lowest rovibrational state ($v = 0, N = 0$) in the $X^1\Sigma^+$ state to the $(v', N' = 1)$ state in the $b^3\Pi_0$ state is referred to as $\omega_{v'}$. v', N' denotes the vibration and rotation quantum numbers for the target electronically excited state in $b^3\Pi_0$. A set of theoretical and experimentally measured transition frequency values are given in Table 3.1. When near resonance, the laser frequency ω is referred to as the detuning from the transition frequency $\Delta_{v'} = \omega - \omega_{v'}$. In this work, the detuning $\Delta_{v'} < 2\pi \times 10$ GHz is describes as near-resonance and medium-detuned otherwise.

3.2 Theory of the Magic Trap for RbCs

3.2.1 Magic Conditions for $(N = 0,\ M_N = 0) \rightarrow (N = 1,\ M'_N = 0)$ Transition

Near-resonance Polarisabilities for $N = 0$ and $N = 1$ States

In this section, we look at the magic condition where the polarisabilities of the $N = 0$ and $N = 1$ ground states are the same by looking for the laser frequencies at which the anisotropic component of polarisability $\alpha^{(2)}$ of each state goes to zero. We examine both near-resonance and medium-detuned regimes to find the optimum detuning near the transitions from $X^1\Sigma^+$ potential to $b^3\Pi_0$ potential. The theory framework of this section is proposed by Guan *et al.* in Ref. [49].

We first introduce how the RbCs molecular states are labelled. In the previous section, the label for the electronic states was already explained. For a given electronic state, there are multiple vibrational, rotational and hyperfine states. The vibrational states of a RbCs molecule is determined by the vibrational motions of the Rb and Cs atoms relative to each other in a diatomic molecule. For a given electronic state, the vibrational states are labelled by letter v. The transition frequencies between vibrational states are typically $\sim$ THz, much smaller than those between electronic states. For a given vibrational state, a molecule can experience different rotational motions and rotational angular momenta due to the rotation of the atoms over an axis that is not parallel to the interatomic axis. This type of motions corresponds to the molecular rotational states. In this thesis, the rotational states are labelled by letter N. The transition frequencies between rotational

states depends on the angular momenta of the states and the rotational constant B_v which is related to the associated vibrational state. The typical rotational transition frequencies are $\sim$ GHz.

The molecular hyperfine structure is much more complicated than that of atoms. The total angular momentum of a molecule is $\boldsymbol{F} = \boldsymbol{N} + \boldsymbol{I}_{\mathrm{Rb}} + \boldsymbol{I}_{\mathrm{Cs}}$. The ^{87}Rb nucleus and the ^{133}Cs nucleus have a nuclear spin quantum number (I) of 3/2 and 7/2, respectively. The quantum number used to describe the hyperfine states depends on the external magnetic field. At zero field, the total angular $\boldsymbol{F}$ is conserved, hence F is a good quantum number. With an external magnetic field, a rotational manifold spits to $(2N+1)(2I_{\mathrm{Rb}}+1)(2I_{\mathrm{Cs}}+1)$ Zeeman-hyperfine sublevels. For example, there are 32 sublevels for rotational state $N = 0$ and 96 sublevels for $N = 1$. At low magnetic field, F is nearly a good quantum number and the states can be approximately described by F and M_F. M_F is the the projection of F to the quantisation axis, in this case the direction of the magnetic field. At high field, the individual projections M_N, m_I^{Rb} and m_I^{Cs} become nearly good quantum numbers, as the magnetic field decouples the different angular momenta. Hence $M_F = M_N + m_I^{\mathrm{Rb}} + m_I^{\mathrm{Cs}}$ is also nearly a good quantum number. M_F is the only (nearly) good quantum numbers in all regimes. After STIRAP, a magnetic field of 181.6 G is applied to the molecules. In this regime, the only good quantum number is M_F. We use N and M_F to label the states. The absolute ground state of the RbCs molecule at this field is $N = 0$, $M_F = 5$. The state with $N = 0$, $M_F = 5$ is the spin-stretched state. We label the molecular rotational and hyperfine states in the $X^1\Sigma^+$ electronic potential and $v = 0$ vibrational state by $(N, M_F)_k$, where N and M_F were introduced before, k is the index of the Zeeman sublevels with the same N and M_F in order of ascending energy. So $(N = 0, M_F = 5)_0$ has the lowest energy at the given magnetic field.

Using the results in Ref. [49], the polarisabilities for $N = 0, M_N = 0$ (i.e. $N = 0, M_F = 5$) and $N = 1, M_N = 0$ (i.e. $N = 1, M_F = 5$) states are approximated by

$$\alpha_{N=0} = -\frac{3\pi c^2}{2\omega_{v'}^3}\frac{\Gamma_{0,v'}}{3\Delta_{v'}} + \frac{1}{3}\alpha_{\mathrm{bg},\parallel} + \alpha_{\mathrm{bg},\perp}, \tag{3.13}$$

and

$$\begin{aligned}\alpha_{N=1} = &-\frac{3\pi c^2}{2\omega_{v'}^3}\left[\frac{\cos^2(\beta)}{3}\frac{\Gamma_{0,v'}}{\Delta_{v'} + 2B_v + 2B_{v'}} + \frac{3+\cos^2(\beta)}{15}\frac{\Gamma_{0,v'}}{\Delta_{v'} + 2B_v - 4B_{v'}}\right] \\ &+ \frac{2\cos^2(\beta)+1}{5}\alpha_{\mathrm{bg},\parallel} + \frac{4-2\cos^2(\beta)}{5}\alpha_{\mathrm{bg},\perp},\end{aligned} \tag{3.14}$$

respectively. In these equations, α_N is the dynamic polarisability of the rotational state N, c is speed of light, $\omega_{v'}$ is the resonant frequency of the transition from $(v = 0, N = 0)$

state of $X^1\Sigma^+$ potential to $(v', N' = 1)$ state of $b^3\Pi_0$ potential, $\Delta_{v'}$ is the detuning of the laser frequency from the above stated transition. In this chapter, all the laser frequency will be referred to as the detuning from this transition unless otherwise stated. The angle between the laser polarisation direction and the magnetic field direction is β. Note that this angle is different from the angle θ in Eq. (3.9) which is the angle between the molecular axis and the magnetic field. Moreover, this angle is the same as the angle β in Eq. (3.11). B_v and $B_{v'}$ are the rotational constants for the v state of $X^1\Sigma^+$ potential and the v' state of $b^3\Pi_0$ potential, respectively. The parameter $\Gamma_{0,v'}$ is the transition width of the transition specified by v'; it is given by

$$\Gamma_{0,v'} = \frac{\omega_{v'}^3}{3\pi\epsilon_0\hbar c^3}|\mu_{0,v'}|^2, \tag{3.15}$$

where $\mu_{0,v'}$ is the transition dipole moment between the $v = 0$ state of the $\mathrm{X}^1\Sigma^+$ potential and the v' state of the $\mathrm{b}^3\Pi_0$ potential. $\alpha_{\mathrm{bg},\parallel}$ and $\alpha_{\mathrm{bg},\perp}$ are the background polarisabilities in the direction parallel and perpendicular to the molecular axis. In these equations they include the contributions from all the far-detuned vibrational states in the electronic states with $\Omega = 0$ and $\Omega = 1$, respectively [50–52].

The actual polarisability of one state consists of the contributions from the transitions to all vibrational states. The background polarisabilities $\alpha_{\mathrm{bg},\parallel}$ and $\alpha_{\mathrm{bg},\perp}$ account for the contribution from strong transitions to other potentials which are very far detuned from the light. To calculate the contribution from the $b^3\Pi_0$ transitions we must also sum over all possible transitions to various vibrational states. In practice, it's adequate to include the transitions up to $v' = 3$ as the transition width of the transitions to higher vibrational states are small enough and can be neglected. The relevant parameters of Eq. (3.13) and Eq. (3.14) are summarised in Table. 3.1. For some parameters, both the theoretical and the experimentally measured values are given. In all the calculations in this thesis the theoretical values are used unless otherwise stated.

Note that Eq. (3.13) and Eq. (3.14) can only describe the states with $M_N = 0$, therefore, only the π transitions driven by linearly polarised microwave parallel to the magnetic field can be described by these equations. In these transitions $\Delta M_F = 0$. The linearly polarised microwave perpendicular to the magnetic field drives σ^+ and σ^- transitions ($\Delta M_F = \pm 1$ and $M_N \neq 0$), for these transitions the analytical equations are not valid anymore.

We consider the transition $(N = 0, M_F = 5) \rightarrow (1, 5)$ and the associated decoherence mechanism. As described by Eq. (3.9), the molecular polarisability consists of the isotropic term $\alpha^{(0)}$ and the anisotropic term $\alpha^{(2)}$. The contributions of $\alpha^{(2)}$ to the polarisabilities of each rotational state are different, causing a shift in the transition frequency between

Quantity	Value	Reference
$\omega_{v'=0}$	$261533.392 \times 2\pi$ GHz	[49]
	$261571.87(6) \times 2\pi$ GHz	This work
$\omega_{v'=1}$	$263036.075 \times 2\pi$ GHz	Predicted parameters for the transition [49]
	$263065.63(6) \times 2\pi$ GHz	This work
$\omega_{v'=2}$	$264533.289 \times 2\pi$ GHz	Predicted parameters for the transition [49]
	$264555.60(6) \times 2\pi$ GHz	This work
$\omega_{v'=3}$	$266025.212 \times 2\pi$ GHz	Predicted parameters for the transition [49]
$\Gamma_{0,v'=0}$	$15.5 \times 2\pi$ kHz	[49]
	$9.6(1.8) \times 2\pi$ kHz	Paper in progress
$\Gamma_{0,v'=1}$	$6.84 \times 2\pi$ kHz	[49]
	$7.8(1.5) \times 2\pi$ kHz	Paper in progress
$\Gamma_{0,v'=2}$	$1.44 \times 2\pi$ kHz	[49]
$\Gamma_{0,v'=3}$	$0.206 \times 2\pi$ kHz	[49]
B_v	490.155(5) MHz	[53]
	490.173 994(45) MHz	[54]
$B_{v'}$	510 MHz	[49]
$\alpha_{\mathrm{bg},\parallel}$	$0.127 \times h$ kHz/(W/cm^2)	[49]
$\alpha_{\mathrm{bg},\perp}$	$0.0340 \times h$ kHz/(W/cm^2)	[49]

Table 3.1: The summary of the parameters for RbCs molecules up to $v' = 3$. v' is the label of the vibrational states in $b^1\Pi_0$ potential. $\omega_{v'}$ is the transition energy from the $v = 0$ state in $X^1\Sigma^+$ potential to the v' state in $b^1\Pi_0$ potential. The data of transition width $\Gamma_{0,v'}$, rotational constants B_v and $B_{v'}$ and background polarisabilities $\alpha_{\mathrm{bg},\parallel}$ and $\alpha_{\mathrm{bg},\perp}$ are also listed. For those parameters of which two values are given, the first one is quoted and the second one is our experimentally measured value.

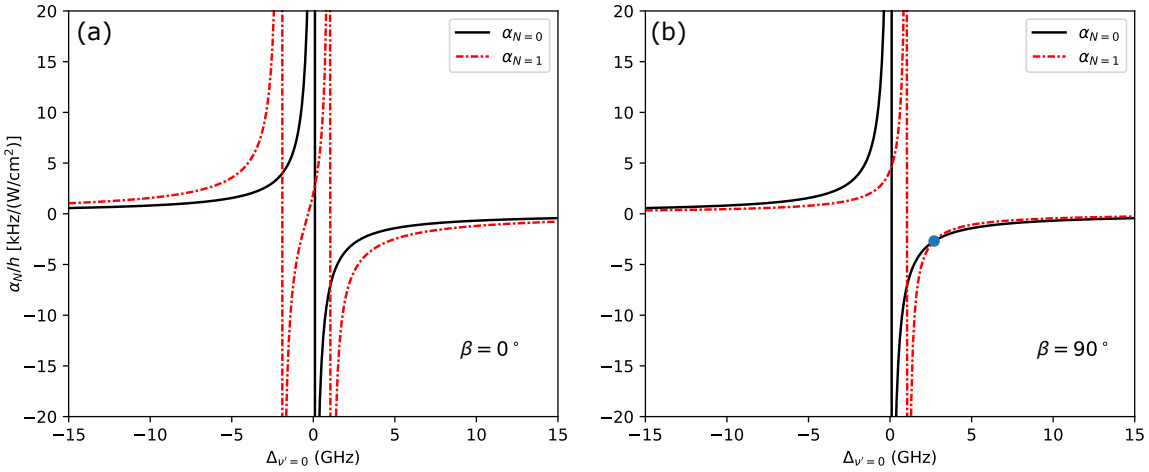

Figure 3.2: Dynamic polarisabilities of N=0 and N=1 states at $\beta = 0°$ (a) and 90° (b) calculated from Eq. (3.13), (3.14) and the method described in the main text. The blue circle in (b) shows the curves of $\alpha_{N=0}$ and $\alpha_{N=1}$ cross at 2.7 GHz.

the rotational transitions. This light shift is the dominant source of decoherence in the processes involving the two states in our previous experiments whenever in an optical trap. The coherence time τ_2 of two states is given by

$$\tau_2 = \frac{1}{|\alpha_{1,s} - \alpha_{2,s}| \times I}, \tag{3.16}$$

where $\alpha_{1,s}$ and $\alpha_{2,s}$ are the total polarisabilities of $N = 0$ and $N = 1$ states by summing over the transitions to all the vibrational states, I is the light intensity. The coherence time can be infinitely lone when the polarisabilities of the two states are equal.

We can eliminate the decoherence by eliminating $\alpha^{(2)}$. For the molecules in their ground electronic state ($X^1\Sigma$), the transitions to the $^1\Sigma$ symmetry electronic states contribute to $\alpha_\parallel$, the transitions to the $^1\Pi$ symmetry electronic states contribute to $\alpha_\perp$. When the laser frequency is close to the electronic transitions between $v = 0$ state in the $X^1\Sigma^+$ potential and the lowest vibrational states in the $b^3\Pi_0$ potential that is weakly mixed with $A^1\Sigma^+$, only $\alpha_\parallel$ can be tuned significantly by the laser. $\alpha_\parallel$ can be tuned as the laser frequency changes and $\alpha_\perp$ doesn't change. This is because that the light is linearly polarised and near the vibrational transitions which are along the internuclear axis. This only affects the polarisability parallel to the axis. As $\alpha_\parallel$ and $\alpha_\perp$ are components of $\alpha^{(2)}$, by tuning the laser detuning from the transition, one can equate $\alpha_\parallel$ and $\alpha_\perp$, then the tensor polarisability term $\alpha^{(2)}$ vanishes. At this detuning the polarisabilities of the two states are equal and there is no light shift.

We calculate the dynamic polarisabilities of $N = 0, M_F = 5$ and $N = 1, M_F = 5$ states as functions of detuning and look for intersections to find a potential magic detuning. The results for the small detunings near the transition from $(v = 0, N = 0)$ state in $X^1\Sigma^+$

potential to $(v' = 0, N' = 1)$ state in $b^3\Pi_0$ potential are shown in Fig. 3.2. A magnetic field with a strength of 181 G is applied to the molecules along the z-axis. The cases of the driving laser polarisation parallel and perpendicular to the magnetic field is shown in (a), (b), respectively. This is an example to show that $\alpha_{N=0}$ is independent of the angle β while $\alpha_{N=1}$ can be tuned by β. At $\beta = 90°$ there is only one pole in $\alpha_{N=1}$ comparing to two poles at $\beta = 0°$. Furthermore, the curves of $\alpha_{N=0}$ and $\alpha_{N=1}$ cross at $\Delta_{v'} = 2\pi \times 2.7$ GHz at $\beta = 90°$ (shown by the blue circle in Fig. 3.2 (b)), which makes it a magic detuning for coupling $N = 0$ and $N = 1$ states. At the magic detuning, $\alpha_{N=0} = \alpha_{N=1} = -h \times 2.71\text{kHz}/(\text{W}/\text{cm}^2)$, so it's possible to trap the molecules in a low-field seeking trap $U = -I\alpha$?. This crossing feature doesn't exist for $\beta = 0°$, which means this magic detuning is still polarisation-dependent and $\alpha^{(2)} \neq 0$. From Eq. (3.11) we see that the polarisability should be independent on the polarisation direction when $\alpha^{(2)} = 0$, therefore, this magic frequency is not good enough to tune $\alpha^{(2)}$ to zero. Below we show that a nearly polarisation-independent magic detuning for $N = 0$ and $N = 1$ states exists in the medium-detuned range.

The Magic Frequency in Medium-detuned Regime

To search for a magic frequency at which $\alpha^{(2)}$ is 0, we calculate the dynamic polarisabilities of $N = 0$ and $N = 1$ rotational states in a wider range of the detuning from the transition from $(v = 0, N = 0)$ state in $X^1\Sigma^+$ electronic state to $(v' = 0, N' = 1)$ state in $b^3\Pi_0$ electronic state at different laser polarisation. The result is shown in Fig. 3.3. The polarisabilities are calculated from -1 THz to more than 5 THz. The polarisabilities of $\alpha_{N=1}$ state at $\beta = 0°$ and $\beta = 90°$ are both shown. The poles in the figure correspond to the resonant transition frequencies to higher vibrational states (v') in $b^3\Pi_0$ potential, which is indicated on the top of the figure. The inset shows the same quantities in a small range of $\Delta_{v'}$ in $214 - 226$ GHz. It can be seen that all the three curves nearly cross the same point in the figure, meaning that the dynamic polarisabilities of the two states are nearly the same at one detuning frequency, and this holds for all the laser polarisation angles. This suggests a magic frequency exists near the resonance transition frequency from $(v = 0, N = 0)$ state in $X^1\Sigma^+$ potential to $(v' = 0, N' = 1)$ state in $b^3\Pi_0$ potential for states $N = 0, M_F = 5$ and $N = 1, M_F = 5$. This magic frequency tunes their dynamic polarisabilities to nearly identical.

The transition frequency shift $\delta\nu$ of the transition from (0, 5) state to (1, 5) state in the ground electronic and vibrational state is given by

$$h\delta\nu = I(\alpha_{1,s} - \alpha_{0,s}), \tag{3.17}$$

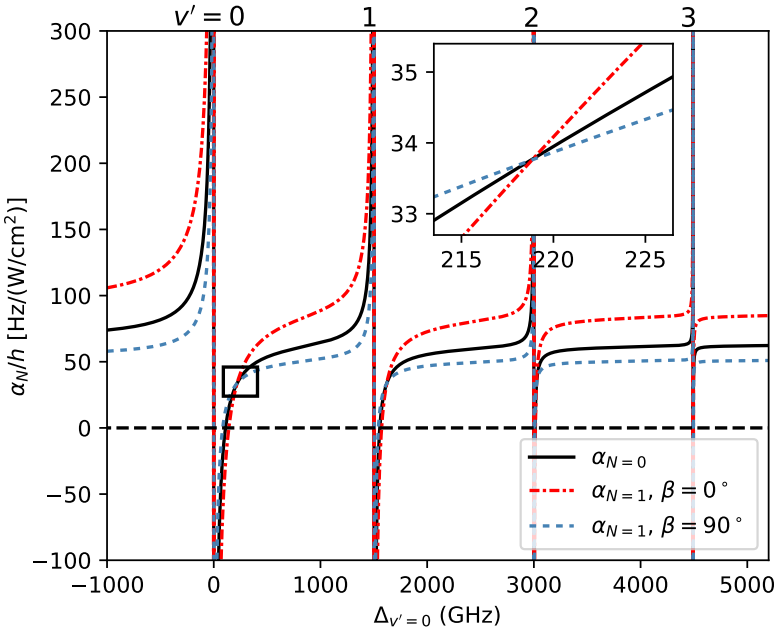

Figure 3.3: Main: The dynamic polarisabilities of $N = 0$ and $N = 1$ rotational states in the ground electronic and vibrational state at the detuning more than 5 THz. $\alpha_{N=0}$ (black line) is independent of the laser polarisation. For $\alpha_{N=1}$, The polarisabilities for laser polarisation parallel (red line) and perpendicular (blue line) to the magnetic field are calculated. The poles in the curves correspond to the resonant transition frequencies to higher vibrational states. The x-axis is given in frequency. Inset: A zoom-in to the detuning around 220 GHz (indicated by the box in the main). The three curves nearly cross the same point.

where h is the Planck constant, I is the light intensity, $\alpha_{0,s}$ and $\alpha_{1,s}$ are the total polarisabilities of $N = 0$ and $N = 1$ states calculated by summing over the transitions to different v' states as described before, respectively. The light shift is proportional to the difference in the polarisabilities. The results of the polarisability difference are given in Fig. 3.4. The difference of α_1 and α_0 for the laser polarisation parallel to the magnetic field ($\beta = 0°$) and perpendicular to the magnetic field ($\beta = 90°$) are calculated. The poles in the figure correspond to transitions to different vibrational states. In the x-axis range of this figure the poles for transitions to different rotational states cannot be resolved. Once the light intensity is known, the light shift can be calculated. It can be seen that at the magic detuning, the differences in polarisabilities of both polarisations are zero, indicating a polarisation-independent magic trap.

Experimentally we can measure the difference of the polarisabilities of the molecules by measuring the light shift of the transition frequency of $(N = 0, M_F = 5) \rightarrow (1, 5)$ of the ground electronic and vibrational state. We measure the transition frequencies with

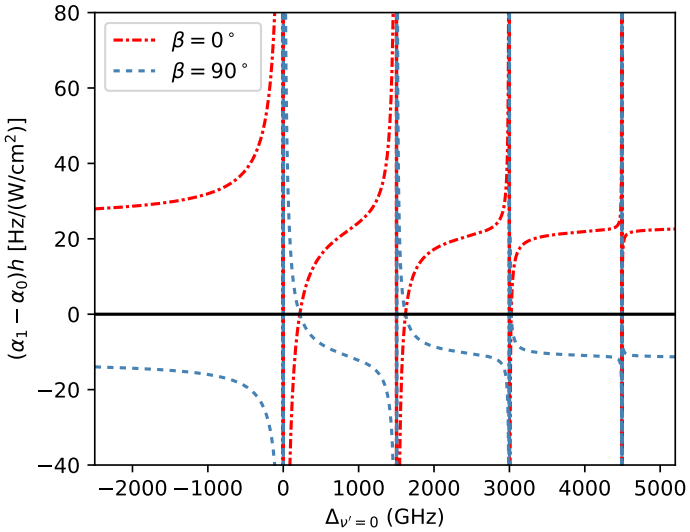

Figure 3.4: The difference of α_1 and α_0 over a detuning range from -3000 GHz to 5000 GHz caused by the AC stark shift of the trapping light. The difference is calculated using the equations for the analytical dynamic polarisabilities at $\beta = 0°$ (orange line) and $\beta = 90°$ (blue line). The difference in the polarisability leads to the light shift of the transition $(N = 0, M_N = 5) \rightarrow (1, 5)$. At the magic detuning, the difference in α_0 and α_1 of both polarisations vanishes, making light shifts go down to 0.

and without the presence of the light by microwave spectroscopy. The light shift can be inferred by comparing the transition frequencies with the light on to that in the free space. The details of the experiment will be given in Section 3.3.

Predicted Coherence Time at The Magic Frequency

We are interested in the coherence time at the magic frequency when we couple $N = 0$ and $N = 1$ states. The purpose of the magic trap is to eliminate differential AC Stark shift between the states we want to couple together and hence create a long coherence time in a system involving these states. The coherence time τ_2 of two states is given by Eq. (3.16).

We calculate the expected coherence time at the frequencies around the magic frequency for different a light intensity of 600 W/cm^2 as shown in Fig. 3.5. This light intensity corresponds to $\sim$1 μK trap depth for the polarisability at the magic frequency. Experimentally the light intensity at the molecules can be readily changed in different ways; we use a single pass AOM before the fibre to control the light power coupled to the fibre, or we can use different lenses in the setup to vary the beam waist at the position of molecules. In Fig. 3.5, the frequencies are relative to $\nu_{\text{magic}} = 218900$ MHz which is the magic detuning frequency at $\beta = 0°$. The results are given in a relative large fre-

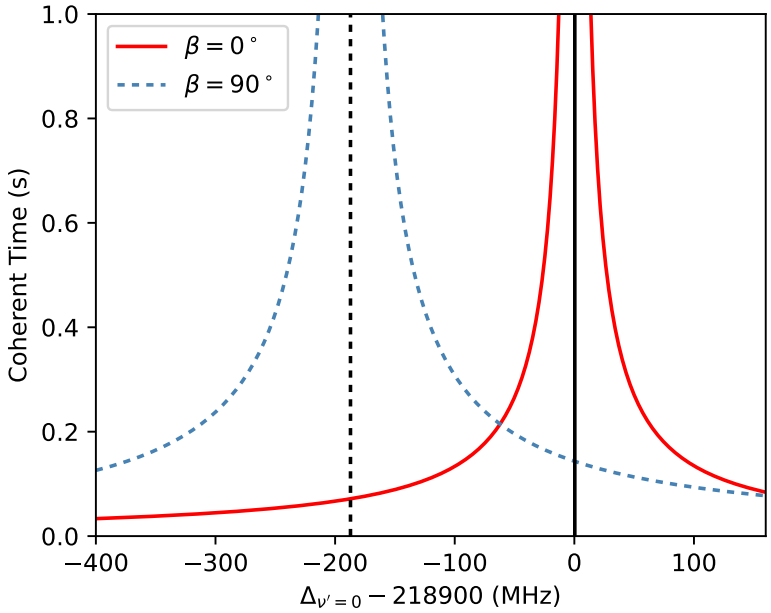

Figure 3.5: The expected coherence time at different polarisation angles. The frequencies are relative to $\nu_{\text{magic}} = 218900$ MHz which is the magic detuning frequency for polarisation being parallel to the magnetic filed. An intensity of 600 W/cm^2 is used in the calculation. This intensity corresponds to $\sim$1 μK trap depth for the polarisability at the magic frequency. The solid line shows the expected coherence time for $\beta = 0°$; the dashed line shows the expected coherence time for $\beta = 90°$.

quency range, but the coherence time is still long at hundreds of megahertz away from the magic frequency. The laser frequency can be stabilised such that the linewidth is within 20 MHz ensuring a long coherence time.. The coherence time curves of the parallel polarisation and the perpendicular polarisation don't overlap well with each other in this range indicating there's still a small angle dependence of the magic detuning.

3.2.2 Extend the Magic Condition to Higher Excited Rotational States

In the previous section, we have shown that there is a magic frequency near the transition from $v = 0$, $N = 0$ state in $X^1\Sigma^+$ potential to $v' = 0$, $N' = 1$ state in $b^3\Pi_0$ potential in the medium-detuned regime. In this section we will show that this frequency is also near-magic for higher rotationally excited states in the ground electronic and vibrational state.

Theoretical Basis of the Magic Frequency for Multiple Rotational States

We employ the same method as the last section to search for the magic frequency for multiple rotational states, i.e., looking for the crossing in the dynamic polarisability curves. The general formula of the dynamic polarisability of the rotational states in the ground electronic and vibrational state illuminated by the light whose frequency is near the transitions to the states in $b^2\Pi_0$ potential is given by [49]

$$\begin{aligned}\alpha_N = &-\frac{3\pi c^2}{2\omega_{v'}^3}\left[A_N(\beta)\frac{\Gamma_{0,v'}}{\Delta_{v'}+L_N}+B_N(\beta)\frac{\Gamma_{0,v'}}{\Delta_{v'}+R_N}\right]\\ &+\left[A_N(\beta)+B_N(\beta)\right]\alpha_{bg,\parallel}+\left[1-A_N(\beta)-B_N(\beta)\right]\alpha_{bg,\perp},\end{aligned} \tag{3.18}$$

where L_N and R_N gives the pole positions of the left and the right branch, respectively, and $A_N(\beta)$ and $B_N(\beta)$ are the angular factors, and all the other parameters were defined before. The pole positions are

$$L_N = N(N+1)B_v - [N(N-1)-2]B_{v'}, \tag{3.19}$$

and

$$R_N = N(N+1)B_v - [(N+1)(N+2)-2]B_{v'}, \tag{3.20}$$

where B_v and $B_{v'}$ are the rotation constants for the states in $X^1\Sigma^+$ potential and $b^3\Pi_0$ potential, respectively as stated before. The angular factors $A_N(\beta)$ and $B_N(\beta)$ are

$$A_N(\beta) = \begin{cases} \frac{(N+1)(N-1)}{2(2N+1)(2N-1)} & \\ +\frac{N^2+1}{2(2N+1)(2N-1)}\cos^2\beta, & N>0 \\ 0, & N=0, \end{cases} \tag{3.21}$$

and

$$B_N = \frac{(N+2)(N+1)}{2(2N+3)(2N+1)} + \frac{N(N+1)}{2(2N+3)(2N+1)}\cos^2\beta, \tag{3.22}$$

where β is the angle between the linearly polarised laser and the uniform magnetic field.

In Section 3.2.1 we have stated that the transitions from the $(v=0, N=0)$ state of the $X^1\Sigma^+$ potential to all the far-detuned vibrational states of the $b^3\Pi^0$ potential contribute to the total dynamic polarisability. Below we will give the formula of the dynamic polarisability including the contribution of all the vibrational states. For this purpose, one needs to sum the dynamic polarisability over all the vibrational states which are specified by their transition frequencies $\omega_{v'}$, transition widths $\Gamma_{0,v'}$ and corresponding laser detuning $\Delta_{v'}$. Practically one only needs to consider the vibrational states from $v'=0$ up to $v'=3$, as for higher states the transition widths are too small and can be neglected (the transition widths are listed in Table 3.1). Therefore, the dynamic

polarisability near the transition from the rotational state $N = 0$ of the $X^1\Sigma^+$ potential to the rotational trapping state of the quantum number N of the $b^3\Pi^0$ potential can be approximated by

$$\begin{aligned}\alpha_N = &\sum_{v'=0}^{3} -\frac{3\pi c^2}{2\omega_{v'}^3}\left[A_N(\beta)\frac{\Gamma_{0,v'}}{\Delta_{v'}+L_N} + B_N(\beta)\frac{\Gamma_{0,v'}}{\Delta_{v'}+R_N}\right] \\ &+ \left[A_N(\beta)+B_N(\beta)\right]\alpha_{\mathrm{bg},\parallel} + \left[1-A_N(\beta)-B_N(\beta)\right]\alpha_{\mathrm{bg},\perp}.\end{aligned} \tag{3.23}$$

The background polarisability terms are not summed as $\alpha_{\mathrm{bg},\parallel}$ ($\alpha_{\mathrm{bg},\perp}$) already include the contribution from the transitions to all the vibrational states in the electronic states with $\Omega = 0$ ($\Omega = 1$). In Eq. (3.23), the detuning $\Delta_{v'}$ are relative the the transition frequency to the corresponding vibrational state in the $b^3\Pi_0$ potential specified by v', i.e. $\omega_{v'}$ which can be found in Table. 3.1. Note that for a certain laser frequency, $\Delta_{v'}$ is different for the different target vibrational states v', but once the detuning relative to $v' = 0$ state is set, the detuning relative to the other vibrational states will also be set and can be calculated by subtracting the energy difference between the corresponding vibrational states.

Now we rewrite the equation for the polarisability by making an approximation. Previously we have seen that the magic detuning frequency for $N = 0$ state and $N = 1$ state at $\beta = 0°$ is 218.900 GHz. We consider the situation where we set the detuning to or near the magic detuning.. As L_N and R_N have the same magnitude as B_v and $B_{v'}$ which are less than 1 GHz, the magnitude of the detuning is much larger than that of L_N and R_N, i.e. $|\Delta_{v'}| \gg |L_N|$ and $|\Delta_{v'}| \gg |R_N|$, and one can Taylor-expand Eq. (3.23) around $\frac{L_N}{\Delta_{v'}} = 0$ and $\frac{R_N}{\Delta_{v'}} = 0$. Then it can be derived that

$$\alpha_N = \left[A_N(\beta)+B_N(\beta)\right]\left[\sum_{v'=0}^{3}\left(-\frac{3\pi c^2}{2\omega_{v'}^3}\frac{\Gamma_{0,v'}}{\Delta_{v'}}\right) + \alpha_{bg,\parallel} - \alpha_{bg,\perp}\right] + \alpha_{bg,\perp} + T_N(\Delta_{v'},\beta), \tag{3.24}$$

where $T_N(\Delta_{v'},\beta)$ is the remaining term and reads

$$\begin{aligned}T_N(\Delta_{v'},\beta) = &\left[A_N(\beta)L_N + B_N(\beta)R_N\right]\sum_{v'=0}^{3}\left(\frac{3\pi c^2}{2\omega_{v'}^3}\frac{\Gamma_{0,v'}}{\Delta_{v'}^2}\right) \\ &+ O\left(\frac{\Gamma_{0,v'}L_N^2}{\Delta_{v'}^3}\right) + O\left(\frac{\Gamma_{0,v'}R_N^2}{\Delta_{v'}^3}\right).\end{aligned} \tag{3.25}$$

We will analyse this term in detail later. According to Eq. (3.24), one can always find the detuning $\Delta_{v',\mathrm{cr}}$ such that

$$\sum_{v'=0}^{3}\left(-\frac{3\pi c^2}{2\omega_{v'}^3}\frac{\Gamma_{0,v'}}{\Delta_{v',\mathrm{cr}}}\right) + \alpha_{\mathrm{bg},\parallel} - \alpha_{\mathrm{bg},\perp} = 0 \tag{3.26}$$

is satisfied by $\Delta_{v',\mathrm{cr}}$. Then the first term of Eq. (3.24) vanishes and the dynamic polarisability becomes

$$\alpha_N = \alpha_{\mathrm{bg},\perp} + T_N(\Delta_{v',\mathrm{cr}},\beta). \tag{3.27}$$

N	0	1	2	3	4	5	6
α_N/h [Hz/(W/cm^2)]	34.00	34.17	34.10	34.06	34.01	33.95	33.88
Difference from α_N (%)	0	0.5	0.3	0.2	0.03	-0.1	-0.4

Table 3.2: The values of the dynamic polarisabilities of different states at $\Delta_{v'} = 220.32$ GHz.

In the medium-detuned regime, we have $|\Delta_{v'}| \gg |\Gamma_{0,v'}|$, and the remaining term $T_N(\Delta_{v',\mathrm{cr}}, \beta)$ can be neglected. From Eq. (3.27) it can be seen that in this case, both the β-dependence and the N-dependence of α_N is eliminated, and for all the rotational states, the frequency-dependent dynamic polarisabilities are tuned to the same by the trapping light at this detuning; therefore, the trap is magic for all rotational states at this laser detuning frequency. This detuning can eliminate the energy shift between the different rotational states and hence remove the source of decoherence. We describe this laser frequency as the "magic frequency" or "magic detuning". The value of the magic detuning is approximately calculated by solving Eq. (3.26) and the dynamic polarisability is approximately equal to $\alpha_{\mathrm{bg},\perp}$. Solving Eq. (3.26) numerically gives $\Delta_{v',\mathrm{cr}} = 220.32$ GHz. The corresponding laser frequency and wave length is 261.75371 THz and 1145.35 nm. The values of the dynamic polarisabilities of a series of states are given in Table. 3.2.

The Dynamic Polarisabilities Near the Magic Frequency

To have a better idea of the magic frequency, we look at the dynamic polarisabilities of a series of rotational states as functions of the the laser detuning. We are particularly interested in the values of the dynamic polarisabilities around the theoretical magic detuning frequency. Figure 3.6 shows the α_N curves with $N = 0$ to 6 around the magic detuning near the resonance transition to the $v' = 0$ vibrational state in the $b^3\Pi_0$ potential. The dynamic polarisabilities are calculated by Eq. (3.23). Figure 3.6 (b) shows the zoom-in figure into the detuning close to the magic detuning frequency. For $N = 0, 1, 2$, the curves of α_N cross each other in the detuning window of 218 GHz to 219.5 GHz. This forms a near triple magic frequency window.

The precise crossing points of the curves of α_0 and α_1, α_1 and α_2, α_0 and α_2 are at 218.90 GHz, 218.15 GHz, 219.20 GHz, respectively. These values are different from that calculated from Eq. (3.26) despite of the small differences. The difference is due to the higher-order corrections in the remaining term $T_N(\Delta_{v'}, \beta)$. The values of α_N at the near-magic window are consistent with the value of $\alpha_{\mathrm{bg},\perp}$ as predicted by Eq. (3.27).

For the physics processes that involve three rotational levels, even though the three

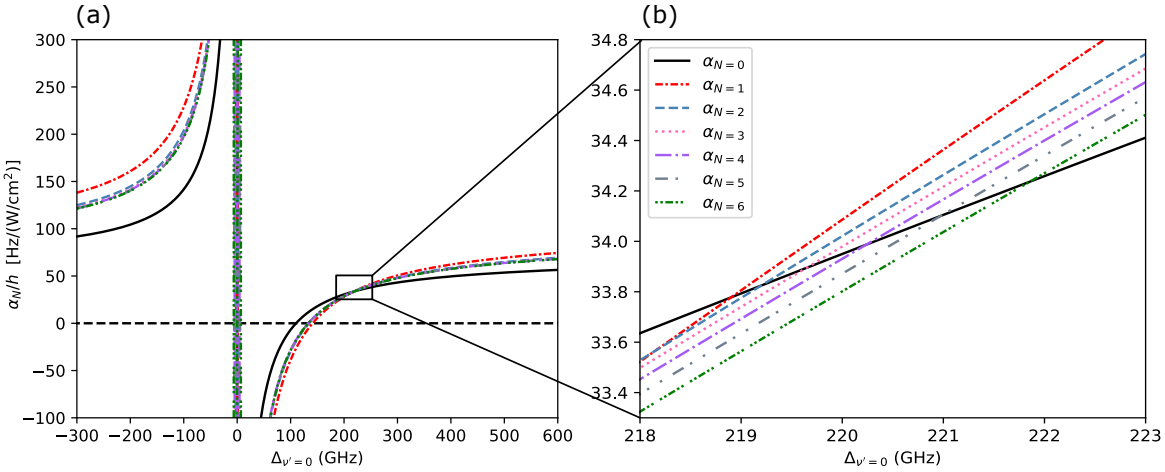

Figure 3.6: The dynamic polarisabilities of the rotational states from N = 0 to 6 near the resonance transition to the $v' = 0$ state of the $b^3\Pi_0$ potential. A magnetic field of 181 G is applied alone the z-axis. The laser polarisation is parallel to the magnetic field, i.e. $\beta = 0°$. No electric field is applied. (a) shows the dynamic polarisabilities in a wider detuning range. The dashed line indicates the position of 0. (b) shows a zoom-in near the magic detuning. A near triple magic condition exist for N=0, 1, 2.

curves do not intersect each other at the same frequency, their values are very close in the frequency window of 1.5 GHz wide (from 218 GHz to 219.5 GHz) as shown in Fig. 3.6 (b). The percent difference $|\alpha_N - \alpha_{N'}|/|\alpha_{N'}|$ for any pair of N and N' with N and N' being 0, 1, 2 in this window is less than 0.3%. This near triple magic frequency window can be further tuned to a true triple magic frequency by adding a weak static electric field [49], but this outside the scope of this thesis.

To further evaluate the validity of the approximation adopted by Eq. (3.24), we can calculate the remaining term $T_N(\Delta_{v'}, \beta)$ given by Eq. (3.25) and compare it to the α_N values in Fig. 3.6 to find the effect of the $T_N(\Delta_{v'}, \beta)$ term. As Eq. (3.24) is obtained by a Taylor expansion, the remaining term is an infinite series of polynomials with each term being a higher order infinitesimal as the previous one. The first four terms of $T_N(\Delta_{v'}, \beta)$

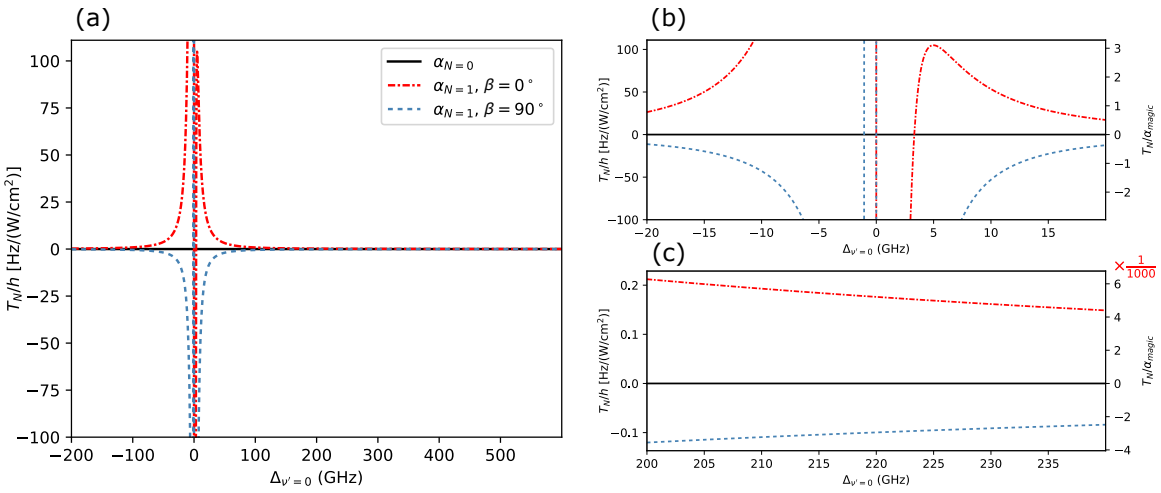

Figure 3.7: Evaluation of $T_N(\Delta_{v'}, \beta)$. (a) Shows the $T_N(\Delta_{v'}, \beta)$ curves of the dynamic polarisabilities of $N = 0,\ 1$ rotational states near the resonance transition to the $v' = 0$ state of the $b^3\Pi_0$ potential. (b) and (c) show the zoom-in curves for small detunings and large detunings around the magic detuning, respectively. The right axes of (b) and (c) also show $T_N/\alpha_{\text{magic}}$ where α_{magic} is the dynamic polarisability at the magic frequency. Note the 1/1000 factor of the right axis in (c). The remaining term is large at small detuning but small for large detunings. At magic detuning it's very small comparing to the polarisability value.

are

$$
\begin{aligned}
T_N(\Delta_{v'}, \beta) = {} & (A_N(\beta)L_N + B_N(\beta)R_N) \sum_{v'=0}^{3} \left(\frac{3\pi c^2}{2\omega_{v'}^3} \frac{\Gamma_{0,v'}}{\Delta_{v'}^2} \right) \\
& - (A_N(\beta)L_N^2 + B_N(\beta)R_N^2) \sum_{v'=0}^{3} \left(\frac{3\pi c^2}{2\omega_{v'}^3} \frac{\Gamma_{0,v'}}{\Delta_{v'}^3} \right) \\
& + (A_N(\beta)L_N^3 + B_N(\beta)R_N^3) \sum_{v'=0}^{3} \left(\frac{3\pi c^2}{2\omega_{v'}^3} \frac{\Gamma_{0,v'}}{\Delta_{v'}^4} \right) \\
& - (A_N(\beta)L_N^4 + B_N(\beta)R_N^4) \sum_{v'=0}^{3} \left(\frac{3\pi c^2}{2\omega_{v'}^3} \frac{\Gamma_{0,v'}}{\Delta_{v'}^5} \right) \\
& + O\left(\frac{\Gamma_{0,v'} L_N^6}{\Delta_{v'}^7} \right) + O\left(\frac{\Gamma_{0,v'} R_N^6}{\Delta_{v'}^7} \right),
\end{aligned}
\tag{3.28}
$$

where all the variables were defined before. We can go further and write the complete form of $T_N(\Delta_{v'}, \beta)$ as the sum of the infinite series:

$$
T_N(\Delta_{v'}, \beta) = \sum_{x=1}^{\infty} (-1)^{x+1} \left[[A_N(\beta)L_N^x + B_N(\beta)R_N^x] \sum_{v'=0}^{3} \left(\frac{3\pi c^2}{2\omega_{v'}^3} \frac{\Gamma_{0,v'}}{\Delta_{v'}^{x+1}} \right) \right], \tag{3.29}
$$

where x is the power of the polynomials. The dependence of $T_N(\Delta_{v'}, \beta)$ on the angle β is hidden in $A_N(\beta)$ and $B_N(\beta)$. This is an alternating series and it converges. Figure 3.7

shows the results of the calculation of the remaining term $T_N(\Delta_{v'}, \beta)$ based on Eq. (3.29). The conditions in this figure is the same as the conditions used in Fig. 3.6, i.e. the magnetic field is 181 G and alone the z-axis and the electric field is 0. The angle between the light polarisation and the magnetic field at both $\beta = 0°$ and $\beta = 90°$ are shown. Figure 3.7 (a) shows the curves of $T_N(\Delta_{v'}, \beta)$ with $N = 0, 1$ as functions of the detuning $\Delta_{v'=0}$ in the range the same as Fig. 3.6 (a). Figure 3.7 (b) shows the remaining term at the small detunings; Fig. 3.7 (c) shows that at large detunings near the magic detuning. In Fig. 3.7 (b) and (c), the ratio between $T_N(\Delta_{v'}, \beta)$ and α_{magic}, $T_N/\alpha_{\text{magic}}$, is also shown on the right hand side y-axes of the plots.

Since we have $A_N(\beta) = 0$ and $R_N = 0$ for $N = 0$, the value of $T_N(\Delta_{v'}, \beta)$ is 0 at all the detuning values for $N = 0$, which is shown by the black line in the Fig. 3.7. Hence for $N = 0$ α_N can be strictly expressed by Eq. (3.24) excluding the $T_N(\Delta_{v'}, \beta)$ term. But for the other α_N with $N \neq 0$ this is not the case. The absolute values of $T_N(\Delta_{v'}, 0)$ are large at small $\Delta_{v'=0}$, but decrease rapidly when Δ_0 increases. It can be seen from the right hand side axis of Fig. 3.7 (c) that at magic detuning, the remaining terms are much less than the dynamic polarisability, with the $T_N(\Delta_{v'}, 0)$ at all the $\Delta_{v'=0}$ values being within 0.5% of α_N. This is consistent with the results shown in Fig. 3.6. Note that Fig. 3.7 is calculated by Eq. (3.29), but a cutoff number was adopted as an infinite number of terms cannot be processed by the computer. In this calculation, a cutoff number of 20 was used.

From Fig. 3.6 one can see that a near-magic window exists for $N = 0$, 1 and 2, but the dynamic polarisability curves for $N = 3$ and higher are almost parallel to that of $N = 2$ in the medium-detuned regime and don't intersect with the curves of the lower rotational states. This can be explained by the behaviour of the angular factors $A_N(\beta)$ and $B_N(\beta)$ in Eq. (3.21) and Eq. (3.22) at large N values. For $N \gg 1$, $1/N \ll 1$, then Eq. (3.21) and Eq. (3.22) can be expanded in terms of $1/N$ and become [49]

$$A_N(\beta) = \frac{1 + \cos^2(\beta)}{8} + O\left(\frac{1}{N^2}\right), \tag{3.30}$$

and

$$B_N(\beta) = \frac{1 + \cos^2(\beta)}{8} + \frac{\sin^2(\beta)}{8N} + O\left(\frac{1}{N^2}\right). \tag{3.31}$$

From the expansion we know that when N increases, both Eq. (3.30) and Eq. (3.31) become independent of N. In Eq. (3.23), $[A_N(\beta) + B_N(\beta)]$ is the coefficient of the $\Delta_{v'}$ term, which means for large N values, the slope of the α_N curves in the medium-detuned regime become similar and the curves are asymptotic if we neglect the remaining term $T_N(\Delta_{v'}, \beta)$. Hence the α_N curves are not expected to cross each other but still close and become almost parallel to each other for high N values. Considering the near-magic

window for $N = 0$, 1, 2 and the asymptotic behaviour of the higher N values, a near-magic frequency to trap the molecules which tunes the dynamic polarisabilities of different rotational states very close to each other should be possible in experiment.

From the results and the discussions above, we can conclude that a magic frequency window of a few gigahertz wide exists for multiple rotational states of the ground electronic and vibrational state. In this frequency window the dynamic polarisabilities of each state are very close to each other offering significantly long coherence time for the RbCs molecules going through multiple rotational transitions.

3.2.3 Polarisation Dependence of the Magic Frequency

According to Eq. (3.27), the dynamic polarisabilities of all the rotational levels are the same at the magic detuning whose value is given by Eq. (3.26) if the remaining term $T_N(\Delta_{v'}, \beta)$ can be neglected. This makes the magic frequency independent of the polarisation. However, if we take the $T_N(\Delta_{v'}, \beta)$ term into consideration, there is a weak dependence of the dynamic polarisabilities on the polarisation directions. In this section we will address the effect of this factor.

Since the dynamic polarisabilities are affected by the angle between the laser polarisation direction and the magnetic field direction (denoted by β), the magic frequency is also affected by this angle. To investigate the effect of β on the magic frequency, we take a closer look at the analytical equation of the dynamic polarisabilities. The difference between the dynamic polarisabilities of two rotational states N_1 and N_2 is given by

$$\begin{aligned}\alpha_{N_1} - \alpha_{N_2} = [A_{N_1}(\beta) + B_{N_1}(\beta) - A_{N_2}(\beta) - B_{N_2}(\beta)] \left[\sum_{v'=0}^{3} \left(-\frac{3\pi c^2}{2\omega_{v'}^3} \frac{\Gamma_{0,v'}}{\Delta_{v'}}\right) + \alpha_{bg,\parallel} - \alpha_{bg,\perp}\right] \\ + [T_{N_1}(\Delta_{v'}, \beta) - T_{N_2}(\Delta_{v'}, \beta)],\end{aligned} \tag{3.32}$$

where all the variables were defined before. The magic detuning can be found by setting Eq. (3.32) to zero. If we neglect the $T_N(\Delta_{v'}, \beta)$ terms, this can be done by setting the terms in either the first or the second bracket to zero. We call the terms in the first bracket the angular term and the terms in the second bracket the frequency term. The magic detuning given by Eq. (3.26) tunes the frequency term to zero. Then the dependence of $\alpha_{N_1} - \alpha_{N_2}$ on β only comes from the $T_N(\Delta_{v'}, \beta)$ terms, which is a weak dependence. The reason why the calculated magic detuning deviates from the value predicted by Eq. (3.26) is that the term in the first and the second bracket as a whole must compensate for the $T_N(\Delta_{v'}, \beta)$ terms which are small. However, when we set the term in the first bracket to zero, the $T_N(\Delta_{v'}, \beta)$ terms actually cannot compensated for so the two-state true magic

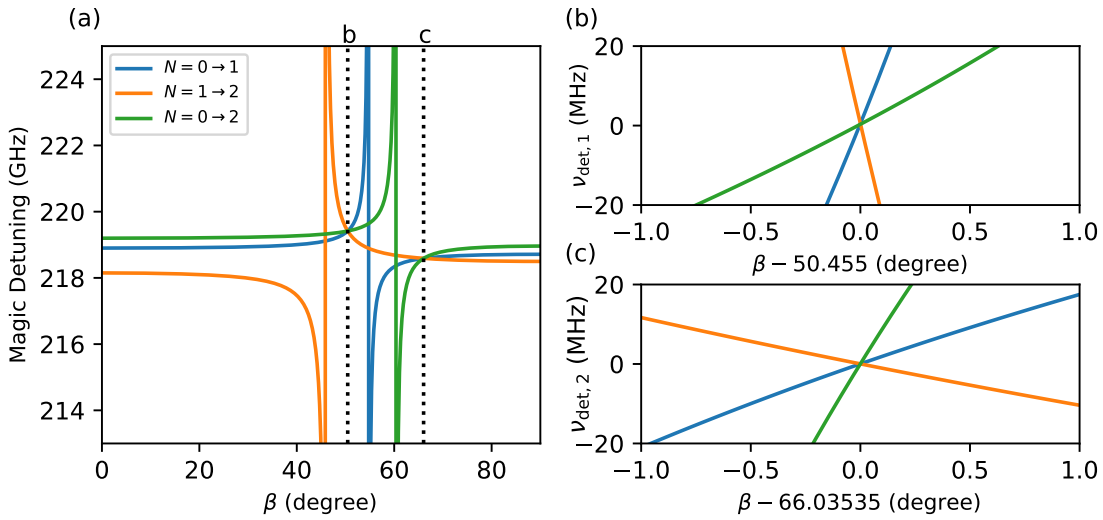

Figure 3.8: Polarisation dependence of the magic detuning for any two of $N = 0$, 1, 2 states. The magic detuning is the detuning at which the dynamic polarisability curves of the two states cross. The blue line shows the magic detunings as a function as the angle β between the laser polarisation direction and the magnetic field direction for $N = 0$ to $N = 1$ states. The orange line shows that for $N = 1$ to $N = 2$ states, green for $N = 0$ to $N = 2$ states. All the states have $M_N = 0$. (a) Shows the three curves cross at two points, meaning the three states have nearly the same magic frequencies at certain laser polarisation. (b) and (c) show the zoom in to the crossings of the magic detuning curves. Their positions in (a) are indicated by dotted lines. The y axis of (b) $\nu_{\mathrm{det},1}$ = magic detuning -219414 MHz. The y axis of (c) $\nu_{\mathrm{det},2}$ = magic detuning -218590.1 MHz.

detuning disappears.

we can calculate the magic frequency at different angles by searching for the crossings of the polarisability curves of two rotational states involved in a physical process. The magic detunings for three states of $N = 0$, 1, 2 as functions of β are shown in Fig. 3.8. The blue line shows the magic detunings for states $N = 0$ and $N = 1$. The orange and green lines show those for $N = 1$, 2 and $N = 0$, 2 states. Take the blue line as an example, the position of the pole is at the angle β that sets the angular term to zero, then the magic detuning diverges. Around this angle the angular term is not zero but relatively small, then the detuning needs to deviate more to compensate for the $T_N(\Delta_{v'}, \beta)$ terms. In this angle regime the magic detuning has an increased polarisation dependence. In the regime β being far from the pole, the polarisation dependence is nearly eliminated. This is the same case for the other curves, too.

From Fig. 3.8 (a) we can see that at $\beta = 0°$ the magic frequencies for the three states are very close, but there is a difference of $\sim$1.5 GHz. This is the same as what we

see in Fig. 3.6. By considering the angular dependence of the magic detunings, we can tune the magic detunings by working at certain polarisation direction. On Fig. 3.8, the three curves cross at two points, meaning the three states have nearly the same magic frequencies at those laser polarisation. The zoom in plots of the magic detunings at these β are shown in Fig. 3.8 (b) and (c) show the zoom in plot around the crossings near 50.455° and 66.03535°, respectively. The y axes of Fig. 3.8 (b) and (c) are detuning from the the value where the three curves cross. In (b) the y axis $\nu_{\mathrm{det},1}$ equals magic detuning minus 219414 MHz. The y axis $\nu_{\mathrm{det},2}$ of (c) is magic detuning minus 218590.1 MHz.

3.3 Experimental Results

3.3.1 Introduction of the Experiment

In our experiment, we produce the ultracold ^{87}Rb^{133}Cs molecules by magnetoassociate the pre-cooled ^{87}Rb and ^{133}Cs atoms using Feshbach association [55]. Then the molecules are transferred to the electronic and rovibrational ground state using Stimulated Raman Adiabatic Passage (STIRAP) technique [16].

The STIRAP transfers the molecules to the state with $N = 0$ and $M_F = 5$, the absolute ground state at the magnetic field of 181.6 G applied to molecules. Using the state labelling method described in 3.2.1, the ground state at this field is labelled as $(N = 0, M_F = 5)_0$. The details of this process were described in Chapter 2[1]. In our experiment, the apparatus is able to produce up to 4000 ground state molecules in one experiment cycle. For imaging the molecules, they are brought back to the free atomic states by inverting the STIRAP process and tuning the magnetic field back across the relevant interspecies Feshbach resonance. The results atoms are then imaged by absorption imaging. This means only the population in the absolute ground state is imaged, giving us a state-selective imaging method.

The 1146 nm light is generated by a homebuilt external cavity diode laser (ECDL) that produces up to 20 mW light power at the molecules. Depending on the intensity required, the beam waist can be varied from 20 μm to 440 μm. We can also vary the power of the light by using a combination of $\lambda/2$ waveplate and the polarisation beam splitter (PBS) cube and varying the waveplate axis direction. When needed, we stabilise the laser frequency with reference to the 977 nm STIRAP laser using a scanning transfer

[1]The experimental apparatus for STIRAP described in Chapter 2 in this thesis is in the optical tweezer lab which is similar but not identical to the optical system for STIRAP in the lab in which the magic trap experiments were conducted. For a description of the STIRAP apparatus in this lab, see Ref. [24].

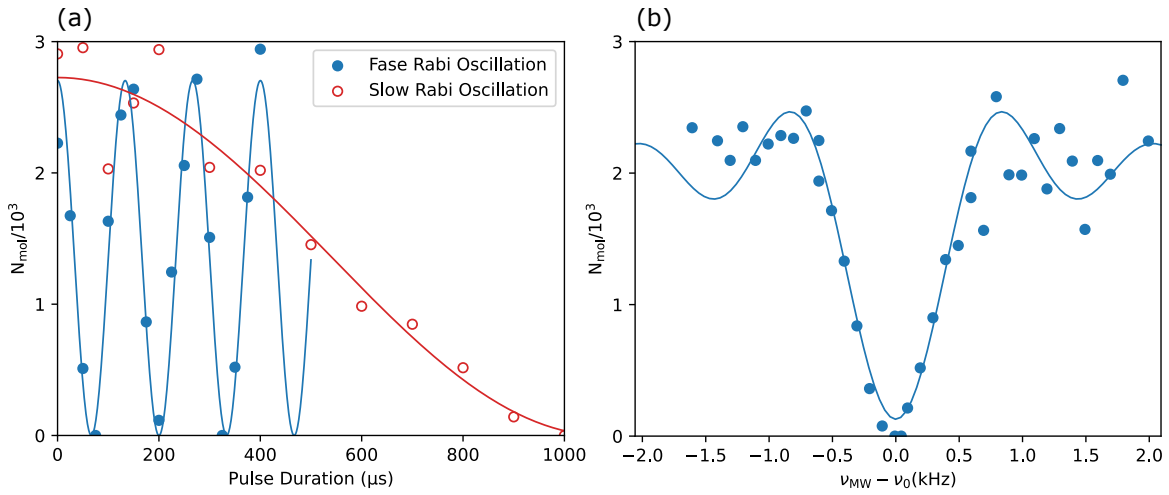

Figure 3.9: (a): The Rabi oscillations to determine the microwave pulse duration for a π-pulse. The blue and red lines are the fittings of the data. (b) An example of the microwave spectroscopy for the transition from $(N = 0, M_F = 5)_0$ to $(N = 1, M_F = 6)_0$. The molecules in $N = 0$ state is imaged.

cavity lock [56]. The estimated upper limit of the locked laser linewidth is ∼20 MHz from the narrowest features we observed. The frequency of this laser is tuned by changing the angle of the grating in the laser. The frequency is measured by Bristol Instruments 621A laser wavelength meter whose operating range is 520-1700 nm and precision 70 MHz.

3.3.2 Spectroscopy of $N = 0 \rightarrow 1$ Transitions

We measure the transition frequencies from the ground vibrational state in $X^1\Sigma^+$ potential to the vibrational states in $b^3\Pi_0$ potential. We shine the 1146 nm laser light on the ground state molecules for 1 ms with a peak intensity of $7(1) \times 10^{-4}$ W/cm^2. We tune the laser frequency close to the transition frequencies and measure the number of the molecules in the ground state. The only allowed transitions are to the rotational states of $N' = 1$ in each v' states. A loss of the molecules is expected when the laser is on resonance with an allowed transition. Thus we can find the centre frequency. We measured the transition frequencies to the vibrational states with v'=0, 1, 2 in $b^3\Pi_0$ potential. The results are listed in Table. 3.1 as $\omega_{v'}$ and the references are labelled as "this work". The transition frequency $\omega_{v'=0}$ is 261571.87(6) $\times 2\pi$ GHz. The error of this measurement is limited by the accuracy of the wavelength meter which is 20 MHz. Note that although we have the precise experimentally measured transition frequency values, in this thesis we still give all the laser detunings relative to the theoretical value of $\omega_{v'=0} = 261533.392 \times 2\pi$ GHz unless otherwise stated. The theoretical value of $\omega_{v'=0}$ is shown in the first row of Table. 3.1.

We then measure the differential light shift between $N = 0$ and $N = 1$ rotational states. We excite the molecules from $(N = 0, M_F = 5)_0$ state to $(N = 1, M_F = 6)_0$ state by the unpolarised microwave with the molecules being illuminated by the 1146 nm laser. We measure the transition frequency between the two rotational states and compare it to the transition frequency in the free space to derive the light shift induced by the 1146 nm light.

Figure 3.9 shows the measurement of the Rabi frequency in the free space and an example of the microwave spectroscopy. The blue filled circles in Fig. 3.9 (a) show a Rabi oscillation driven by the microwave at high power; the blue line shows a fitting of the data and the corresponding Rabi frequency is 7.50(5) kHz. The red empty circles show the first half period of a Rabi oscillation at lower microwave power; the red line shows the fitting and gives a Rabi frequency of 0.46(3) kHz. In the experiment, we use the lower microwave power and a pulse duration of 1 ms to generate a coherent π-pulse to transfer all the populations to $(1, 6)_0$ state when the microwave is on resonance. Figure 3.9 (b) shows an example microwave spectroscopy and a fitting of the data to determine the centre frequency. The x-axis is the microwave frequency relative to the centre frequency of the transition.

The results of the measurement of the differential light shift between state $(0, 5)_0$ and state $(1, 6)_0$ is shown in Fig. 3.10. The light shift induced by the 1146 nm light is measured as a function of the laser frequency. In this figure the laser frequencies are shown as the detuning relative to the experimentally measured transition frequency. The poles correspond to the transitions to $v' = 0$, 1 and 2, respectively. The dashed lines are at the experimentally measured transition frequencies shown in Table 3.1 by laser spectroscopy; we can see a good agreement between two measurements. In this figure the transitions to higher rotational states in $b^3\Pi_0$ potential cannot be resolved but this is not prohibited by the laser frequency resolution in principle. The destination state of this transition has $M_F = 6$, which means $M_N = 1$, $m_I^{\mathrm{Rb}} = 3/2$, $m_I^{\mathrm{Cs}} = 7/2$. The spin-stretched states ensures that M_N is a good quantum number. For other states M_N can't be known for sure.. The polarisability of this state cannot be described by the theory presented in Section 3.2.2, hence we cannot fit the data to a theoretical function. But the frequency of the magic detuning is nearly the same as predicted by the theory we have.

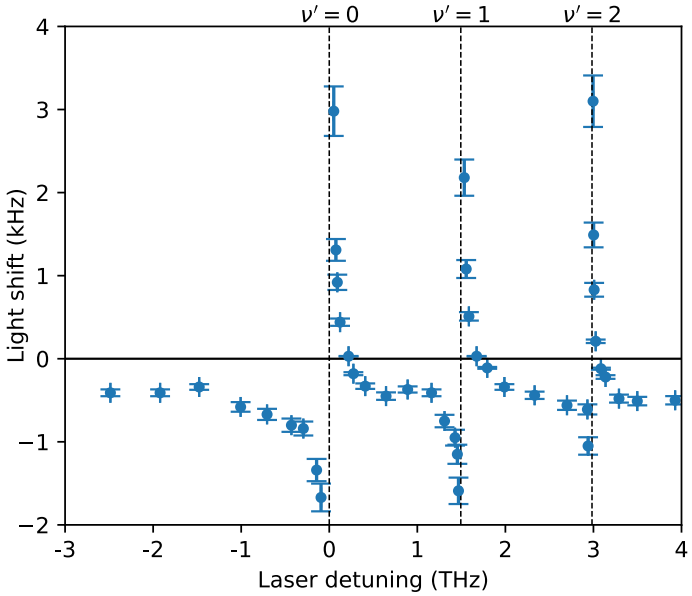

Figure 3.10: Light shift of the transition from $(0, 5)_0$ state to $(1, 6)_0$ state caused by the linearly polarised laser at 1146 nm with $\beta = 90°$. Note that the detuning in the x-axis is given relative to the measured transition frequency to $v' = 0$, i.e., $261571.87 \times 2\pi$ GHz. The light shift of each point in this figure is measured by microwave spectroscopy. An example spectroscopy is shown in Fig. 3.9 (b). The dashed vertical lines are at the previously measured frequencies of the transitions to different vibrational states v' in $b^3\Pi_0$ potential. At magic detuning the light shift is 0. The theory presented in Section 3.2.2 and Fig. 3.4 only holds for π transitions and hence doesn't agree with the results in this figure.

3.3.3 Rotational Coherence of $N = 0 \rightarrow 1$ Near the Magic Wavelength

We investigate the rotational coherence of the molecules associated with the superposition of $(0, 5)_0$ state and $(1, 5)_0$ state around magic frequency. For this purpose we can use Ramsey method which has been an essential method for precision measurement in atomic and molecular physics since it was first introduced [57]. An example of its application can be found in Ref. [58]. In this section we first briefly review the principles of Ramsey method, then the experimental results of the phase-varying Ramsey is presented.

The process of Ramsey sequence can be more easily understood in a Block sphere representation. Consider a simple two-level system with the ground state $|0\rangle$ and the excited state $|1\rangle$. $|0\rangle$ is at the south pole of the Block sphere, $|1\rangle$ is at the north pole. The population is in state $|0\rangle$ initially. In the first step of Ramsey sequence, they are driven by the microwaves with a Rabi frequency of Ω and a detuning from the resonant

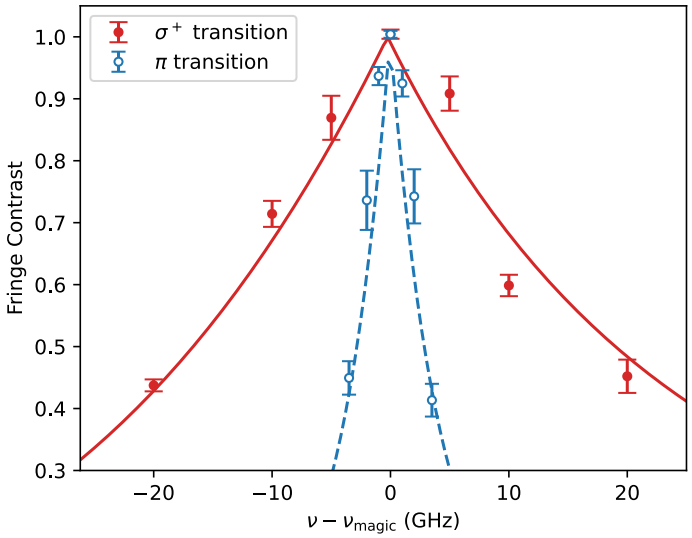

Figure 3.11: Fringe contrast of the phase-varying Ramsey measurement. Each point represents a single experiment. The molecules are initially in $(0, 5)_0$ spin-stretched state. Two microwave pulses are turned on with an evolving time $T = 1$ ms in between. The microwave pulse time τ and its Rabi frequency Ω are such that $\tau\Omega = \pi/2$, i.e. $\pi/2$ pulse. The microwave frequencies are on resonance with the transitions from $N = 0$ to $N = 1$. We fix the phase of the first microwave pulse and vary the phase of the second pulse and measure the fringes of the Rabi oscillation. The decrease of fringe contrast is an indication of dephasing. The blue empty circles show the fringe contrast of π transition, the red filled circles show that of σ^+ transition. The blue dashed line and the red solid line are a fitting of the data, respectively.

transition frequency Δ and a pulse duration τ. The angle by which the state vector is rotated is $\Omega'\tau$ where $\Omega' = \sqrt{\Omega^2 + \Delta^2}$ is the effective Rabi frequency. The axis by which the state vector rotates is determined by Δ and ϕ_0 which is the phase of the microwaves. A pulse with $\Omega'\tau = \pi/2$, i.e. $\pi/2$ pulse drives the state vector to the equator. In the second step the system evolves freely for a time of T. In this period time the state vector precess along the equator at angular frequency Δ. Hence if the detuning Δ is 0, the state vector will stay at the same place. At last, a second microwave pulse with Rabi frequency Ω, detuning Δ, pulse duration τ and phase ϕ rotates the state vector by $\pi/2$ again. The rotation axis depends on the phase of the second pulse ϕ.

There are two types of Ramsey measurement one can do. One type is time-varying Ramsey measurement in which the evolving time T is varied and population in the ground state is measured, the other type is phase-varying Ramsey measurement in which the phase of the second e.m. wave pulse ϕ is varied. In both cases the population in the ground state will oscillate as the time T or the phase ϕ is varied. Due to the gravity, the

molecules drop from the imaging area of STIRAP, which causes a loss of the molecules, hence the decrease of maximum population of the ground state during oscillation. As long as the population in the ground state still goes to 0, the molecular states are still coherent. The decoherence causes a decrease of the maximum population of the ground state during the oscillation and an increase of the minimum population, so the ground state population no longer decreases to zero. One can distinguish the two processes by measuring the fringe contrast of the oscillation. A decoherence causes the decrease in the fringe contrast. With no decoherence the contrast should be 1. The fringe contrast is related to the transition energy shift caused by the AC Stark shift. The contrast decay exponentially as the evolving time T and the polarisability difference between two states and reads

$$C = \exp\left(\frac{-T|\Delta\alpha|I}{h}\right), \tag{3.33}$$

where C is the fringe contrast, T is the evolving time, $\Delta\alpha = \alpha_{N=1} - \alpha_{N=0}$ is the difference in the polarisabilities of the two states, I is the light intensity and h is the Planck constant.

We measure the fringe contrast as a function of laser frequency by a set of phase-varying Ramsey measurements. We drive a transition between $N = 0$ and $N = 1$ rotational states with microwave. The two microwave pulse are both on resonance and are $\pi/2$ pulses. We fix the evolving time T at 1 ms and the phase of the first microwave and vary the phase of the second microwave. In the whole process the molecule is illuminated by the 1146 nm light. Then we change the frequency of the light and repeat the Ramsey sequence to measure the fringe contrast st different laser frequencies around the magic frequency. The measurement is done for both π and σ^+ transitions. π transition refers to the transition from state $|N = 0, M_F = 5\rangle$ to state $|N = 1, M_F = 5\rangle$. σ^+ transition refers to the transition from state $|N = 0, M_F = 5\rangle$ to state $|N = 1, M_F = 6\rangle$. The results are shown in Fig. 3.11 by blue empty circles (π transition) and red filled circles (σ^+ transition). Each point in the figure is an experiment of Ramsey measurement. The x-axis of the figure is relative to the experimentally measured magic frequency value ν_{magic}. At the magic frequency both the π and the σ^+ transitions have the fringe contrast equaling 1, which is a sign of full coherence in the period on 1 ms. The blue dashed line and the red solid line show fittings of the data to Eq. (3.33). The difference of the widths of the fringe contrast feature is due to the sensitivity of the differential light shift to the laser frequency of different combinations of the states. It is also inversely proportional to the Ramsey time which is fixed in this measurement.

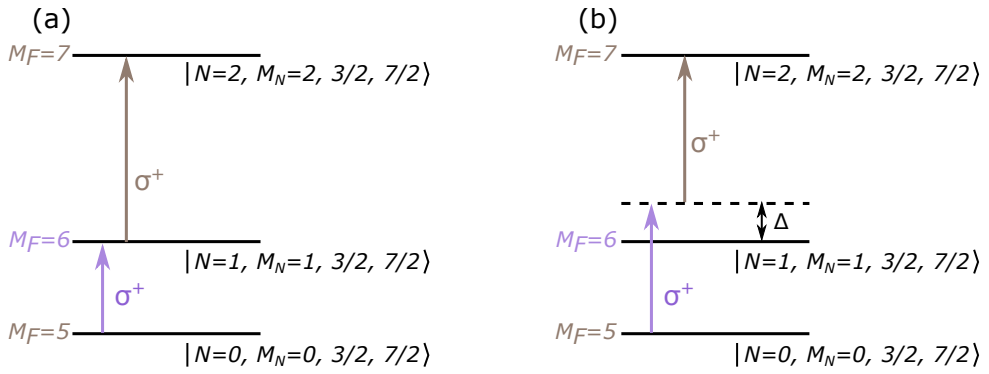

Figure 3.12: The diagram of the two methods to transfer the population from $(0,5)_0$ state to $(2,7)_0$ state. The states are labelled in the uncoupled basis $|N, M_N, m_I^{\mathrm{Rb}}, m_I^{\mathrm{Cs}}\rangle$ but M_F is also given. All the populations begin with the lowest rotational and hyperfine state $(0,5)_0$. (a): Two-step transfer between $N = 0$, 1, 2 using two one-photon transitions. (b): Two-photon transfer from $N = 0$ to 2. The $N = 1$ state is never populated.

3.3.4 Spectroscopy of $N = 1 \rightarrow 2$ Transition

Having measured the spectroscopy of the transition from $N = 0$ to $N = 1$, in this section we address the transition further to the second rotationally excited state $N = 2$ and confirm the magic frequency is also valid for this state. There are two ways to drive the transition from the ground rotational state to the second excited rotational state, the diagram of which are shown in Fig. 3.12. In this experiment we use a two-step transfer method which is shown in Fig. 3.12 (a). The molecules begin with the lowest rotational and hyperfine state and is first transferred to $(1,6)_0$ spin-stretched state by a σ^+ microwave transition. They are further transferred to $(2,7)_0$ spin-stretched state by a σ^+ microwave with a frequency of ∼1960 MHz.

There is another method which we don't use in this experiment to transfer the population shown in Fig. 3.12 (b). The molecules are transferred using a two-photon process in a single step. The two microwave frequencies are near resonance but have a detuning Δ. This is to prevent from populating the intermediate $N = 1$ state. Both microwaves are turned on simultaneously, the power of them should be tuned such that the two microwaves have similar Rabi frequencies.

We use the method shown in Fig. 3.12 (a) to drive the transition from $(0,5)_0$ to $(1,6)_0$ state. We measure the light shift of the transition frequencies from $(1,6)_0$ state to $(2,7)_0$ state as a function of the laser frequency. We first use a resonant π pulse to transfer the molecules from $(0,5)_0$ to $(1,6)_0$ state, the pulse time is 67 μs. Then we pulse on another π pulse for 1 ms to transfer the molecules to $(2,7)_0$ state. The power of this pulse is set such that 1 ms pulse time corresponds to a π pulse. We finally pulse on another π

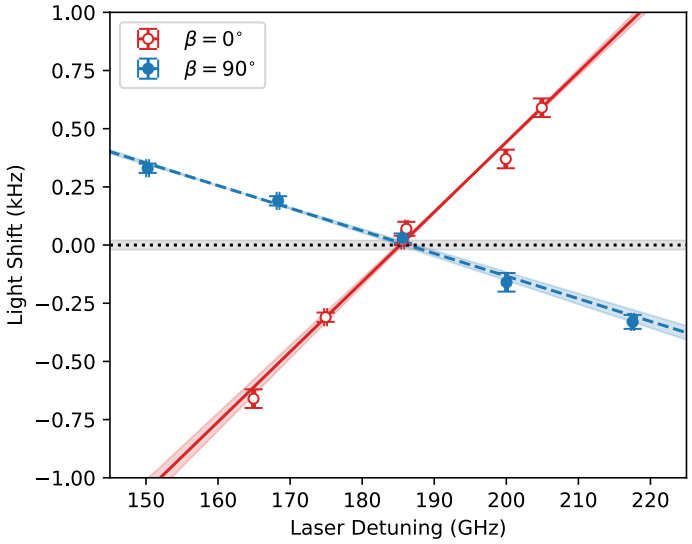

Figure 3.13: The light shift of the $\sigma+$ transition from $N = 1$ to 2 state caused by the 1146 nm laser. The laser frequency is given relative to 261571.87 GHz, the experimentally measured transition frequency. The transition frequency at each laser detuning is measured by microwave spectroscopy and compared to that in the free space. The red empty circles show the light shift data of $\beta = 0°$. The blue filled circles show the data of $\beta = 90°$. The grey shaded area around 0 shows the uncertainty of the free space transition frequency. The red solid and the blue dashed lines are the fittings of the data to straight lines. The shaded areas show the uncertainties of the fittings. The two lines cross x-axis at the same laser detuning within the error.

pulse resonant to the transition from $(0, 5)_0$ to $(1, 6)_0$ for 67 μs to bring any population remaining in $(1, 6)_0$ state back to $(0, 5)_0$ state for imaging. The reason why we use the short pulse time for $N = 0 \rightarrow 1$ transition is that the molecules can only be held in the trap of 1146 nm for $\sim$1 ms and we need to have a lone pulse time for the $N = 1 \rightarrow 2$ transition to get a narrow spectroscopic feature. We repeat this process and change the microwave frequency of the second pulse to measure the spectroscopy of the transition from $(1, 6)_0$ to $(2, 7)_0$ to find the transition frequency. We first measure the transition frequency in free space. Then we shine the 1146 nm light on the molecules and measure the transition frequency shifted by the light. The light shift is the transition frequency with the light minus the transition frequency in free space.

We measure the light shift of the transition frequency caused by the 1146 nm light near the experimentally measured magic frequency for both horizontal and vertical light polarisation. The results are shown in Fig. 3.13. The laser frequencies are given relative to the experimentally measured transition frequency from $v = 0$ state in $X^1\Sigma^+$ potential to v' state in $b^3\Pi_0$ potential which is 261571.87 GHz. The light shifts caused by the

light with two polarisations are both zero at the same laser frequency within the error. This demonstrates a magic laser frequency for the coupling of the $(1,6)_0$ and $(2,7)_0$ spin-stretched states.

3.4 Conclusion

3.4.1 Summary

In this chapter, we present a theoretical calculation of the the "magic frequency" for RbCs molecules to eliminate the anisotropic AC Stark shift followed by experimental demonstration of this method. we introduced the AC Stark effect caused by the trapping light and the corresponding light shift and the decoherence in molecular rotational states. We derived the matrix elements of the interaction energy, treating the isotropic and anisotropic components of the molecular polarisability separately. We gave the analytical equation for the polarisabilities of different rotational states at laser frequencies near a narrow transition between singlet and triplet electronic states. By investigating the behaviours of the polarisability, we identify a $\sim$1.5 GHz wide "near magic" frequency window in which the polarisabilities of the rotational states $N = 0, 1, 2$ become nearly the same. We further demonstrated that the magic frequencies of each states can be tuned by the light polarisation direction and be within 4 kHz of each other at certain polarisation direction.

We measured the transition frequencies from the ground rovibrational state in the ground electronic potential to different vibrational states in the $b^3\Pi_0$ state. We then measured the light shift of the transition between $(0,5)_0$ state and $(1,6)_0$ state by microwave spectroscopy, from which we show the light shift vanishes at the magic frequency. We further measured the phase varying Ramsey fringe contrast to confirm that at the magic frequency, the rotational coherence time for $N = 0, 1$ states lasts at least 1 ms. We subsequently measured the light shift of the transition from $(1,6)_0$ state and $(2,7)_0$ state at two light polarisation directions and showed that in both cases the light shift becomes zero at the same frequency. Thus we confirm a magic frequency for $N = 0, 1, 2$ states exists.

Chapter 4

Conclusions

In this work, we have described a laser system to transfer magnteoassociated molecules in optical tweezers to their ground rovibrational state using STIRAP. This is an important step towards producing ground state RbCs molecule array defined by tweezers, which have many applications in quantum science. We have further demonstrated a magic trapping wavelength that eliminates the differential light shift between the rotational states of the molecule caused by the AC Stark effect of the trapping light. We expect that this wavelength can significantly lengthen the rotational coherence time available in experiments.

4.1 Summary

We have introduced the method to make ultracold RbCs molecules in an optical trap: the pre-cooled constituent atoms are magnetoassociated using a Feshbach resonance before transferred to the rovibrational ground state by STIRAP using an intermediate state. We have introduced the theory of STIRAP based on a three-level system. We then gave the requirements on the linewidth of the STIRAP lasers. To achieve sufficiently low linewidth, an active frequency stabilisation technique need to be used to narrow the laser linewidth as well as ensure the long-term frequency stability. Here a modified Pound-Drever-Hall (PDH) technique is applied; we introduced the theory of the locking technique: the lasers are modulated by EOMs and referenced to a cavity to derive the error signal. This allows the laser frequency to be tunable while locked. We have introduced the cavity theory and characterised the cavity by measuring its finesse and free spectral range. We have experimentally demonstrated the locking technique with a simple, robust laser system and have estimated that the linewidth of the locked laser is $\sim$1.5(3) kHz and that the

lock bandwidth is ∼1.7 MHz. Then we have described the setup to combine the beams and to align the beams to the atoms.

Coherence is essential for many proposed applications of ultracold molecules. In this work, we have focused on the decoherence introduced by the AC Stark effect of the trapping laser. We have given the polarisability of the molecules and the Hamiltonian of the interaction between the linearly polarised light and the molecules. Following the approach by Guan *et al.* [49], we have separated the isotropic and the anisotropic term of the molecular polarisability and given the matrix elements of each of them. We have then given the equation of the molecular polarisability of different rotational states in the ground vibrational states. Based on that equation and a series of experimentally measured parameters, we found a "magic frequency" that eliminates the light shift of the transitions between the lowest rotational states. We experimentally measure the transition frequency from the ground electronic and vibrational state to various vibrational states in the excited $b^3\Pi_0$ electronic state which can be used in the polarisability calculations. We have measured the light shifts of $N = 0 \rightarrow 1$ and $N = 1 \rightarrow 2$ transitions near the magic frequency and confirmed that they vanish st the magic frequency. We further confirmed the coherence time is maximised on the 1 ms time scale by the fringe contrast of the phase varying Ramsey measurement.

4.2 Outlook

There are many future goals we would to achieve in our group with the ground state molecule experiment platform. In this section, we will talk about some of the directions as a continuation of the work done in this thesis.

4.2.1 Making Ground State Molecules in Optical Tweezers

In Chapter. 2 we have introduced the STIRAP theory and the laser system. Previously in our tweezer lab, the ^{87}Rb and ^{133}Cs atoms have been successfully prepared in their relative motional ground state in tweezers [59], which is an important step towards creating RbCs molecules. During the time this thesis was written, we have seen the success in the formation of Feshbach molecules in optical tweezer arrays and the subsequent transfer of the molecules to the ground state using the apparatus described in this thesis.

4.2.2 Application of the Magic Wavelength in a 3D Lattice

In this thesis we measured the transition frequency to different vibrational states in $b^3\Pi_0$ potential, but we don't know the transition widths with confidence. The next step is to measure the light shift near the poles corresponding to the transitions to higher vibrational states and extract the transition widths. We also notice that the light shift can be zero at frequencies near these poles, which makes these frequencies "magic" frequency, too. As a full characterisation, the magic frequencies near higher order poles should also be measured.

Currently the intensity of the 1146 nm laser we use in our experiment is not high enough to trap molecules. This limits the time by which we can hold the molecules to $\sim$1 ms. The next step of implementing the magic frequency is to use another laser source working at 1146 nm with higher output power to make an optical trap and confine the molecules. We can then measure the lifetime and the rotational coherence time in the magic trap.

The further goal of the experiment described in Chapter 3 is to construct a 3D optical lattice for RbCs molecules. To achieve this, three beams in x, y, x directions are needed. We can judiciously choose the polarisation directions and the frequencies of the beams to make a "magic" 3D lattice making using of the polarisation-dependence of the magic frequency.

4.2.3 Optical Tweezers for Robust Entangling Molecular Gate

Polar molecules have been proposed as a promising platform for quantum information processing [4, 60] as the strong dipole-dipole interactions between molecules and the long coherence time makes them a good candidate of qubits. The quantum information can be encoded in the hyperfine states of the molecules. The molecules trapped in an controlled array of tweezers is especially a powerful tool for this application [61–64]. A long coherence time is essential for all the proposed applications. A potential way to extent the coherence time of the molecules in tweezers is to use the magic frequency investigated in this thesis, i.e., to use the laser at 1146 nm to make "magic tweezers" and to trap the molecules.

Bibliography

[1]L. Santos, G. V. Shlyapnikov, P. Zoller, and M. Lewenstein, "Bose-einstein condensation in trapped dipolar gases", Phys. Rev. Lett. **85**, 1791–1794 (2000).

[2]M. A. Baranov, M. Dalmonte, G. Pupillo, and P. Zoller, "Condensed matter theory of dipolar quantum gases", Chemical Reviews **112**, 5012–5061 (2012).

[3]D. DeMille, "Quantum computation with trapped polar molecules", Phys. Rev. Lett. **88**, 067901 (2002).

[4]S. F. Yelin, K. Kirby, and R. Côté, "Schemes for robust quantum computation with polar molecules", Physical Review A **74**, 050301 (2006).

[5]M. Du, D. Zhang, and T. E. Wall, "Preparation of cold molecules for high-precision measurements", Journal of Physics B **49**, 243001 (2016).

[6]R. V. Krems, "Cold controlled chemistry", Physical Chemistry Chemical Physics **10**, 4079–4092 (2008).

[7]K. K. Ni, S. Ospelkaus, D. Wang, G. Quéméner, B. Neyenhuis, M. H. D. Miranda, J. L. Bohn, J. Ye, and D. S. Jin, "Dipolar collisions of polar molecules in the quantum regime", Nature 2010 464:7293 **464**, 1324–1328 (2010).

[8]S. Ospelkaus, K. K. Ni, D. Wang, M. H. D. Miranda, B. Neyenhuis, G. Quéméner, P. S. Julienne, J. L. Bohn, D. S. Jin, and J. Ye, "Quantum-state controlled chemical reactions of ultracold potassium-rubidium molecules", Science **327**, 853–857 (2010).

[9]M. H. D. Miranda, A. Chotia, B. Neyenhuis, D. Wang, G. Quéméner, S. Ospelkaus, J. L. Bohn, J. Ye, and D. S. Jin, "Controlling the quantum stereodynamics of ultracold bimolecular reactions", Nature Physics 2011 7:6 **7**, 502–507 (2011).

[10]A. Micheli, G. K. Brennen, and P. Zoller, "A toolbox for lattice-spin models with polar molecules", Nature Physics 2006 2:5 **2**, 341–347 (2006).

[11]A. V. Gorshkov, S. R. Manmana, G. Chen, J. Ye, E. Demler, M. D. Lukin, and A. M. Rey, "Tunable superfluidity and quantum magnetism with ultracold polar molecules", Phys. Rev. Lett. **107**, 115301 (2011).

[12]N. Y. Yao, M. P. Zaletel, D. M. Stamper-Kurn, and A. Vishwanath, "A quantum dipolar spin liquid", Nature Physics 2018 14:4 **14**, 405–410 (2018).

[13]P. K. Molony, "Creation of ultracold polar ground-state RbCs molecules", Ph.D. thesis (Durham University, 2016).

[14]P. D. Gregory, "Coherent control of ultracold polar molecules", Ph.D. thesis (Durham University, 2018).

[15]J. A. Blackmore, "Coherence and collisions in ultracold rbcs molecules" (Durham University, 2020).

[16]P. K. Molony, P. D. Gregory, Z. Ji, B. Lu, M. P. Köppinger, C. R. Le Sueur, C. L. Blackley, J. M. Hutson, and S. L. Cornish, "Creation of ultracold $^{87}Rb^{133}Cs$ molecules in the rovibrational ground state", Phys. Rev. Lett. **113**, 255301 (2014).

[17]J. Klein, F. Beil, and T. Halfmann, "Experimental investigations of stimulated raman adiabatic passage in a doped solid", Physical Review A **78**, 033416 (2008).

[18]G. S. Vasilev, A. Kuhn, and N. V. Vitanov, "Optimum pulse shapes for stimulated raman adiabatic passage", Physical Review A **80**, 013417 (2009).

[19]K. Bergmann, N. V. Vitanov, and B. W. Shore, "Perspective: stimulated raman adiabatic passage: the status after 25 years", The Journal of Chemical Physics **142**, 170901 (2015).

[20]L. Reichsöllner, A. Schindewolf, T. Takekoshi, R. Grimm, and H. C. Nägerl, "Quantum engineering of a low-entropy gas of heteronuclear bosonic molecules in an optical lattice", Phys. Rev. Lett. **118**, 073201 (2017).

[21]S. A. Moses, J. P. Covey, M. T. Miecnikowski, B. Yan, B. Gadway, J. Ye, and D. S. Jin, "Creation of a low-entropy quantum gas of polar molecules in an optical lattice", Science **350**, 659–662 (2015).

[22]P. D. Gregory, J. A. Blackmore, S. L. Bromley, J. M. Hutson, and S. L. Cornish, "Robust storage qubits in ultracold polar molecules", Nature Physics **17**, 1149–1153 (2021).

[23]N. V. Vitanov, A. A. Rangelov, B. W. Shore, and K. Bergmann, "Stimulated raman adiabatic passage in physics, chemistry, and beyond", Reviews of Modern Physics **89**, 015006 (2017).

[24]P. D. Gregory, P. K. Molony, M. P. Köppinger, A. Kumar, Z. Ji, B. Lu, A. L. Marchant, and S. L. Cornish, "A simple, versatile laser system for the creation of ultracold ground state molecules", New Journal of Physics **17**, 055006 (2015).

[25]L. P. Yatsenko, V. I. Romanenko, B. W. Shore, and K. Bergmann, "Stimulated raman adiabatic passage with partially coherent laser fields", Physical Review A **65**, 043409 (2002).

[26]K. Aikawa, D. Akamatsu, J. Kobayashi, M. Ueda, T. Kishimoto, and S. Lnouye, "Toward the production of quantum degenerate bosonic polar molecules, $^{41}K^{87}Rb$", New Journal of Physics **11**, 055035 (2009).

[27]C. S. Adams and I. G. Hughes, *Optics f2f: from fourier to fresnel* (Oxford University Press, Dec. 2018).

[28]W. T. Silfvast, *Laser fundamentals* (Cambridge University Press, Jan. 2004).

[29]G. Brooker, *Modern classical optics*, Vol. 8 (Oxford University Press, July 2003).

[30]O. Svelto, *Principles of lasers*, edited by D. C. Hanna, 5th ed. (Springer, 2010).

[31]G. Machavariani, N. Davidson, A. Ishaaya, and A. Friesem, "Improving the stability of longitudinal and transverse laser modes", Optics communications **239**, 147–151 (2004).

[32]C. Bond, D. Brown, A. Freise, and K. Strain, "Interferometer techniques for gravitational-wave detection", `10.12942/lrr-2010-1` (2009).

[33]M. P. Koppinger, "Creation of ultracold RbCs molecules", Ph.D. thesis (Durham University, 2014).

[34]R. W. Fox, "Fabry-perot temperature dependence and surface-mounted optical cavities", Optics Express, Vol. 17, Issue 17, pp. 15023-15031 **17**, 15023–15031 (2008).

[35]B. Willke, M. E. Husman, E. K. Gustafson, R. L. Byer, and M. J. Lawrence, "Dynamic response of a fabry–perot interferometer", JOSA B, Vol. 16, Issue 4, pp. 523-532 **16**, 523–532 (1999).

[36]E. D. Black, "An introduction to pound–drever–hall laser frequency stabilization", American Journal of Physics **69**, 79–87 (2001).

[37]G. C. Bjorklund, "Frequency-modulation spectroscopy: a new method for measuring weak absorptions and dispersions", Optics Letters, Vol. 5, Issue 1, pp. 15-17 **5**, 15–17 (1980).

[38]D. J. McCarron, S. A. King, and S. L. Cornish, "Modulation transfer spectroscopy in atomic rubidium", Measurement Science and Technology **19**, 105601 (2008).

[39]J. I. Thorpe, K. Numata, J. Livas, R. Drever, J. Hall, F. Kowalski, J. Hough, G. Ford, A. Munley, H. Ward, H. Zhen, H. Ye, X. Liu, D. Zhu, H. Li, Y. Lu, and Q. Wang, "Laser frequency stabilization and control through offset sideband locking to optical cavities", Optics Express, Vol. 16, Issue 20, pp. 15980-15990 **16**, 15980–15990 (2008).

[40]B. J. J. Slagmolen, D. E. McClelland, K. G. Baigent, and M. B. Gray, "Phase-sensitive reflection technique for characterization of a fabry–perot interferometer", Applied Optics, Vol. 39, Issue 21, pp. 3638-3643 **39**, 3638–3643 (2000).

[41]P. K. Molony, P. D. Gregory, A. Kumar, C. R. L. Sueur, J. M. Hutson, and S. L. Cornish, "Production of ultracold $^{87}Rb^{133}Cs$ in the absolute ground state: complete characterisation of the stimulated raman adiabatic passage transfer", ChemPhysChem **17**, 3811–3817 (2016).

[42]H. S. Moon, W. K. Lee, L. Lee, and J. B. Kim, "Double resonance optical pumping spectrum and its application for frequency stabilization of a laser diode", Applied Physics Letters **85**, 3965–3967 (2004).

[43]A. Nakayama, "Novel method for high resolution measurement of laser output spectrum", English, Electronics Letters **16**, 630–631(1) (1980).

[44]P. Horak and W. H. Loh, "On the delayed self-heterodyne interferometric technique for determining the linewidth of fiber lasers", Opt. Express **14**, 3923–3928 (2006).

[45]H. Tsuchida, "Simple technique for improving the resolution of the delayed self-heterodyne method", Opt. Lett. **15**, 640–642 (1990).

[46]J. A. Blackmore, R. Sawant, P. D. Gregory, S. L. Bromley, J. Aldegunde, J. M. Hutson, and S. L. Cornish, "Controlling the ac stark effect of rbcs with dc electric and magnetic fields", Physical Review A **102**, 053316 (2020).

[47]P. D. Gregory, J. A. Blackmore, J. Aldegunde, J. M. Hutson, and S. L. Cornish, "AC Stark effect in ultracold polar $^{87}Rb^{133}Cs$ molecules", Physical Review A **96**, 021402 (2017).

[48]B. Yan, S. A. Moses, B. Gadway, J. P. Covey, K. R. Hazzard, A. M. Rey, D. S. Jin, and J. Ye, "Observation of dipolar spin-exchange interactions with lattice-confined polar molecules", Nature 2013 501:7468 **501**, 521–525 (2013).

[49]Q. Guan, S. L. Cornish, and S. Kotochigova, "Magic conditions for multiple rotational states of bialkali molecules in optical lattices", Physical Review A **103**, `10.1103/PhysRevA.103.043311` (2021).

[50]S. Kotochigova and E. Tiesinga, "Controlling polar molecules in optical lattices", Physical Review A **73**, 041405 (2006).

[51]R. Vexiau, D. Borsalino, M. Lepers, A. Orbán, M. Aymar, O. Dulieu, and N. Bouloufa-Maafa, "Dynamic dipole polarizabilities of heteronuclear alkali dimers: optical response, trapping and control of ultracold molecules", International Reviews in Physical Chemistry **36**, 709–750 (2017).

[52]M. Li, A. Petrov, C. Makrides, E. Tiesinga, and S. Kotochigova, "Pendular trapping conditions for ultracold polar molecules enforced by external electric fields", Physical Review A **95**, 063422 (2017).

[53]C. E. Fellows, R. F. Gutterres, A. P. Campos, J. Vergès, and C. Amiot, "The RbCs $X^1\Sigma^+$ ground electronic state: new spectroscopic study", Journal of Molecular Spectroscopy **197**, 19–27 (1999).

[54]P. D. Gregory, J. Aldegunde, J. M. Hutson, and S. L. Cornish, "Controlling the rotational and hyperfine state of ultracold ^{87}Rb^{133}Cs molecules", Physical Review A **94**, 041403 (2016).

[55]M. P. Köppinger, D. J. McCarron, D. L. Jenkin, P. K. Molony, H. W. Cho, S. L. Cornish, C. R. L. Sueur, C. L. Blackley, and J. M. Hutson, "Production of optically trapped ^{87}RbCs feshbach molecules", Physical Review A **89**, 033604 (2014).

[56]S. Subhankar, A. Restelli, Y. Wang, S. L. Rolston, and J. V. Porto, "Microcontroller based scanning transfer cavity lock for long-term laser frequency stabilization", Review of Scientific Instruments **90**, 043115 (2019).

[57]N. F. Ramsey, "A molecular beam resonance method with separated oscillating fields", Physical Review **78**, 695 (1950).

[58]S. Truppe, R. J. Hendricks, S. K. Tokunaga, H. J. Lewandowski, M. G. Kozlov, C. Henkel, E. A. Hinds, and M. R. Tarbutt, "A search for varying fundamental constants using hertz-level frequency measurements of cold ch molecules", Nature Communications 2013 4:1 **4**, 1–7 (2013).

[59]S. Spence, R. V. Brooks, D. K. Ruttley, A. Guttridge, and S. L. Cornish, "Preparation of ^{87}Rb and ^{133}Cs in the motional ground state of a single optical tweezer", New Journal of Physics **24**, 10.1088/1367-2630/ac95b9 (2022).

[60]J. Zhu, S. Kais, Q. Wei, D. Herschbach, and B. Friedrich, "Implementation of quantum logic gates using polar molecules in pendular states", The Journal of Chemical Physics **138**, 024104 (2013).

[61]M. Hughes, M. D. Frye, R. Sawant, G. Bhole, J. A. Jones, S. L. Cornish, M. R. Tarbutt, J. M. Hutson, D. Jaksch, and J. Mur-Petit, "Robust entangling gate for polar molecules using magnetic and microwave fields", Physical Review A **101**, 062308 (2020).

[62]K. K. Ni, T. Rosenband, and D. D. Grimes, "Dipolar exchange quantum logic gate with polar molecules", Chemical Science **9**, 6830–6838 (2018).

[63]C. M. Holland, Y. Lu, and L. W. Cheuk, "On-demand entanglement of molecules in a reconfigurable optical tweezer array", 10.48550/arxiv.2210.06309 (2022).

[64]Y. Bao, S. S. Yu, L. Anderegg, E. Chae, W. Ketterle, K.-K. Ni, and J. M. Doyle, "Dipolar spin-exchange and entanglement between molecules in an optical tweezer array", 10.48550/arxiv.2211.09780 (2022).